Naval Surface Warfare Center
Carderock Division
West Bethesda, MD 20817-5700

NSWCCD-61-TR-2023/13 **September 2023**

Platform Integrity Department

Technical Report

Temperature-Dependent Material Property Databases for Marine Steels – Part 6: HY-100

By

Justin E. Norkett

Jennifer K. Semple

Daniel H. Bechetti

Wei Zhang (The Ohio State University)

Charles R. Fisher

Naval Surface Warfare Center
Carderock Division
West Bethesda, MD 20817-5700

NSWCCD-61-TR-2023/13 **September 2023**

Platform Integrity Department
Technical Report

Temperature-Dependent Material Property Databases for Marine Steels – Part 6: HY-100

by
Justin E. Norkett
Jennifer K. Semple
Daniel H. Bechetti
Wei Zhang (The Ohio State University)
Charles R. Fisher

REPORT DOCUMENTATION PAGE

Form Approved
OMB No. 0704-0188

1. REPORT DATE *(DD-MM-YYYY)*	2. REPORT TYPE	3. DATES COVERED *(From - To)*
22-09-2023	Technical Report	JAN 2018 – JUN 2019

4. TITLE AND SUBTITLE

Temperature-Dependent Material Property Databases for Marine Steels – Part 6: HY-100

5a. CONTRACT NUMBER
N/A

5b. GRANT NUMBER
N/A

5c. PROGRAM ELEMENT NUMBER
N/A

6. AUTHOR(S)
Justin E. Norkett
Jennifer K. Semple
Daniel H. Bechetti
Wei Zhang
Charles R. Fisher

5d. PROJECT NUMBER
N/A

5e. TASK NUMBER

5f. WORK UNIT NUMBER

7. PERFORMING ORGANIZATION NAME(S) AND ADDRESS(ES) AND ADDRESS(ES)

Naval Surface Warfare Center,
Carderock Division, Code 611
9500 MacArthur Boulevard
West Bethesda, MD 20817-5700

Ohio State University, Department of
Materials Science & Engineering
Welding Engineering Program
1248 Arthur Adams Dr
Columbus, OH 43221

8. PERFORMING ORGANIZATION REPORT NUMBER

NSWCCD-61-TR-2023/13

9. SPONSORING / MONITORING AGENCY NAME(S) AND ADDRESS(ES)

William Mullins
Program Manager, 332
Office of Naval Research
Arlington, VA 22217

Lightweight Innovations for Tomorrow (LIFT)
Detroit, MI 48216

10. SPONSOR/MONITOR'S ACRONYM(S)
ONR

11. SPONSOR/MONITOR'S REPORT NUMBER(S)
N/A

12. DISTRIBUTION / AVAILABILITY STATEMENT
DISTRIBUTION A. Approved for public release: distribution unlimited.

13. SUPPLEMENTARY NOTES

14. ABSTRACT:
The Lightweight Innovations for Tomorrow (LIFT) project entitled, Robust Distortion Control Methods and Implementation for Construction of Lightweight Metallic Structures – ICME Extension to Advanced Alloys, sought to address distortion issues with thin-plate steel fabrication of U.S. Navy ships. Integrated Computational Materials Engineering (ICME)-based tools and techniques were identified as the best path forward for distortion mitigation through computational simulation of the welding process. ICME tools require temperature-dependent material properties to achieve accurate computational results for distortion and residual stress. Properties of note include specific heat, thermal conductivity, coefficient of thermal expansion (CTE), elastic modulus, yield strength, and flow stress of alloys from room temperature to near melting. In addition, the temperatures associated with on-heating and on-cooling phase transformations and their variation with heating rate, cooling rate, and peak temperature are also important for the prediction of stress and distortion evolution.

The integrated project team made generating pedigreed, temperature-dependent material property databases of Navy-relevant steels a key task within the LIFT project. The testing plan included some of the most common marine steels used in the construction of U.S. Naval vessels; namely, DH36, HSLA-65, HSLA-80, HSLA-100, HY-80, and HY-100. Material testing for each of the six steel grades was performed jointly by the Welding Engineering Program within the Department of Materials Science and Engineering at the Ohio State University (OSU) and the Welding, Processing, and Nondestructive Evaluation Branch at the Naval Surface Warfare Center, Carderock Division(NSWCCD). The temperature-dependent material property data were then sent to ESI for adaptation for use in their welding-based, finite-element analysis (FEA) software colloquially known as SYSWELD.

This report is part of a seven-part series detailing the pedigreed steel data. The first six reports will report and discuss the material properties for each of the individual steel grades, whereas the final report will compare and contrast the measured steel properties across all six steels, while also comparing them to the available literature data. This report will focus specifically on the data associated with HY-100 steel.

15. SUBJECT TERMS
ICME, CWM, SYSWELD, Computational Simulation, Steel, Welding, Material Database, HY-100

16. SECURITY CLASSIFICATION OF:			17. LIMITATION OF ABSTRACT	18. NUMBER OF PAGES	19a. RESPONSIBLE PERSON
a. REPORT	b. ABSTRACT	c. THIS PAGE			19b. TELEPHONE NUMBER
UNCLASSIFIED	UNCLASSIFIED	UNCLASSIFIED		81	Charles Fisher (301) 221-2259

CONTENTS

Page

FIGURES

Page

TABLES

Page

ADMINISTRATIVE INFORMATION

The work described in this report was performed by the Welding, Processing, and Nondestructive Evaluation Branch (Code 611) of the Platform Integrity Department at the Naval Surface Warfare Center, Carderock Division (NSWCCD) and by the Department of Materials Science and Engineering at the Ohio State University. The work was funded in FY18-19 by the Office of Naval Research (ONR), in support of the Lightweight Innovations for Tomorrow (LIFT) Institute's program entitled *Robust Distortion Control Methods and Implementation for Construction of Lightweight Metallic Structures – ICME Extension to Advanced Alloys*.

ACKNOWLEDGEMENTS

The authors would like to thank the other members of the LIFT Joining-R4-3 integrated project team, including other engineers at the Naval Surface Warfare Center, Carderock Division (Matthew Sinfield, Maria Posada, and Johnnie DeLoach), Huntington Ingalls Industries – Ingalls Shipbuilding (T.D. Huang, Randy Johnson, Yu-Ping Yang, Steve Scholler, Charlotte Merritt, Shannon Dolese, Anthony Copeland, Andrew Nicholson, Lance Carnahan, Stacey Merritt, Win Delancey, Dianna Genton, and John Walks), the University of Michigan (Pingsha Dong, Jack Hu, Theodor Freiheit), the Ohio State University (Colleen Hilla and Chris Cathis), ESI (Yogendra [San] Gooroochan and Mark Doroudian), and LIFT (Melvin Hawke, Alan Taub, and Hadrian Rori), for their technical assistance in the completion of this work.

This page intentionally left blank

EXECUTIVE SUMMARY

The Lightweight Innovations for Tomorrow (LIFT) project entitled, Robust Distortion Control Methods and Implementation for Construction of Lightweight Metallic Structures – ICME Extension to Advanced Alloys, sought to address distortion issues with thin-plate steel fabrication of U.S. Navy ships. Integrated Computational Materials Engineering (ICME)-based tools and techniques were identified as the best path forward for distortion mitigation through computational simulation of the welding process. ICME tools require temperature-dependent material properties to achieve accurate computational results for distortion and residual stress. Properties of note include specific heat, thermal conductivity, coefficient of thermal expansion (CTE), elastic modulus, yield strength, and flow stress of alloys from room temperature to near melting. In addition, the temperatures associated with on-heating and on-cooling phase transformations and their variation with heating rate, cooling rate, and peak temperature are also important for the prediction of stress and distortion evolution.

The integrated project team (IPT) made generating pedigreed, temperature-dependent material property databases of Navy-relevant steels a key task within the LIFT project. The testing plan included some of the most common marine steels used in the construction of U.S. Naval vessels; namely, DH36, HSLA-65, HSLA-80, HSLA-100, HY-80, and HY-100. Material testing for each of the six steel grades was performed jointly by the Welding Engineering Program within the Department of Materials Science and Engineering at the Ohio State University (OSU) and the Welding, Processing, and Nondestructive Evaluation Branch at the Naval Surface Warfare Center, Carderock Division (NSWCCD). The temperature-dependent material property data were then sent to ESI for adaptation for use in their welding-based, finite-element analysis (FEA) software colloquially known as SYSWELD.

This report is part of a seven-part series detailing the pedigreed steel data. The first six reports will report and discuss the material properties for each of the individual steel grades, whereas the final report will compare and contrast the measured steel properties across all six steels, while also comparing them to the available literature data. This report will focus specifically on the data associated with HY-100 steel.

BACKGROUND

The Lightweight Innovations for Tomorrow (LIFT) project entitled, *Robust Distortion Control Methods and Implementation for Construction of Lightweight Metallic Structures – ICME Extension to Advanced Alloys*, is a collaborative research project to address the complex fabrication problems that arise from the use of thin, high-strength steel panels for ship construction. The importance of lightweighting in the commercial and military shipbuilding sectors has gained attention in recent decades as a way to increase the performance capabilities of products while also reducing total ownership costs. Over the past decade, the production ratio of thin plate (10 mm [3/8-in.] or less) to thicker plate structures for steel construction at Huntington Ingalls Industries – Ingalls Shipbuilding has risen to over 80% in the Coast Guard's National Security Cutter (NSC) program. Modern naval vessel designs also make greater use of complex panels with inserts and cutouts, further increasing the fabrication complexity to achieve weight savings while meeting structural requirements.

European shipbuilding research suggests that 30% of hull fabrication costs can be attributed to re-work and fit-up issues due to distortion [1]. Integrated Computational Materials Engineering (ICME)-based prediction tools can be used to quantify distortions associated with the fabrication process of complex stiffened panels or other lightweight structures. These tools, once validated on selected product

forms, could be used to establish recommended fitting, fixturing, welding, and assembly sequencing for optimized distortion control in thin-plate steel construction.

These ICME tools require detailed, reliable databases of temperature-dependent material properties in order to increase the accuracy of calculated distortion and residual stresses in welded metallic structures. Of highest importance to the fidelity of such models are the thermo-physical and thermo-mechanical properties of the material(s) being joined. The properties of note include specific heat, thermal conductivity, coefficient of thermal expansion (CTE), elastic modulus, yield strength, and flow stress of the alloy, from room temperature to near melting. The temperatures associated with on-heating and on-cooling phase transformations and their variation with heating rate, cooling rate, and peak temperature are also important for the prediction of stress and distortion evolution.

While some of these data exists for the most common Navy steels, these are generally not suitable for use in high-fidelity welding-focused computational models for several reasons. First, the methods of data generation are inconsistent because the testing was completed over many decades by separate researchers and programs. Also, significant gaps exist in the data, especially at temperatures above approximately 400 °C (~750 °F). Additionally, some available data are restricted against public distribution. Finally, the data are, in general, subject to reliability issues because of changes in material fabrication and testing practices that have occurred in the decades since the data were generated. To combat this lack of comprehensive and consistent data, the integrated project team (IPT) made generating pedigreed, temperature-dependent material property databases of Navy-relevant steels a key task within the LIFT project. A major portion of the tasking involved analysis of heat-affected zone (HAZ) microstructures, as this region of rapidly changing microstructure results in significant changes in resultant mechanical properties. These varied HAZ region microstructures of Navy-relevant alloys do not have well-established mechanical property data, especially as a function of temperature and heating or cooling rate.

The testing plan included some of the most common marine steels used in the construction of U.S. Naval vessels; namely DH36, HSLA-65, HSLA-80, HSLA-100, HY-80, and HY-100. HSLA is short for “high-strength low-alloy,” whereas HY stands for “high yield.” The number designation behind HSLA and HY is the minimum yield strength of the plate material in units of ksi. Current (as of this writing) specifications for these alloys can be found in references [2] [3] [4]. Material testing for each of the six steel grades was performed jointly by the Welding Engineering Program within the Department of Materials Science and Engineering at the Ohio State University (OSU) and the Welding, Processing, and Nondestructive Evaluation Branch at the Naval Surface Warfare Center, Carderock Division (NSWCCD). The temperature-dependent material property data were then sent to ESI for adaptation for use in their welding-based, finite-element analysis (FEA) software colloquially known as *SYSWELD*.

This report is part of a seven-part series based on the pedigreed steel data. The first six reports will focus on establishing the material properties for each of the individual steel grades, whereas the final report will compare and contrast the measured steel properties across all six steels, while also comparing them to the available literature data. Follow-on reports detailing use of these temperature-dependent material databases within the LIFT-funded program are also expected. While this report focuses on HY-100 data, the citation for the previous report on DH36 is [5], HSLA-65 is [6], HSLA-80 is [7], HSLA-100 is [8], and HY-80 is [9].

APPROACH

Material Testing Program

The material property assessment program was developed through inputs from welding engineers at NSWCCD, researchers at OSU, and modeling experts at ESI. The program focused on generating the

types of data required to develop Navy-relevant material databases for use by ESI's commercial software, *SYSWELD*. The raw data could also be adapted for use by other FEA tools, such as MSC's *Simufact Welding* or the welding module for *Abaqus*. Specific data included thermo-physical and mechanical properties of the alloys of interest, from room temperature up to near-melting. Density, heat capacity, thermal conductivity, and coefficient of thermal expansion (CTE) were identified as the most important thermo-physical properties. Mechanical properties of interest included the elastic modulus, yield strength, and flow stress.

Material from a single HY-100 steel plate procured to NAVSEA Technical Publication T9074-BD-GIB-010/0300 (Tech Pub 300) [4] was analyzed for this project. The nominally 4.76 mm (3/16-in.) thick plate was acquired by Huntington Ingalls Industries – Ingalls Shipbuilding (HII – Ingalls). The room temperature yield strength and elongation requirements for the alloy are 690-827 MPa (100-120 ksi) and 17% in 50 mm (2-in.), respectively [4]. There are no ultimate tensile strength requirements for HY-100 plate procured to Tech Pub 300 [4]. The plate conformance certification sheet for the material investigated in this study is given in **Appendix A**. A portion of this plate was cut into 610 mm by 305 mm (24-in. by 12-in.) pieces and shipped to both NSWCCD and OSU for determination of temperature-dependent material properties.

Chemical Composition

The chemical composition of the base material was measured at OSU using optical emission spectroscopy on a SPECTROMAXx arc spark system. Additional chemical composition testing was performed at NSWCCD using glow discharge atomic emission spectroscopy (GD-AES) with a LECO GDS900 glow discharge spectrometer. All AES/GDS composition testing was performed in accordance with ASTM E415 [10]. Carbon and sulfur content was measured at NSWCCD with a LECO CS844 combustion analyzer according to ASTM E1019 [11].

Heat Affected Zone Phase Transformation Analysis

Phase transformations of HY-100 as a function of austenitization temperature and cooling rate were assessed via dilatometry. Continuous cooling transformation (CCT) diagrams were developed for four regions of the heat affected zone (HAZ) that are subject to microstructural transformation during welding: the intercritical region (ICHAZ); the low-temperature, fine-grained region (FGHAZ1); the high-temperature, fine-grained region (FGHAZ2); and the coarse-grained region (CGHAZ).

Heating and cooling rates for these regions in HY-100 were assumed to be the similar those for DH36 weldments [5]. As part of the DH36 effort [5], the heating and cooling rates were defined by combining typical heat inputs used in the fabrication of DH36 weldments, from 0.4 to 2.6 kJ/mm (10 to 65 kJ/in) as suggested by Ingalls engineers, with numerical simulation of the heat flow using the *SmartWeld* program from Sandia National Laboratories [12]. From these calculations, it was determined that peak temperatures (T_{peak}) between 785 and 1350 °C (1445 and 2462 °F), in combination with cooling rates between 1 and 200 °C/s (1.8 and 360 °F/s), would provide information covering a sufficiently broad range of phase transformation behavior relevant to both slowly-cooled welds (*e.g.*, high heat input welds on thin plate) and rapidly-cooled welds (*e.g.*, low heat input welds on thick plate). These CCT diagrams informed the temperature-dependent mechanical property testing program as well, specifically for heating and cooling rates, peak temperatures, and various testing temperatures.

In addition to the on-cooling CCT diagram development, this portion of the testing program also involved a detailed assessment of the on-heating austenite transformation as a function of heating rate. Just as on-cooling transformation temperatures vary with cooling rate, so does on-heating austenitization temperature (A_{c1} and A_{c3}). Heating rates between 10 and 2000 °C/s (18 and 3632 °F/s) were used to study these variations. **Table 1** shows the full test matrix utilized for HAZ CCT diagram development.

Table 1. Test Matrix for HAZ CCT Diagram Development

Test Type	Region	Peak Temperature, °C (°F)	Heating Rate, °C/s (°F/s)	Soak Time, s	Cooling Rate, °C/s (°F/s)
A_{c1}/A_{c3} Determination	N/A	1200 (2192)	10 (18) 100 (180) 200 (360) 500 (900) 1000 (1800) 2000 (3600)	N/A	N/A
CCT Diagram Development	ICHAZ	785 (1445)	200 (360)	2	1 (1.8) 5 (9) 10 (18) 25 (45) 100 (180) 200 (360)
	FGHAZ1	1000 (1832)			
	FGHAZ2	1150 (2102)			
	CGHAZ	1350 (2462)			

Execution of this test matrix was performed at NSWCCD by employing a Gleeble 3500 thermo-mechanical simulation apparatus to apply the prescribed heating and cooling rates. The Gleeble operates on the principles of resistive heating, conductive cooling through water-cooled fixturing, and rapid (50 kHz) control system feedback to apply precise thermal cycles even at rapid heating and cooling rates that cannot be easily achieved by other apparatus. The Gleeble 3500 system, in combination with the apparatus's standard 'Pocket Jaw' setup, used full contact copper grips and 70 mm (2.76-in.) long specimens with 3 mm (0.118-in.) diameters. A linear variable differential transformer (LVDT)-type contact extensometer was used to measure diametric dilation of the specimens during heating and cooling. All dilatometry specimens were extracted perpendicular to the rolling direction of the plate, and all dilatometry tests were performed in an argon atmosphere. The typical experimental setup for the dilatometry testing is shown in **Figure 1.**

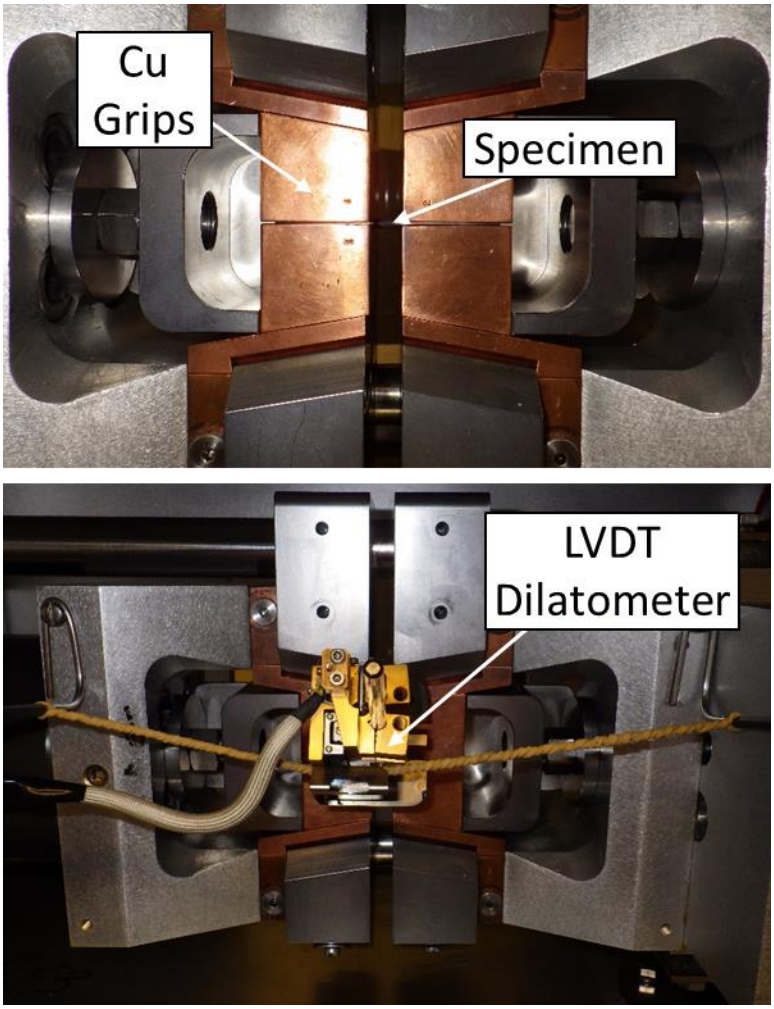

Figure 1. Photographs of the Gleeble-based dilatometry experimental set-up.

Thermo-Physical Property Analysis

Specimens were sent to the Thermophysical Properties Research Laboratory, Inc. (TPRL) in West Lafayette, IN for analysis of thermal diffusivity (α) and specific heat (C_p). Thermal diffusivity was measured using the laser flash method according to ASTM E1461 [13]. Specific heat was measured using differential scanning calorimetry (DSC) methods according to ASTM E1269 [14]. Coefficient of thermal expansion (CTE) was measured from the on-heating Gleeble dilatometry data in two regimes: 200 to 750 °C (392 to 1382 °F) for the base material microstructure, and 875 to 1100 °C (1607 to 2012 °F) for austenite. No attempt was made to determine CTE during the on-heating transformation. CTE calculations were performed by linear fitting of dilation data within each temperature range in conjunction with **Equation 1**. The material was assumed to be isotropic.

$$\alpha_T = \left(\frac{\Delta d}{d_0}\right)\left(\frac{1}{\Delta T}\right) \quad \textbf{(1)}$$

where $\alpha_T \equiv$ Linear coefficient of thermal expansion [°C^{-1}]
$\Delta d \equiv$ Change in specimen diameter over the chosen temperature range [cm]
$d_0 \equiv$ Initial specimen diameter [cm]
$\Delta T \equiv$ Temperature range [°C]

The temperature-dependent density (ρ) was calculated using a theoretical cubic volume element under the assumption of isotropic thermal expansion:

$$\rho(T) = \frac{\rho_0 V_0}{V(T)} \quad \textbf{(2)}$$

where $\rho(T)$ ≡ Density at temperature T [g/cm^{-3}]
ρ_0 ≡ Room temperature density provided by TPRL [g/cm^3]
V_0 ≡ Room temperature volume of the theoretical cubic element [cm^3]
$V(T)$ ≡ Volume of the theoretical cubic element at temperature T [cm^3]

V_0 was calculated assuming a side length equal to the room temperature width of the dilatometry specimens. This value was chosen because, as shown in **Figure 1**, it corresponds to the starting gauge length for the dilatometer used to measure thermal expansion. A theoretical cubic volume element was chosen instead of the actual specimen dimensions to subvert potential complications with measuring dimensions that were not directly measured by the dilatometer (*e.g.*, the effect of thermal gradients on measurement of the specimen's longitudinal expansion). V_T was simply calculated by:

$$V(T) = [w(T)]^3 \quad \textbf{(3)}$$

where $w(T)$ ≡ Dilatometer-measured specimen width at temperature T [cm]

This method allowed calculation of the density through the austenite transformation. Finally, thermal conductivity (λ) as a function of temperature was then calculated by using **Equation 4**:

$$\lambda = \rho \cdot c_p \cdot \alpha \quad \textbf{(4)}$$

where λ ≡ Thermal conductivity [W/cm-°C]
c_p ≡ Specific heat capacity [J/g-°C]
ρ_0 ≡ Room temperature density [g/cm^3]
α ≡ Thermal diffusivity [cm^2/s]

Thermo-Mechanical Property Analysis

Tensile specimens were machined from the HY-100 plates according to the dimensions shown in **Figure 2a**. All specimens were extracted with their length perpendicular to the rolling direction of the plate. Elastic modulus, yield strength, and flow stress were identified as the required mechanical properties from room temperature up to near-melting. On-heating tension testing of the HY-100 base material at temperatures between 22 and 1100 °C (72 and 2012 °F) was performed by the Ohio State University using their Gleeble 3800. Specimens were spray painted with an yttrium oxide (Y_2O_3) solvent-based paint to provide a contrast between the black and white speckle pattern sprayed onto the face of specimens, as shown in **Figure 2b**. Tensile testing was carried out using digital image correlation in lieu of a contact extensometer. Room temperature testing was performed in accordance with ASTM A370 [15], and elevated temperature testing was performed in accordance with ASTM E21 [16].

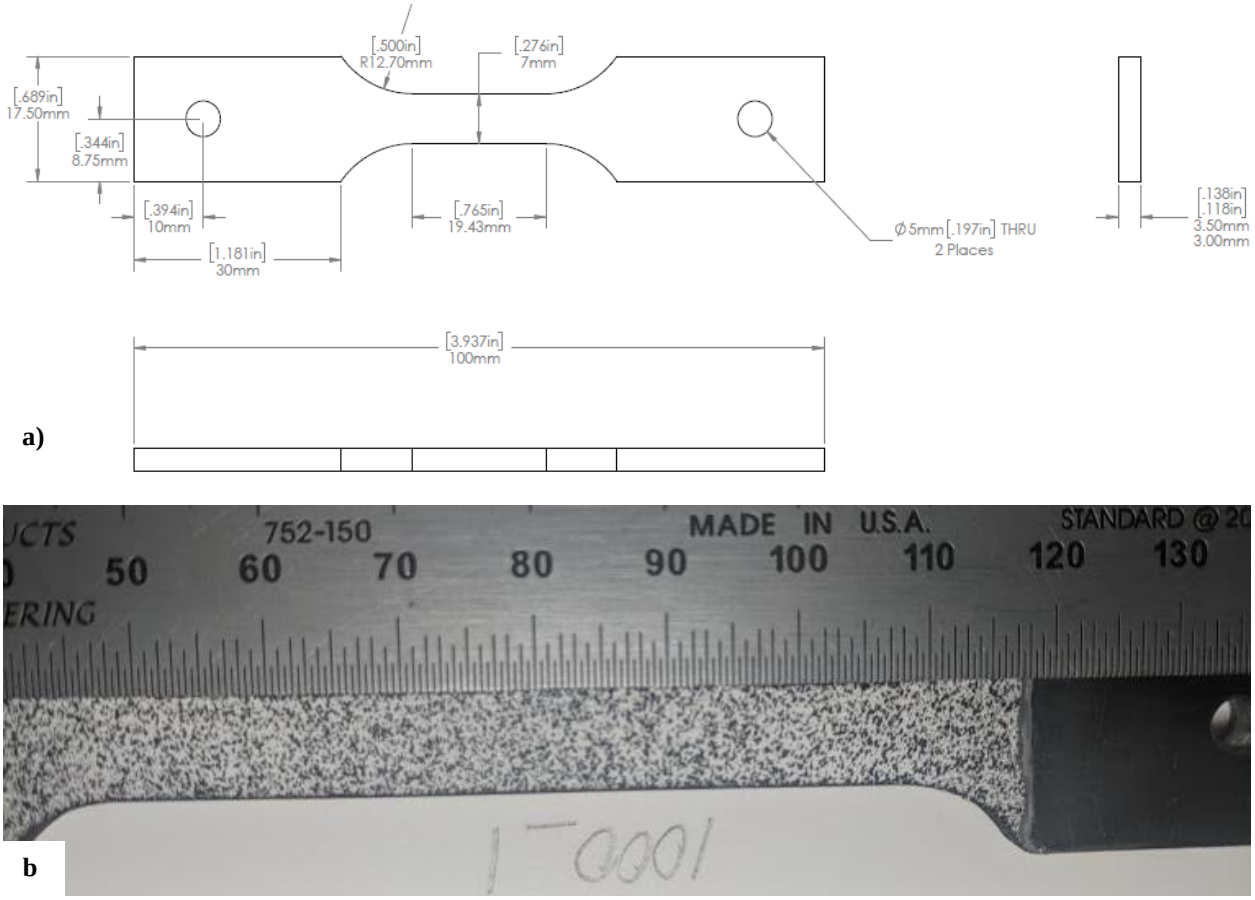

Figure 2. Tensile specimens for Gleeble-based mechanical testing of HY-100 steel: **a)** dimensions for single-reduced gauge section, **b)** sample speckle pattern for DIC testing (dimensions in mm).

On-cooling mechanical properties were measured using the Gleeble 3500 at NSWCCD. Prior to mechanical testing, the specimens were thermally cycled to generate different initial microstructures based on the results of the CCT diagram development described above. For HY-100, microstructural analysis indicated that substantially different microstructures formed when the material was cooled at 1, 10, 25, and 100 °C/s (1.8, 18, 45, and 180 °F/s). Because of programmatic time constraints, only a peak temperature of 1350 °C (2462 °F) was applied to the tensile specimens. All specimens were heated in an argon atmosphere, and forced air was used to meet cooling rates of 10 °C/s (18 °F/s) and above. All specimens were cooled to room temperature, and thereafter a contact longitudinal extensometer was affixed. The specimens were then reheated to the test temperature at a rate of 10 °C/s (18 °F/s) and soaked for 10 sec. before being pulled to failure in crosshead control mode at strain rates targeting those prescribed in ASTM E21 [16]. The crosshead displacement rate used was 0.30 mm/min (0.012 in/min). It is acknowledged that this is not the most representative method of testing for welding-related applications because the stresses that develop during welding do so rapidly and while the material is cooling and undergoing phase transformations. However, given the programmatic intent of establishing the mechanical behavior of specific microstructures and the need to avoid exposing the strain measurement device to exceedingly high temperatures, the method of cooling to room temperature and tension testing after reheating was determined to be an acceptable compromise. In cases where the induced microstructure was stronger than the base material, a second reduced gauge section was machined in the

specimen prior to testing to ensure specimen fracture in the region of interest. This revised specimen geometry is shown in **Figure 3**.

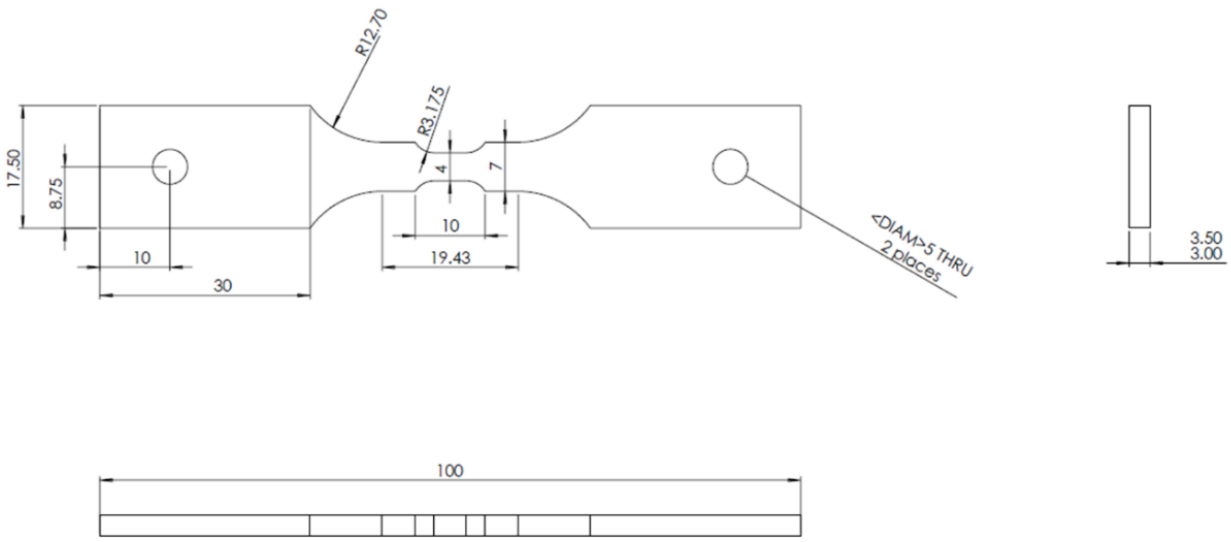

Figure 3. Specimen dimensions for Gleeble-based mechanical testing of HY-100 steel for a double-reduced gauge section (dimensions in mm).

Thermal cycling and subsequent tensile testing were performed using the Gleeble apparatus's "Pocket Jaw" setup with minimal contact stainless steel grips used to fixture the specimen. These grips were selected to minimize the longitudinal thermal gradient in the gauge length of the specimens during testing. Graphite foil was inserted between the specimen and the grips to further minimize the thermal gradient. Strain in the specimens was measured using a contact longitudinal extensometer, and the initial gauge length for the tests varied between 8 and 10 mm (0.31 and 0.39 in.). Elevated temperature tension tests were performed in an argon atmosphere. Preliminary testing as part of the DH36 test program [5] indicated that for this setup, the temperature variation across the initial gauge length was 10 to 30 °C (18 to 54 °F). The typical experimental setup for the dilatometry testing is shown in **Figure 4**.

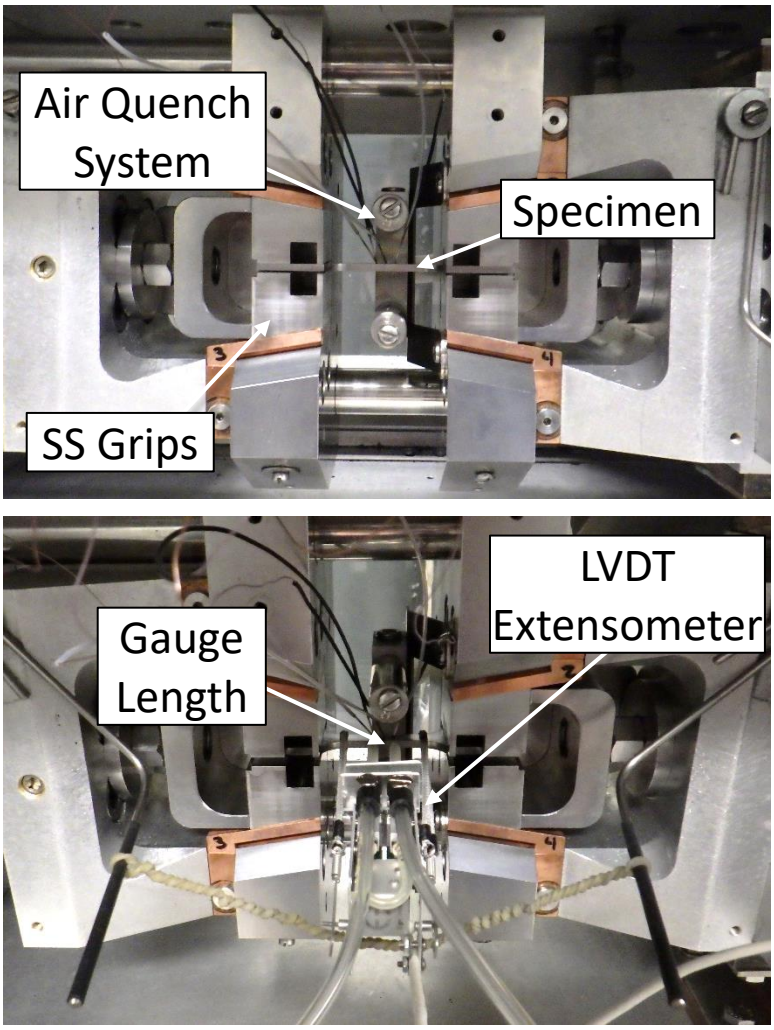

Figure 4. Photographs of the Gleeble-based mechanical testing experimental set-up.

Fabrication of Welded Specimens

Additionally, two sets of HY-100 plates were welded together at Ingalls and sent to OSU to investigate the plate, weld, and heat-affected zone (HAZ) microstructures. The first set of plates were welded using submerged arc welding (SAW) in a two-sided butt joint configuration, as shown in **Figure 5**. The second set of plates were welded using flux cored arc welding (FCAW) in a two-sided tee-joint configuration. Welding parameters for both scenarios are given in **Table 2**. These weldments enabled correlation of the microstructures generated through thermal simulations for the CCT curves with those produced from arc welding. Each weldment is representative of two primary types of joints used at Ingalls for structural welds: seaming butt joints and fillet joint stiffener welds. These joint types were also the focus of larger fabrication efforts described in other tasks within the greater LIFT project as described in [17].

Figure 5. Representative butt joint weldment of HY-100 material investigated for plate, weld, and HAZ microstructures. The tee joint configuration was not imaged prior to cross-sectioning, but the shape and size is representative of the previous marine steel alloy efforts.

Table 2. Nominal Welding Parameters used to Fabricate HY-100 Butt and Tee Joints

	Butt Joint	**Tee Joint**
Welding Process	Submerged arc (SAW)	Flux cored arc (FCAW)
Current (A)	325 / 350 (1st / 2nd Pass)	190
Voltage (V)	30	27.5
Travel Speed (mm/s [in/min])	10.6 (25)	7.62 (18)
Heat Input (kJ/mm [kJ/in])	0.92 / 0.99 (23.4 / 25.2)	0.69 (17.4)
Consumable Designation(s)	MIL-E-23765/2E: MIL-100S-1	AWS A5.20 E71T-1
Filler Wire Diameter (mm [in])	3.175 (0.125)	1.32 (0.052)
Interpass Temperature, Max. (°C [°F])	93 (200)	107 (225)

Microstructural Analysis

To quantify and characterize the HY-100 weldment microstructures, a cross-section of each of the weldments was analyzed. Each specimen was metallographically prepared to a final polish of 0.05 μm using standard techniques and etched by immersion in 4% Picral (4 g picric acid dissolved in 100 mL ethanol) for approximately 10 seconds followed by immersion in 2% Nital (2 mL nitric acid in 98 mL of ethanol) for 5 seconds. Metallographic preparation was followed by light optical microscopy (LOM) and scanning electron microscopy (SEM) analysis. Vickers microhardness values measured using a load of

200 g (7.05 oz.) were taken from the fusion zone through the HAZ to the base material for both weldments.

Thermally cycled specimens from the HAZ CCT diagram development were metallographically prepared using the same procedure. Identification and phase fraction measurement of the microstructural constituents in each specimen were evaluated using image analysis through LOM and SEM. Vickers microhardness testing was also used to determine the hardness of the constituent(s) in each CCT specimen. This analysis facilitated proper CCT analysis, provided phase fraction input for the HY-100 material property database, and helped determine which thermal cycles were the most appropriate for application in the mechanical testing portion of the program described above.

RESULTS AND DISCUSSION

Chemical Composition

Table 3 shows the averaged results of base material chemistry measurements for the HY-100 plate conducted at OSU and NSWCCD, plus manufacturer's plate certification values (shown in **Appendix A**) and the NAVSEA Tech Pub 300 HY-100 specifications [4]. The measured chemical composition values generally agreed with the manufacturer's plate certification with the exception of the carbon concentration measured at OSU. Subsequent analysis performed at NSWCCD using the more accurate combustion method for analyzing carbon found the carbon content to be well within the limits of the specification. However, sulfur content was at or slightly above the maximum allowable limit outlined by the specification. The carbon equivalency number (CEN) was calculated according to Yurioka *et al.* [18]. The individual measurements made by OSU and NSWCCD to obtain the average composition values are located in **Appendix A**.

Table 3. Chemical Composition of HY-100 Material (wt.%)

Type	C	Mn	P	S	Si	Ni	Cr	Mo
Measured Avg. (NSWCCD)	0.17	0.32	0.007	0.004	0.23	2.6	1.57	0.25
Measured Avg. (OSU)	0.07	0.29	0.005	0.0007	0.22	2.92	1.25	0.26
Plate Certificate	0.15	0.30	0.007	0.002	0.21	2.44	1.24	0.25
Tech Pub 300 [4]	0.08-0.18	0.10-0.40	<0.015	<0.004	0.15-0.38	2.25-3.50	1.00-1.80	0.20-0.60

Type	Cu	V	Ti	Al	Nb	Sb	As	Sn	Fe	CEN [18]
Measured Avg. (NSWCCD)	0.16	0.0003	---	0.019	0.0001	---	---	---	Bal	0.693
Measured Avg. (OSU)	0.15	0.005	0.002	0.018	0.002	0.001	---	0.009	Bal	0.363
Plate Certificate	0.15	0.004	0.001	0.013	0.001	0.0010	0.0030	0.007	Bal	0.583
Tech Pub 300 [4]	<0.25	<0.03	<0.02	---	---	<0.025	<0.025	<0.030	Bal	

Solidus and Liquidus Analysis

Solidus and liquidus temperatures were not experimentally measured for HY-100 base material as part of this project. A report by Concurrent Technologies Corporation (CTC) as part of a previous Navy Manufacturing Technology (ManTech) program with the Naval Metalworking Center from the late-1990s gave an on-heating solidus of 1508 °C (2746 °F) and liquidus of 1525 °C (2779 °F) when tested at a heating rate of 10 °C/min (18 °F/min) using differential thermal analysis (DTA) techniques [19]. At a higher heating rate of 50 °C/min (90 °F/min), these values shifted to an on-heating solidus of 1497 °C (2727 °F) and liquidus of 1534 °C (2793 °F) [19]. However, for on-cooling analysis, these values shifted to a solidus of 1489 °C (2712 °F) and liquidus of 1496 °C (2725 °F) at 10 °C/min (18 °F/min) and a solidus of 1453 °C (2647 °F) and liquidus of 1495 °C (2723 °F) at 50 °C/min (90 °F/min) [19]. In comparison, a Honeywell report from 1987 stated a melting temperature of 1520 °C (2768 °F) [20].

Base Metal Microstructure

The microstructure of the HY-100 base metal is shown in the light optical micrograph in **Figure 6**. The microstructure is tempered martensite. The manufacturer subjected the plate material to a hardening heat treatment at a nominal temperature of 904 °C (1660 °F) for 14 minutes followed by quenching, then tempered it at 638 °C (1180 °F) for 26 minutes followed by air cooling to room temperature. The average Vickers microhardness of the base metal was 281 ± 8.1 HV_{200}. In comparison, Yue *et al.* measured a value of 283 HV, though using a 1 kg load [21].

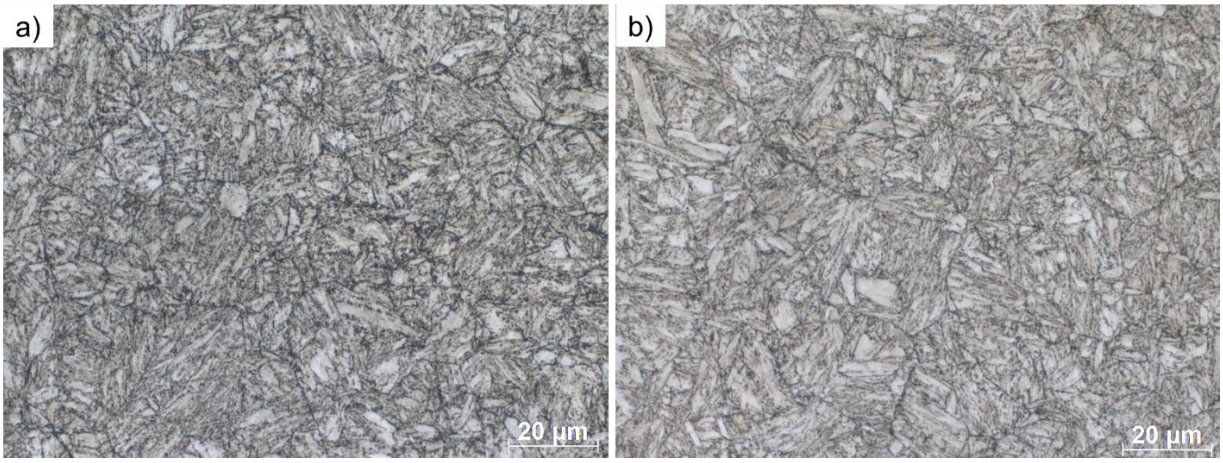

Figure 6. Representative micrograph of HY-100 steel plate base metal microstructure etched with 4% Picral and 2% Nital, shown at 1000x magnification using LOM with the imaged plane normal to the **a)** transverse plate direction and **b)** the longitudinal direction.

Observing the HY-100 base metal in both the longitudinal and transverse planes revealed no evidence of anisotropy. The heat treat effectively erased evidence of prior austenite grains and no attempt to quantify prior austenite grain size was made. LOM techniques revealed fine precipitates but no attempt was made to positively identify them. The relatively high carbon content of this alloy and the typical behavior of tempered steel both suggest that these are carbides.

Heat Affected Zone Phase Transformation Analysis

Dilation Curve Analysis Method

Figure 7 shows a representative on-heating portion of a Gleeble-produced dilatometry curve generated by NSWCCD. The black curve (left axis) represents the change in sample diameter (*i.e.*, dilation) with temperature, with non-linearity in the black dilation curve corresponding to a phase transformation. Instances at which non-linearity occurs can be highlighted by graphing the derivative of the dilation curve with respect to temperature, shown by the blue curve (right axis). Simple linear extrapolations of the black dilation curve are shown by the green lines as a secondary method for pinpointing the temperatures at which nonlinearity occurs. In this case, the transformation of interest is that of the HY-100 base metal microstructure to austenite.

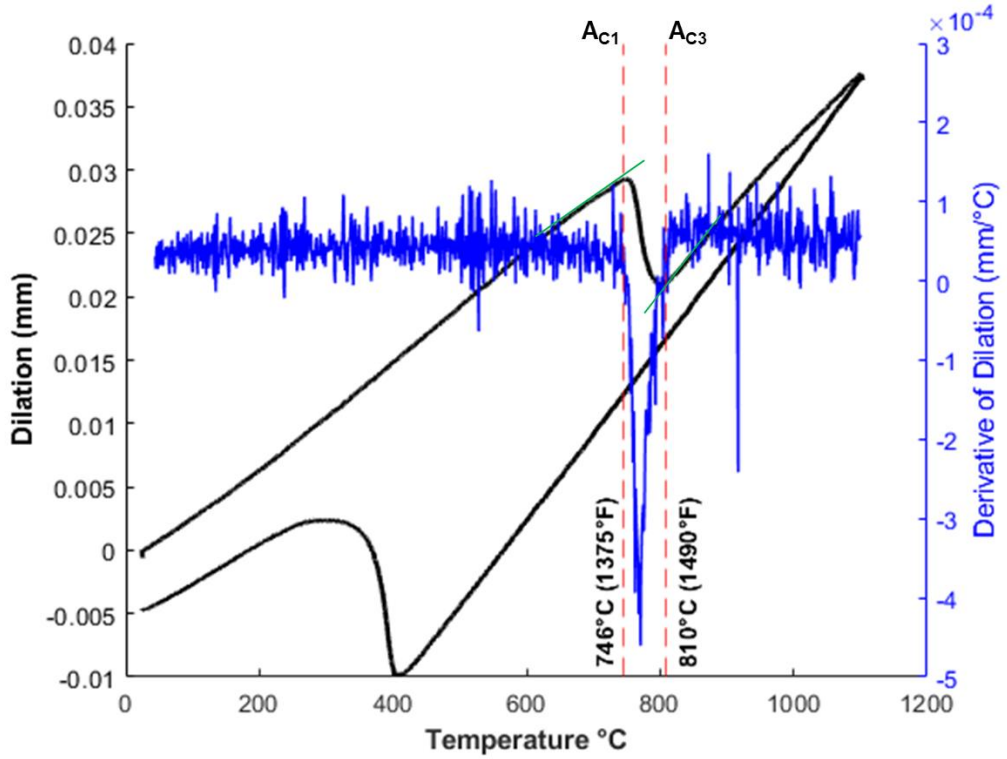

Figure 7. Representative on-heating dilatometry curve for HY-100 steel, showing the linear extrapolation and derivative curve methods for evaluating the ferrite to austenite reaction. Black curve, left axis: dilation data. Blue curve, right axis: derivative of dilation data. Green lines: extrapolation lines for determining transformation start (A_{c1}) and finish (A_{c3}) temperatures.

Two methods for extracting start and finish temperatures for phase transformations from Gleeble dilatometry data are commonly used. The first method involves superimposing a straight line of matching slope along the low temperature portion of the dilation curve and extrapolating it past the transformation. The point at which the experimental data begin to deviate from the straight line is then taken as the transformation start temperature. The same technique is then used to find the transformation finish temperature, with the straight line being extrapolated from the high-temperature portion of the curve after the transformation. The second method involves calculating and plotting the derivative of the dilation curve. Then the points at which the derivative begins to deviate from a constant value are taken as the transformation start and finish temperatures. Both methods for determining phase transformation

temperatures are inherently somewhat subjective, and both also have advantages and disadvantages. The linear extrapolation method is faster and easier to interpret but is difficult to use when multiple transformations occur. The derivative method is more quantitative and can more easily distinguish multiple transformations but can be difficult to interpret when the dilation data are noisy. For this work, the linear extrapolation method was chosen as the primary method of data analysis, and the derivative method was used as a complementary technique for distinguishing concurrent phase transformations. Both methods are shown in **Figure 7**, where the derivative curve is displayed in blue and the linear extrapolations are displayed in green.

Austenite Transformation Temperature Measurement

Figure 8 presents the variation in austenite transformation behavior as a function of heating rate for HY-100 base material. As shown, the austenite transformation start temperature (A_{c1}) is relatively insensitive to heating rate. This is expected, as the tempered state of the base material leaves very little inhomogeneity and requires minimal mass diffusion to take place prior to austenite transformation. The sample heated at 100 °C/s (212 °F/s) appears to be an outlier in this dataset as a result of experimental error. This specimen was also measured at a lower data sampling rate which may have affected the accuracy of measurement. Another possible explanation for recording artificially high values is because of misalignment of the dilatometer with the thermocouple. Recall that the sample is heated via resistive heating, which produces a thermal gradient across the length of the specimen. In the case that the dilatometer placement corresponds to an adjacent, cooler region of the dilatometry sample the heating can lagged slightly. By the time A_{c1} is reached at the dilatometer, the thermocouples report a higher temperature in the hotter adjacent region. These data are important for the refinement of welding simulation results because different regions of a weldment and its HAZ are subject to significantly different heating rates during the welding process. The on-heating transformation behavior must be incorporated in order to accurately predict which areas around the weld will transform to austenite and will therefore be subject to re-transformation (and associated changes in mechanical properties and residual stresses) during cooling. Data found from Yue *et al.* are included for comparison [21]. The raw data points for **Figure 8** can be found in **Table 10** within **Appendix B**.

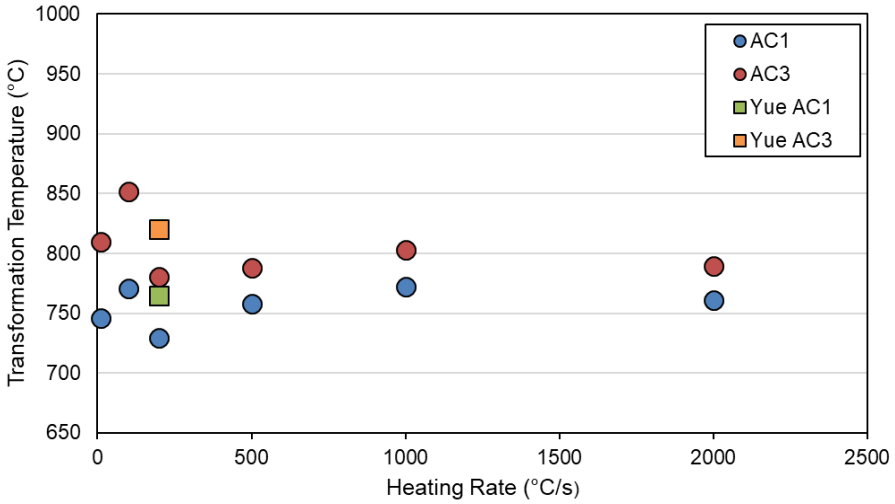

Figure 8. Variation in austenite transformation start and finish temperatures with heating rate for HY-100 material.

Continuous Cooling Transformation Diagrams

CCT diagrams assembled from dilatometry of HY-100 thermally cycled to peak temperatures representative of the four selected HAZ regions are given in **Figures 9-12**. The austenite transformation temperatures described above resulted in selection of an ICHAZ simulation temperature of 785 °C (1445 °F) for HY-100, which was the same value used for HY-80 [9], 5 °C (9 °F) lower than that used for HSLA-100 [8], 40 °C (72 °F) lower than that used for HSLA-65 [6] and HSLA-80 [7], and 90 °C (162 °F) lower than the temperature used for DH36 [5]. The A_{c1} and A_{c3} temperatures labeled on the CCT diagrams are averages calculated from the individual A_{c1} and A_{c3} values for all of the CCT specimens. The black curves are the actual specimen cooling curves. The target cooling rates for all specimens were maintained through the on-cooling phase transformations. The raw data for these figures are given in **Table 11-14** of **Appendix B**, and the individual dilation curves are given in **Figures 38-61** of **Appendix B**.

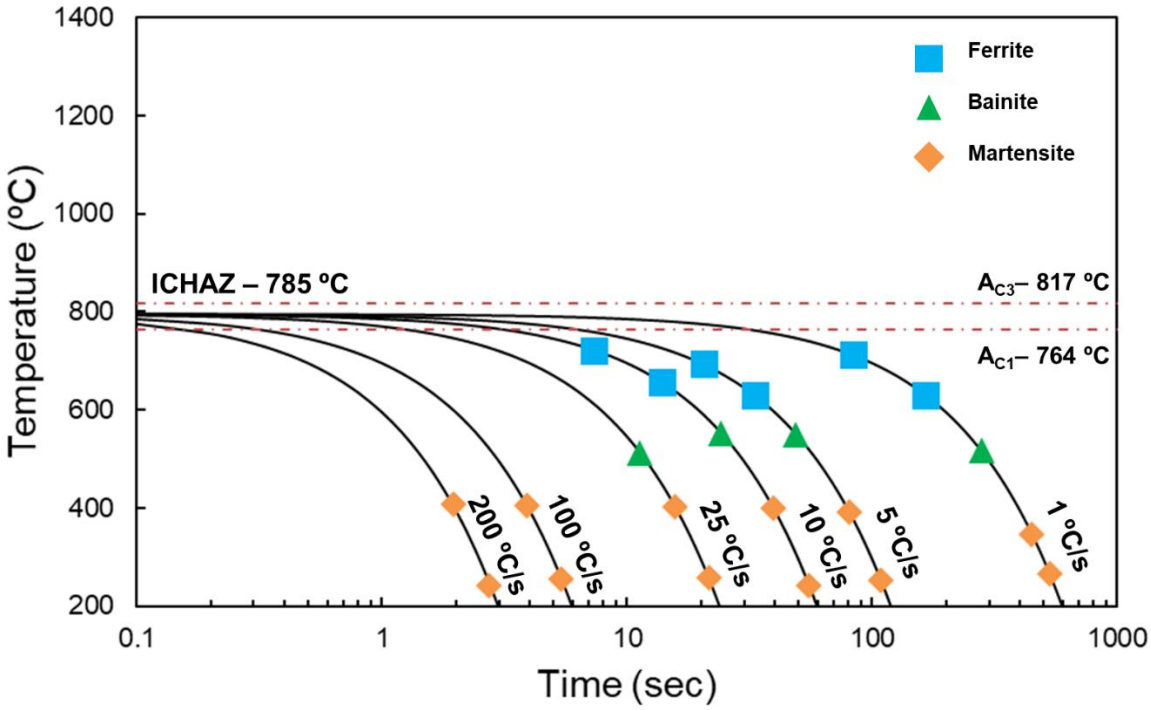

Figure 9. CCT diagram for HY-100 heated to peak temperature of 785 °C (1445 °F).

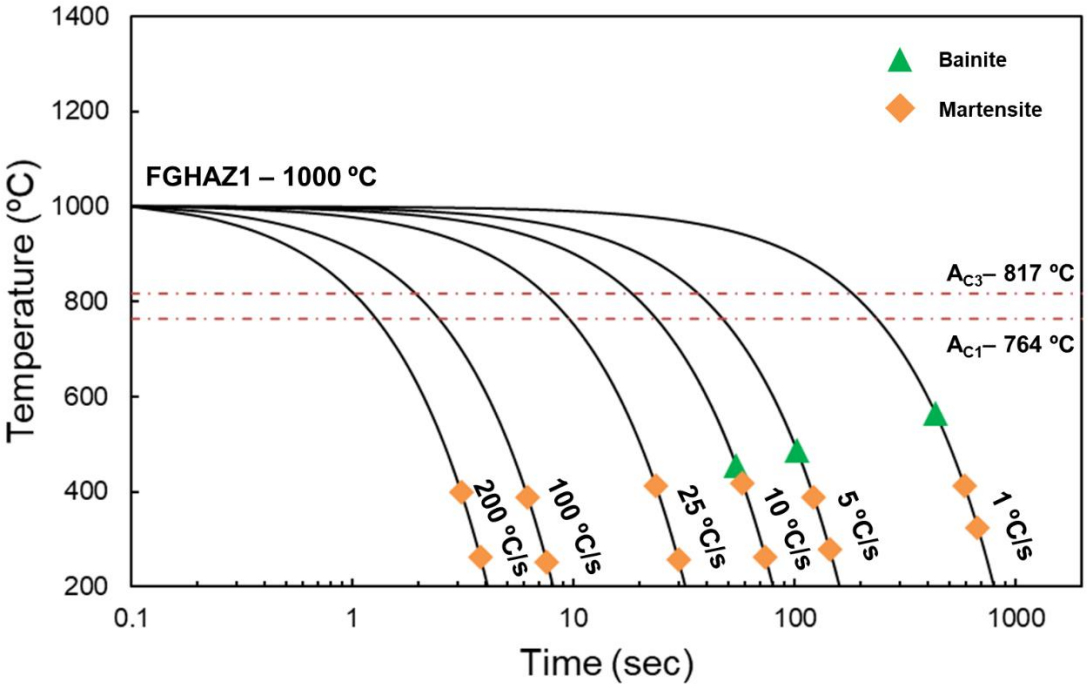

Figure 10. CCT diagram for HY-100 heated to peak temperature of 1000 °C (1832 °F).

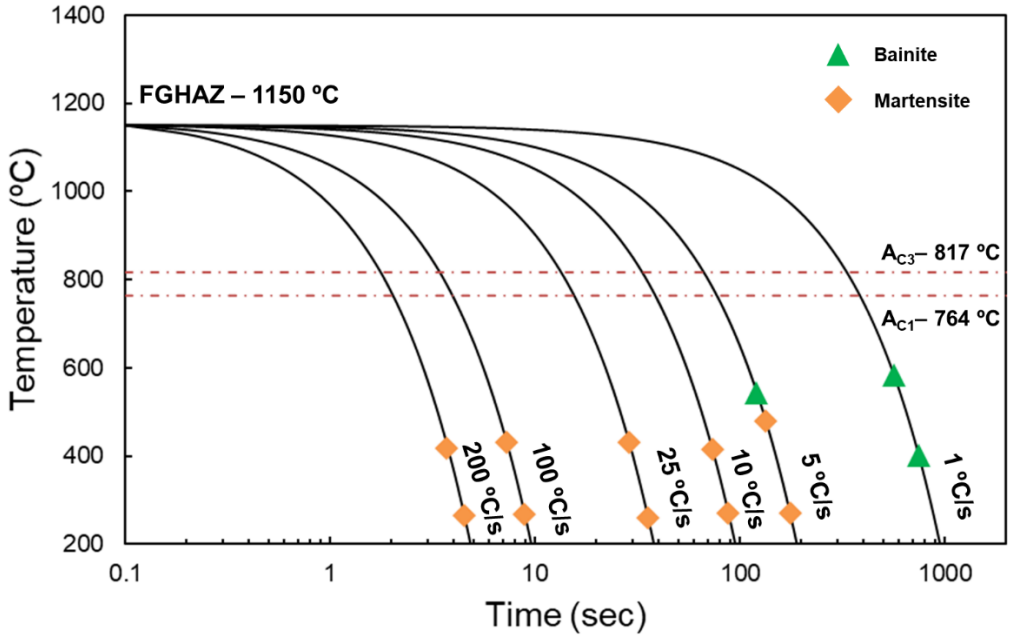

Figure 11. CCT diagram for HY-100 heated to peak temperature of 1150 °C (2102 °F).

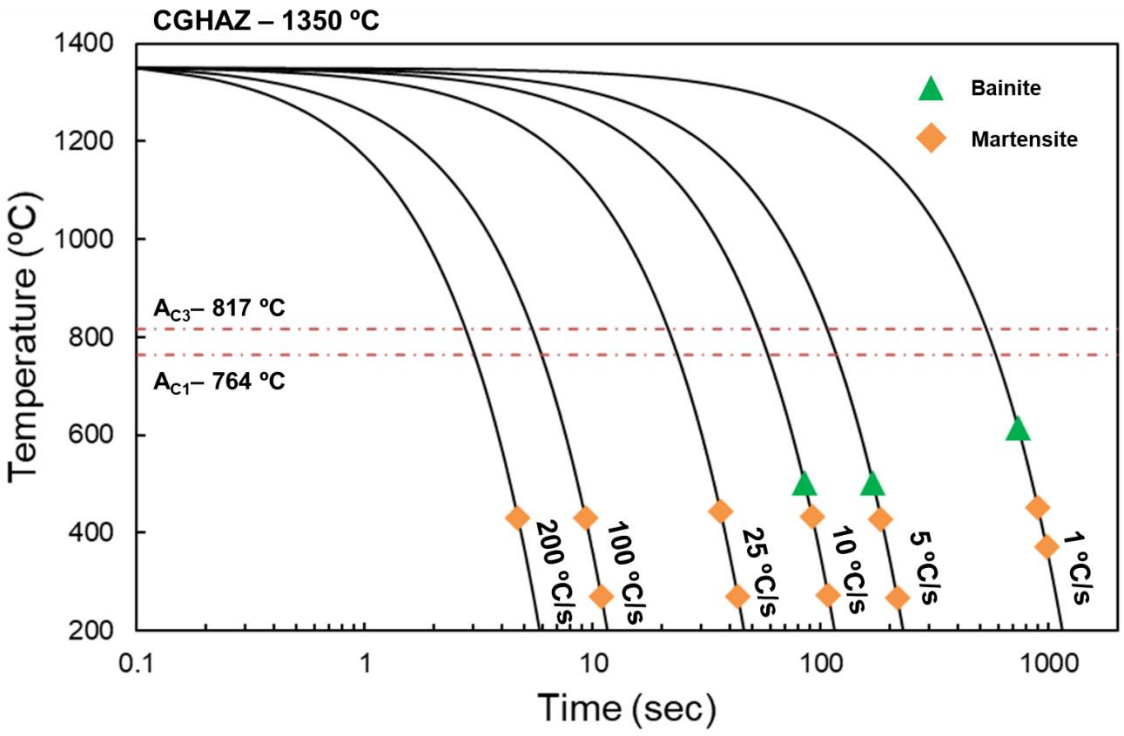

Figure 12. CCT diagram for HY-100 heated to peak temperature of 1350 °C (2462 °F).

The colored symbols in **Figures 9-12** correspond to the start and finish temperatures for the various on-cooling phase transformations. Simulated HAZ regions were subject to up to three regimes of on-cooling transformation start temperatures across the cooling rate range assessed in this work as shown in **Figure 13-Figure 15**. The first transformation occurred at high temperatures and was associated with ferrite formation, which was only observed for slow cooling conditions (1-10 °C/s [1.8-18 °F/s]) in the ICHAZ sample, as illustrated below in **Figure 13**. In general, the ferrite start transformation temperature is expected to be suppressed as cooling rate increased, due to the diffusion-based nature of ferritic transformations. No pattern was discernible for the three cases in which ferrite appeared, likely due to the sensitivity of ICHAZ transformations to experimental conditions (*e.g.*, peak temperature, cooling rate) that are difficult to perfectly reproduce for a partial transformation. This is exacerbated by the extremely narrow region of the physical sample that reaches peak temperature. In this case, even a minor offset between the dilatometer and the thermocouples attached to the specimen may have a drastic effect on recorded phase transformations. At the time of testing a laser dilatometer was not available to mitigate such measurement errors.

Bainite was present in all samples cooled at rates below 10 °C/s (18 °F/s) as well as those cooled at 25 °C/s (45 °F/s) with the exception of the FGHAZ simulant specimens, as is shown in **Figure 14**. Bainite largely replaced ferrite formation at intermediate cooling rates in the ICHAZ specimens and at slow cooling rates for higher peak temperatures. Martensite formed for all conditions tested, though was only present in trace amounts in in FGHAZ specimens cooled at 1 °C/s (1.8 °F/s). Martensite was the only phase formed at 100-200 °C/s (180-360 °F/s) for all peak temperatures. There is no definitive relationship shown in these data between M_s and cooling rate, but there is a slight upward trend with respect to peak temperature. These transformation start temperatures are illustrated in **Figure 15**. An increase in M_s with respect to peak temperature may be a consequence of increased chemical homogeneity due to more dissolution of carbon and alloying elements. However, more experiments are

required to confirm this trend definitively considering the same result was not observed in the chemically similar HY-80 alloy [9].

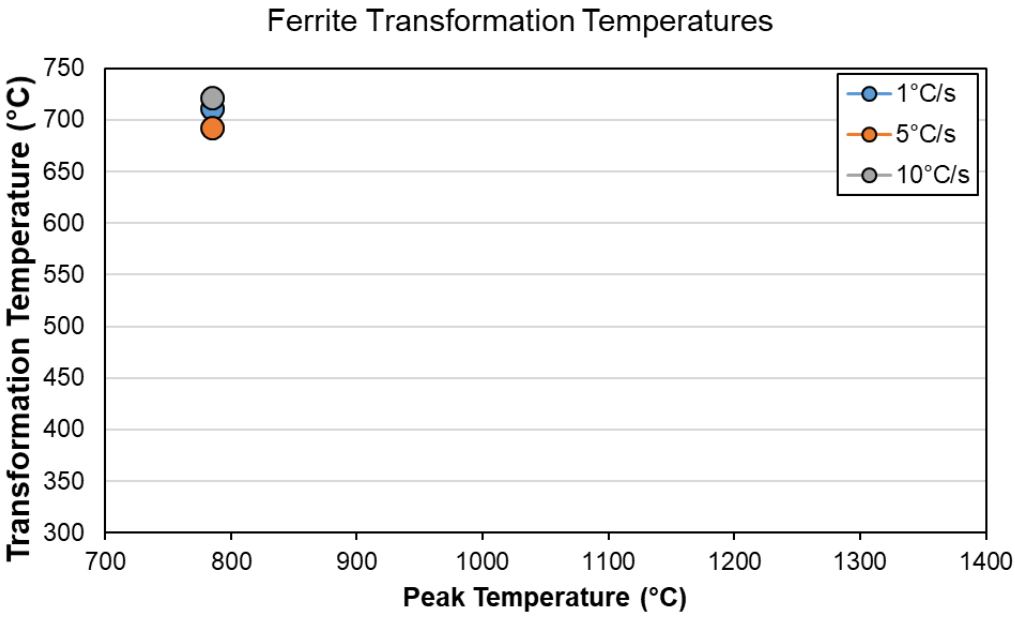

Figure 13. Variation of start temperature for the ferrite transformation shown in **Figures 9-12**.

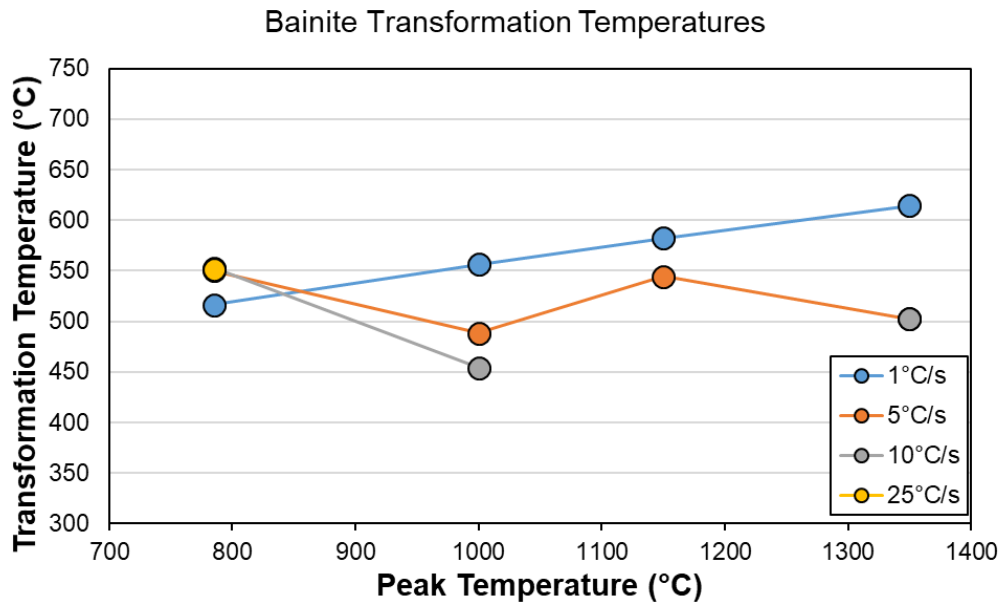

Figure 14. Variation of start temperature for the bainite transformation shown in **Figures 9-12**.

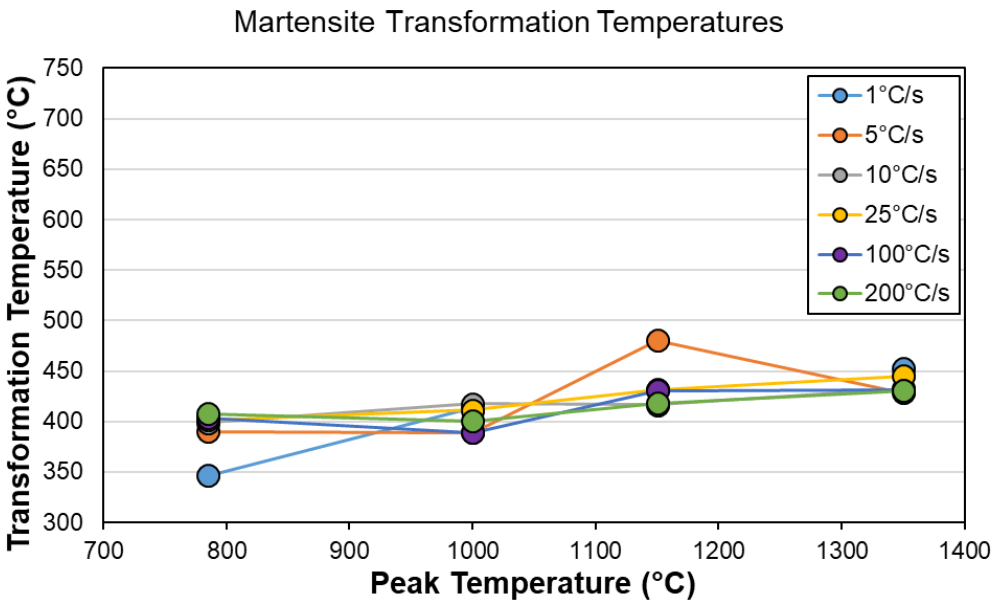

Figure 15. Variation of start temperature for the martensite transformation shown in **Figures 9-12**.

Various constitutive equations for predicting the start temperatures for bainite and martensite transformations based on alloy chemistry are available in the literature [22] [23]. Such models are generally oversimplifications and often are only accurate for alloys similar to those used to create them, but they can act as a guide for reasonable temperatures at which to expect formation of intermediate and low temperature phases. As such, the models developed by Capdevilla *et al.* [24] and Kirkaldy [25] were applied to the measured HY-100 composition given in **Table 3**:

$$M_s = 491.05 - 302.6w_C - 30.6w_{Mn} - 16.6w_{Ni} - 8.9w_{Cr} + 2.4w_{Mo} - 11.3w_{Cu} + 8.58w_{Co} + 7.4w_W - 14.5w_{Si} \quad \textbf{(5)}$$

$$B_s = 656 - 57.7w_C - 75w_{Si} - 35w_{Mn} - 15.3w_{Ni} - 32w_{Cr} - 41.2w_{Mo} \quad \textbf{(6)}$$

where $M_s \equiv$ martensite start temperature (°C)
$B_s \equiv$ bainite start temperature (°C)
$w_i \equiv$ concentration of element i (wt%)

From **Equations 5** and **6**, the M_s and B_s temperatures for HY-100 are predicted to be 392 °C (738 °F) and 522 °C (972 °F), respectively. The predicted M_s and B_s temperatures fall within the range of transformation temperatures measured for both phases. The best agreement between measured and predicted M_s temperatures occurred at lower peak temperatures. Measured bainite start temperatures were subject to a larger spread across all specimens, however the predicted B_s temperature was in good agreement with the mean measured B_s of 532 °C (990 °F).

In order to establish the identities of the on-cooling phase transformations, LOM was performed on all dilatometry specimens and select specimens were analyzed via SEM. Micrographs collected from the dilatometry specimens are given in **Figures 62-65** of **Appendix C.** While the progression of phases shown in micrographs is readily explainable, the transformation temperatures captured by dilatometry were unreliable due to experimental error associated with contact dilatometry use on specimens with extremely steep thermal gradients. A best effort has been made identify transformation temperatures but it is recommended that additional investigations are undertaken for applications that are particularly

sensitive to ICHAZ transformations. Additionally, the measured microhardness for each specimen is shown in **Figure 16** (raw data are found in **Table 15** of **Appendix D**).

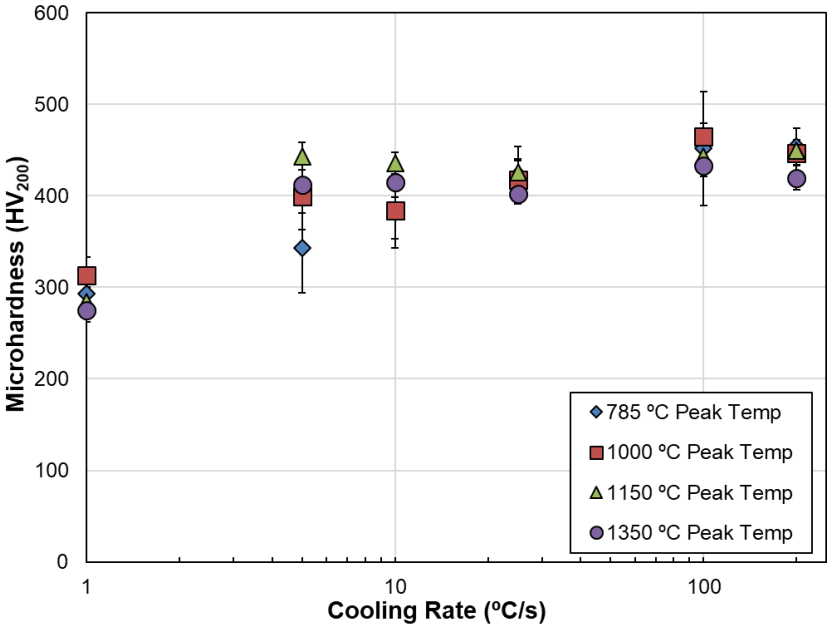

Figure 16. Measured Vickers microhardness for HY-100 dilatometry specimens as a function of peak temperature and cooling rate. Error bars are one standard deviation. Values are the average of 8-26 indents. Data are tabulated in **Table 15** of **Appendix D**.

For this discussion, the following definitions for the morphology of microstructural constituents are adopted, based on references [26] [27] [28] [29] [30]. The typical definitions for crystal structure and composition of the constituents are also assumed.

Primary ferrite (F_P) – Carbide-free grain boundary or intragranular, allotriomorphic, or idiomorphic ferrite

Martensite-austenite constituent (M/A) – Structure represented by a combination of martensite and residual austenite

Bainite (B) – General term for fine aggregates of ferrite laths or plates and cementite particles

Lath martensite (M_L) – Martensite laths with highly dislocated substructure which are grouped into larger packets

Representative micrographs of all CCT specimens heated to 785 °C (1445 °F) are shown in **Figure 62** of **Appendix C**. This temperature falls between A_{c1} and A_{c3} (764 and 817 °C [1407 and 1503 °F], respectively) and was chosen in order to achieve partial transformation to austenite prior to cooling. As such, some of the base metal microstructure was retained in these specimens. Samples cooled from 1-10 °C/s (1.8-18 °F/s) consisted of a mixture of light etching primary ferrite, dark etching bainite and tan etching martensite. Ferrite grains had a quasipolygonal morphology and occasionally formed in bands, most visible in the 5 °C/s specimen shown in **Figure 62b**. Bainitic ferrite grains were fine and globular across all three conditions with unaligned cementite dispersed inside them. A low temperature, likely martensitic, transformation was observed via dilatometry for these conditions. Due to the incomplete transformation induced by the heating profile, residual tempered martensite and M/A constituents from the base metal are also present. Optical microscopy does not provide a reliable delineation between these sources of martensite and therefore any residual M/A was considered part of the martensite phase fraction for these conditions.

As shown in **Table 4**, increasing the cooling rate from 1 to 5 °C/s resulted in a decrease in ferrite area fraction in favor of bainite and some additional martensite formation. At this cooling rate, some bainite begins to precipitate aligned cementite in discontinuous plates within the grains. At 10 °C/s, the microstructure is largely martensitic with a few remaining quasipolygonal ferrite grains and some remaining fine bainite. These changes correspond to a steady increase in average microhardness values with increase cooling rate. There is no remaining primary ferrite in the specimens cooled at 25 °C/s and above. What remains is a fine microstructure consisting of a mixture of bainite and martensite (At 25 °C/s) or pure martensite (100-200 °C/s).

Table 4. Measured Phase Fraction of HY-100 CCT Specimens Thermally Cycled to a Peak Temperature of 785 °C (1445 °F)

Cooling Rate		**Peak Temperature = 785 °C (1445 °F)**		
°C/s	**°F/s**	**F + M/A**	**B**	**M**
1	1.8	0.49	0.26	0.26
5	9	0.10	0.71	0.19
10	18	0.03	0.71	0.26
25	45	0	0.20	0.80
100	180	0	0	1
200	360	0	0	1

The microstructure becomes increasingly fine as the cooling rate increases until 200 °C/s in which the individual martensite features are largely indiscernible with optical microscopy. As a result, it is impossible to distinguish freshly formed martensite from any residual M/A remaining from the base material. However, the high hardness of the 100 and 200 °C/s microstructures indicate the presence of mostly newly-formed untempered martensite.

The next simulated HAZ region was the FGHAZ, with a peak temperature of 1000 °C (1832 °F). Representative micrographs are presented in **Figure 63** of **Appendix C**, with measured phase fractions reported in **Table 5**. These samples fully austenitized prior to cooling, eliminating the original base material microstructure. The higher peak temperature noticeably increased the prior austenite grain size which resulted in a coarsening of the microstructure relative to the ICHAZ treatment. The sample cooled at 1 °C/s (1.8 °F/s) exhibited a primarily bainitic microstructure with some martensite constituent. The bainite grains are coarse with intragranular cementite precipitates showing some signs of alignment but with substantial degeneracy. The sample cooled at 5 °C/s had a roughly equal quantity of martensite to bainite. The morphology of the bainite is notably much more uniform with fine aligned cementite plates present inside most bainitic grains. The martensitic component is discernable in the micrographs as a light tan constituent in contrast to the darker etching of the cementite in the bainite phase. While the phase fraction shifts further to a primarily martensitic microstructure at 10 °C/s, the morphologies of each phase remain largely consistent. There is notably no significant change in the microhardness values of these two conditions with respect to their relative standard deviations.

The samples cooled at 25 °C/s and above were all primarily martensitic. There is an increase in microhardness values between the samples cooled at 25 °C/s and those cooled at 100 and 200 °C/s which suggests a change in the structure that is not readily apparent based on the dilatometry or optical microscopy data. This could be the presence of some microstructurally rare bainitic ferrite or a change in the martensite morphology which increased the hardness. There is not a substantial change in hardness between 100 and 200 °C/s which is consistent with both the dilatometry data and analysis of optical micrographs.

Table 5. Measured Phase Fraction of HY-100 CCT Specimens Thermally Cycled to a Peak Temperature of 1000 °C (1832 °F)

Cooling Rate		Peak Temperature = 1000 °C (1832 °F)		
°C/s	°F/s	F + M/A	B	M
1	1.8	0	0.82	0.18
5	9	0	0.539	0.461
10	18	0	0.218	0.782
25	45	0	0	1
100	180	0	0	1
200	360	0	0	1

The third peak temperature investigated was also representative of the FGHAZ, but with a slightly higher peak temperature of 1150 °C (2102 °F). Representative micrographs are shown in **Figure 64** in **Appendix C**, with measured phase fractions reported in **Table 6**. There is a qualitative increase in packet size compared to samples heated to 1000 °C (1832 °F), indicating that the higher peak temperature allowed significant austenite grain growth. The microstructure of the sample cooled at 1 °C/s (1.8 °F/s) consisted entirely of coarse bainite with aligned cementite or M/A constituents.

Table 6. Measured Phase Fraction of HY-100 CCT Specimens Thermally Cycled to a Peak Temperature of 1150 °C (2102 °F)

Cooling Rate		Peak Temperature = 1150 °C (2102 °F)		
°C/s	°F/s	F + M/A	B	M
1	1.8	0	1	0
5	9	0	0.586	0.414
10	18	0	0	1
25	45	0	0	1
100	180	0	0	1
200	360	0	0	1

Increasing the cooling rate to 5 °C/s introduced lath martensite to the specimen at the expense of the bainitic phase. A corresponding substantial increase in hardness was observed between 1 and 5 °C/s cooling rates. The bainite had a finer spacing of aligned carbide and M/A than the slower cooled specimen. The bainite start temperature also decreased from 583 °C/s to 544 °C/s with increased cooling rate.

Samples cooled between 10-200 °C/s (18-360 °F/s) were all completely martensitic. Average microhardness values rose slightly with cooling rate, but were largely within measurement error of one another. M_s temperatures associated with these samples were slightly higher than those associated with samples cooled at the same rate but heated to a lower peak temperature, a trend that continued into the highest peak temperature specimens. This may be due to increase homogenization induced at higher temperatures over the short dwell times of these welding simulations.

The final simulated region was the CGHAZ, with a peak temperature of 1350 °C (2462 °F). Representative micrographs are shown in **Figure 65** in **Appendix C**, with measured phase fractions reported in **Table 7**. Material response to cooling rates for this peak temperature was similar to that described for a peak temperature of 1150 °C (2102 °F). Further coarsening of the microstructure was observed, likely brought about by an increase in austenite grain size relative to the prior treatments. The sample cooled at 1 °C/s was completely made up of coarse bainite with aligned second phases. This

condition had the lowest average microhardness of any peak temperature or cooling rate, likely due to the significant coarsening of the microstructure and subsequent Hall-Petch effects.

Table 7. Measured Phase Fraction of HY-100 CCT Specimens Thermally Cycled to a Peak Temperature of 1350 °C (2462 °F)

Cooling Rate		Peak Temperature = 1350 °C (2462 °F)		
°C/s	°F/s	F + M/A	B	M
1	1.8	0	1	0
5	9	0	0.302	0.698
10	18	0	0.08	0.92
25	45	0	0	1
100	180	0	0	1
200	360	0	0	1

The samples heated to 1350 °C (2462 °F) and cooled at 5 and 10 °C/s (9 and 18 °F/s) were comprised of extremely fine bainite and martensite. Volumetric fraction martensite increased with cooling rate, with the sample cooled at 10 °C/s consisting of mostly martensite. Samples cooled at 25-200 °C/s (45-360 °F/s) were each entirely martensitic. M_s temperatures continued to rise slightly for these specimens relative to the lower peak temperatures.

The phase transformation information developed here is critically important for ensuring that weld simulation software can draw on thermo-physical and thermo-mechanical property information from the appropriate phases at the appropriate times during calculations. The results in **Figures 9-15** highlight the importance of developing multiple HAZ-related CCT diagrams.

Weldment Microstructures

Metallographic specimens were removed from both weldments and analyzed in a manner similar to the Gleeble specimens. Discussion of the microstructures present correspond to the HAZ of the second pass for each weldment, as the reheating experienced by the first pass confounded the analysis and do not directly correlate with thermal cycles undergone by Gleeble CCT specimens, making them unsuitable for the intended purpose of experimental validation.

The fusion zone for each joint configuration was a mixture of coarse primary ferrite, acicular ferrite, and unidentified carbides. **Figure 17** presents representative micrographs for the butt joint and tee joint fusion zones. Microhardness values ranged from approximately 240-300 HV_{200}. It is noted that the microstructure is finer in the butt joint fusion zone, while the fusion zone of the tee joint has more coarse primary ferrite grains. This is reflective of the two different processes used to deposit the welds, with submerged arc welding (SAW) used for the butt joint and flux-cored arc welding (FCAW) used for the tee joint. Specific welding parameters are provided in **Table 2**. Heat input, filler wire diameter, and interpass temperature were different for each weldment and each likely contributed to differences in thermal histories that would drive variation in resulting microstructure. It is likely that the weld metal associated with the butt joint cooled more rapidly than the tee joint, allowing less time for nucleation and growth of primary ferrite grains and instead favoring acicular ferrite formation.

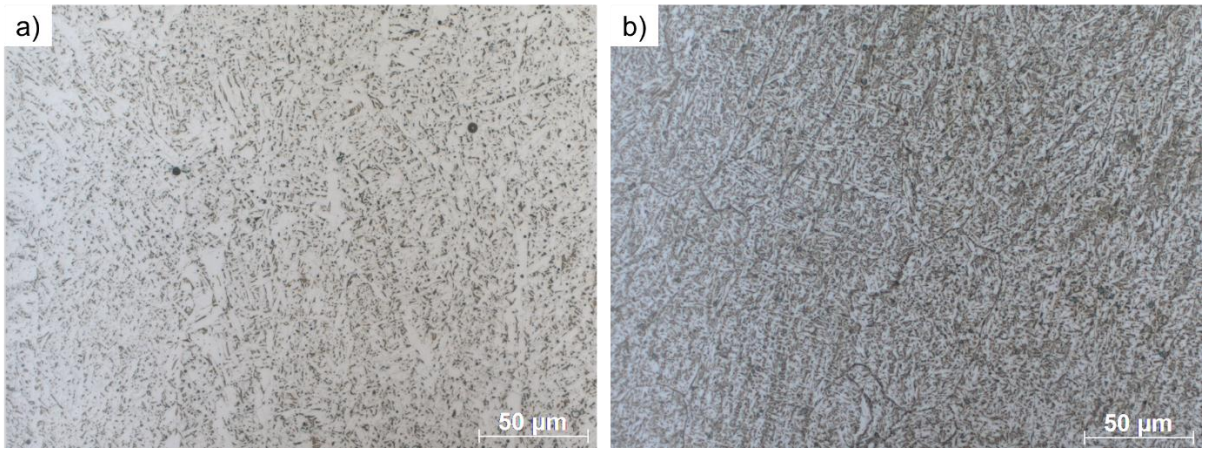

Figure 17. Representative microstructures of the second pass fusion zone for the **a)** tee joint and **b)** butt joint configuration.

Representative HAZ microstructures for the second pass of the HY-100 butt joint are presented in **Figure 18**. A microhardness map with truncated color scale is provided in **Figure 19**. The map shows measurement values for indents spaces at intervals of 500 µm in both horizontal and vertical directions. The raw values for this map are provided in **Table 16** in **Appendix D**: Microhardness Measurements. The CGHAZ of the butt joint weldment was subject to substantial hardening, with hardness values ranging from 300 HV_{200} nearest to the fusion zone and between 350-400 HV_{200} near the FGHAZ. Cooling was rapid enough to result in a CGHAZ largely made up of coarse martensite, show in **Figure 18a**. A peak hardness value of 478 HV_{200} was observed in the FGHAZ nearest to the CGHAZ. The microstructure in this region is made up of very fine mixed martensite and bainite, with more martensite closer to the fusion zone (**Figure 18b**) and more bainite farther away(**Figure 18c**). The drastic increase in hardness is attributed to a Hall-Petch effect from the decrease in grain size. The ICHAZ region shown in **Figure 18d** consists of a mix of fine martensite and bainite interspersed with rows of ferrite grains. This microstructure is similar to the 5 ºC/s (9 ºF/s) cooled ICHAZ specimen produced via the Gleeble. The hardness in this region was only a small amount higher than the base metal, with a hardness around 300 HV_{200}.

Representative HAZ microstructures for the second pass of the HY-100 tee joint are presented in **Figure 20**. A microhardness map with full-range color scale is provided in **Figure 21**, showing a map of indents spaced at intervals of 500 µm in both the horizontal and vertical directions. Numerical values are provided in **Table 17** in **Appendix D**. Tee joint HAZ microhardness was in general slightly higher than those in the butt joint, likely due to thermal cycle differences driven by the two welding processes. The heat input associated with butt joint was higher (0.92-0.99 kJ/mm compared to 0.69 kJ/mm) and the process is associated with a blanket of granular flux on the joint. Thus not only was more heat put into the butt joint, but the flux likely acted as an insulator, reducing cooling rate. This is reflected in the bainitic CGHAZ of the butt joint, whereas the tee joint CGHAZ was composed of martensite.

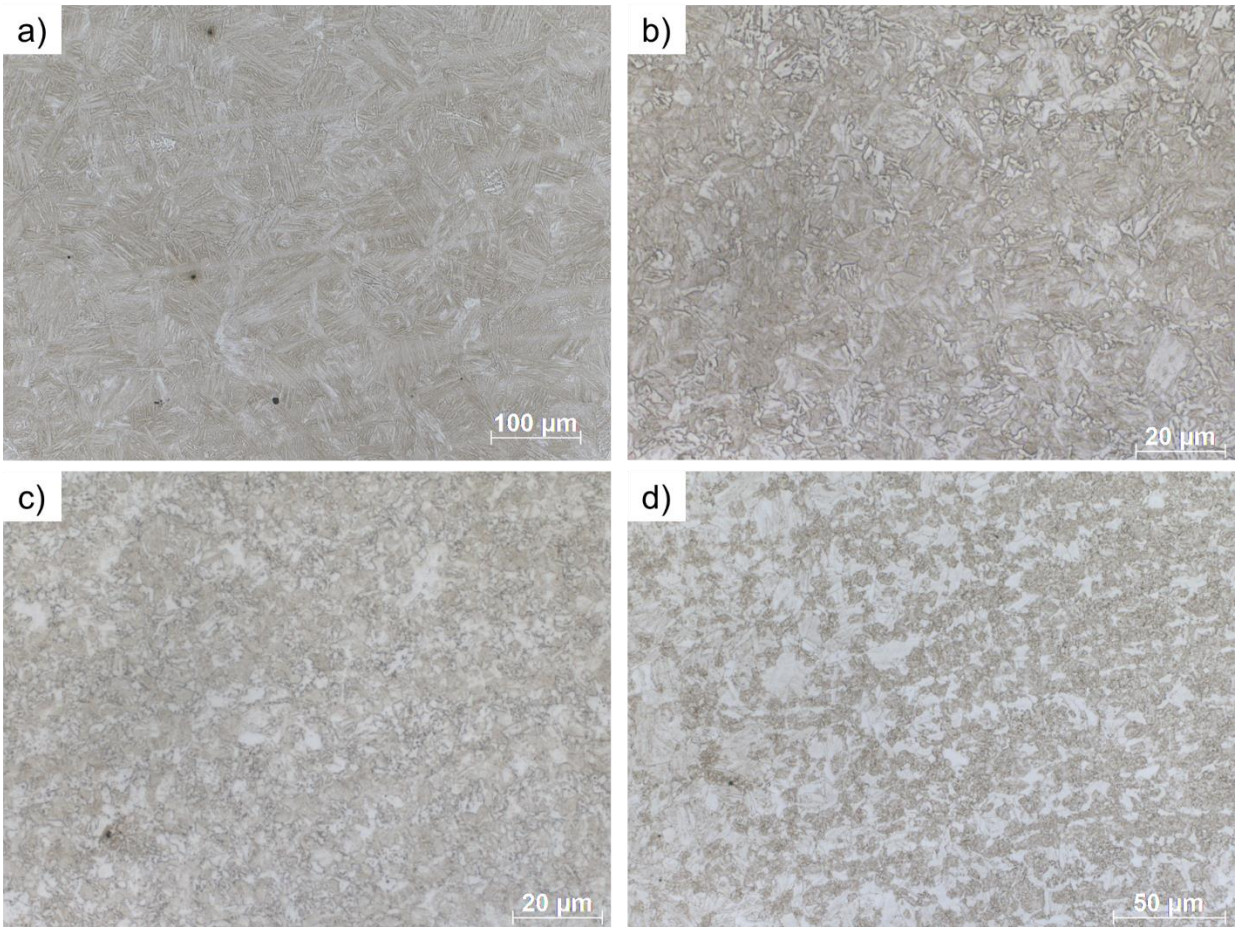

Figure 18. Representative light optical micrographs associated with the second pass of the HY-100 butt joint **a)** CGHAZ, **b)** FGHAZ close to the CGHAZ, **c)** FGHAZ close to the ICHAZ, and **d)** ICHAZ. Note the change in scale between images.

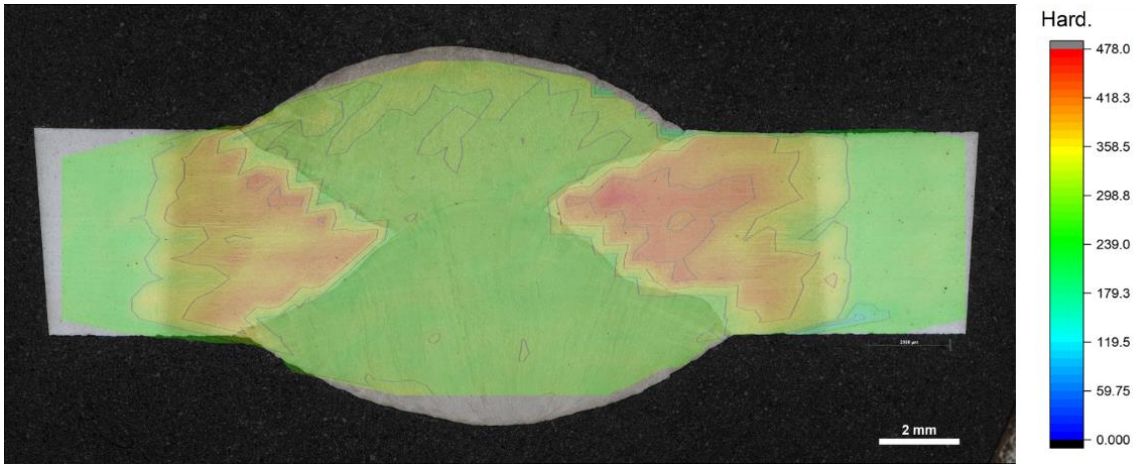

Figure 19. Composite image of light optical micrographs of the HY-100 butt joint overlaid with contour map of microhardness values in units of HV_{200}. Color scale is the same as that shown in **Figure 21** for a direct comparison of the two joint configurations.

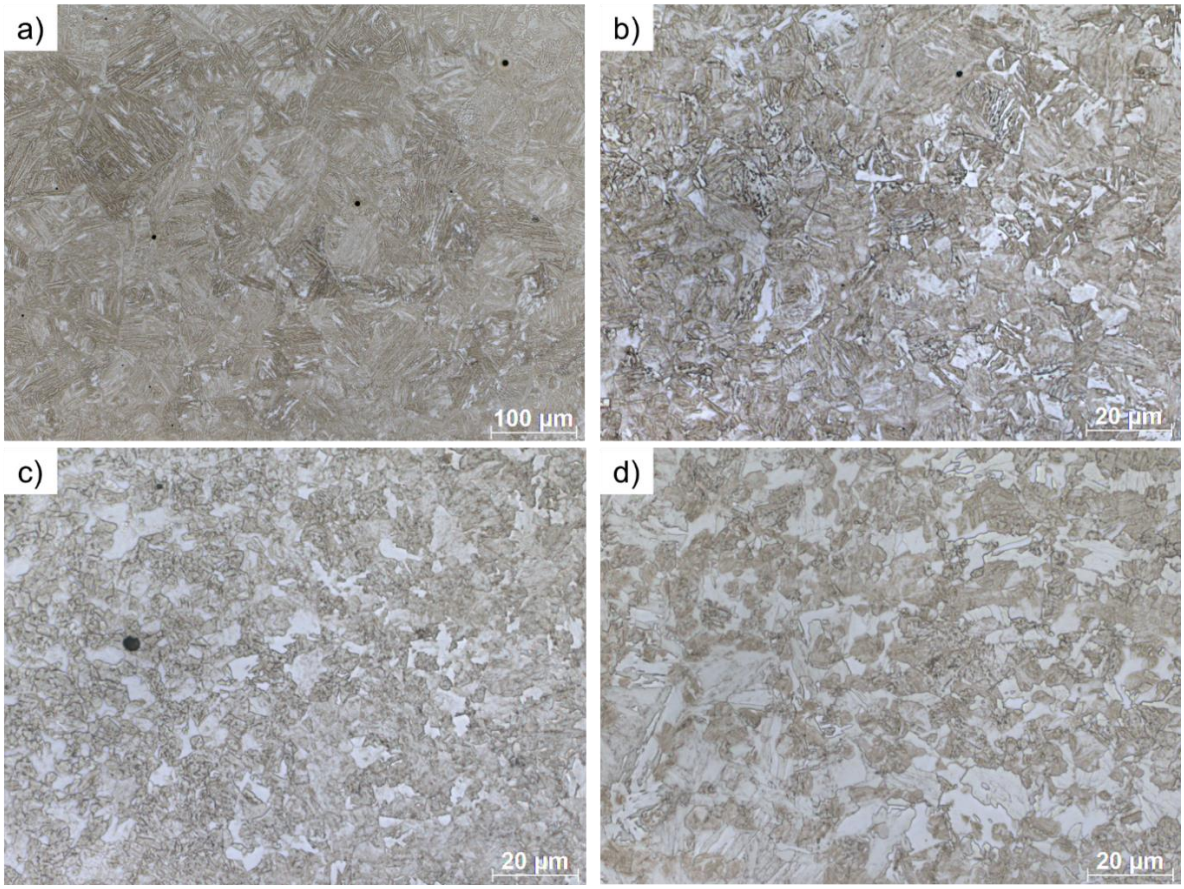

Figure 20. Representative light optical micrographs of the second pass of the HY-100 tee joint **a)** CGHAZ, **b)** FGHAZ close to the CGHAZ, **c)** FGHAZ close to the ICHAZ, and **d)** ICHAZ. Note the change in scale between images.

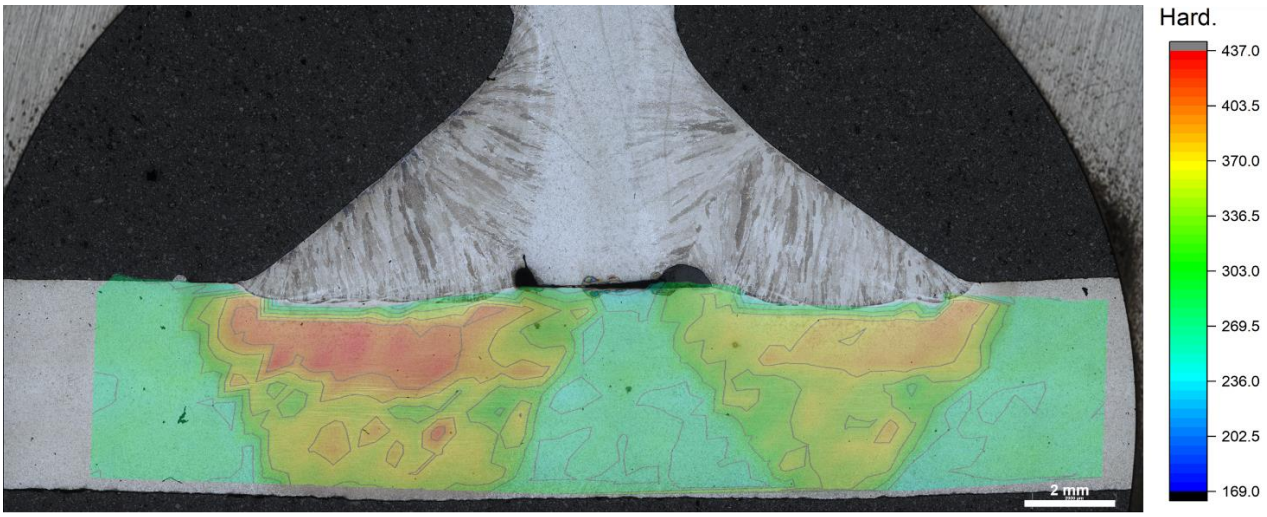

Figure 21. Composite image of light optical micrographs of the HY-100 tee joint overlaid with contour map of microhardness values in units of HV_{200}. Color scale is the same as that shown in **Figure 19** for a direct comparison of the two joint configurations.

Microhardness values measured in the butt joint matched well with those in the tee joint despite the reheated nature of HAZ regions in the butt joint. Gleeble sample microstructures generally matched

well with experimental weldment. In particular, the slowest cooling rates simulated with the Gleeble were a close match for the microstructures observed in the butt joint weldment.

Thermo-Physical Property Analysis

The average CTE values measured from the dilation curves (n=4) were $1.48 \times 10^{-5} \pm 1.71 \times 10^{-7}$ $°C^{-1}$ ($8.2 \times 10^{-6} \pm 9.5 \times 10^{-8}$ $°F^{-1}$) for the untransformed base metal below 720 °C (1328 °F) and $2.09 \times 10^{-5} \pm 1.07 \times 10^{-5}$ $°C^{-1}$ ($1.2 \times 10^{-5} \pm 1.7 \times 10^{-7}$ $°F^{-1}$) for austenite above 825 °C (1517 °F). A representative graph showing the CTE measurement is given in **Figure 22**.

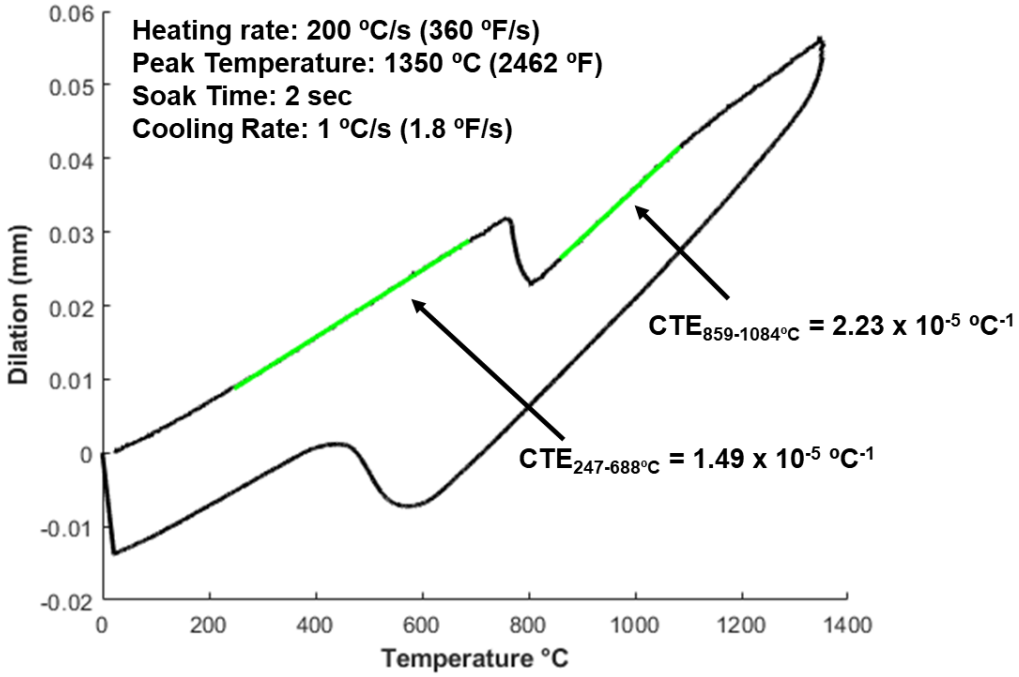

Figure 22. Representative on-heating dilatometry curve for HY-100, showing typical CTE analysis and results.

Temperature-dependent density values are shown in **Figure 23**. A comparison dataset from a Navy ManTech study conducted at the Naval Metalworking Center from the late-1990s is also included in the figure [19]. These data are labeled "CTC" for Concurrent Technologies Corporation, where the testing was conducted. Additionally, two room temperature density values from literature are shown for comparison, though one data point is 35 years old (Honeywell [20]) and the other is over 50 years old (Alloy Digest [31]). Differences are attributed to either improved measurement technique since these data were collected or modifications in mill practices relative to HY-100 composition.

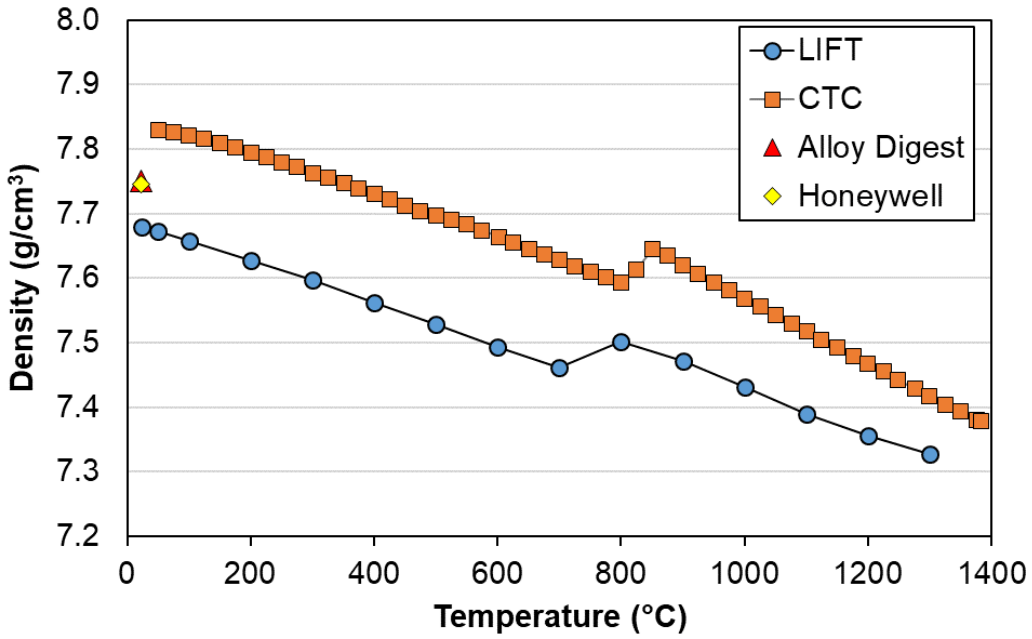

Figure 23. Density of HY-100 steel as a function of temperature. LIFT data measured using analysis of Gleeble-based dilation curves in accordance with **Equations 2** and **3**. Comparative data adapted from a CTC report [19], Honeywell report [20], and Alloy Digest book [31].

The measured specific heat and thermal diffusivity data for HY-100 can be found in **Figures 24-25**. The peaks or cusps in the data correspond to the effects of thermal energy absorption during phase transformations, particularly during the austenitic transformation between approximately 700 to 900 °C (1292 to 1652 °F). As shown, the data from this program compares well with temperature-dependent values from the CTC report [19], two specific heat values found in Alloy Digest [31], and room temperature values adapted from a Honeywell report [20].

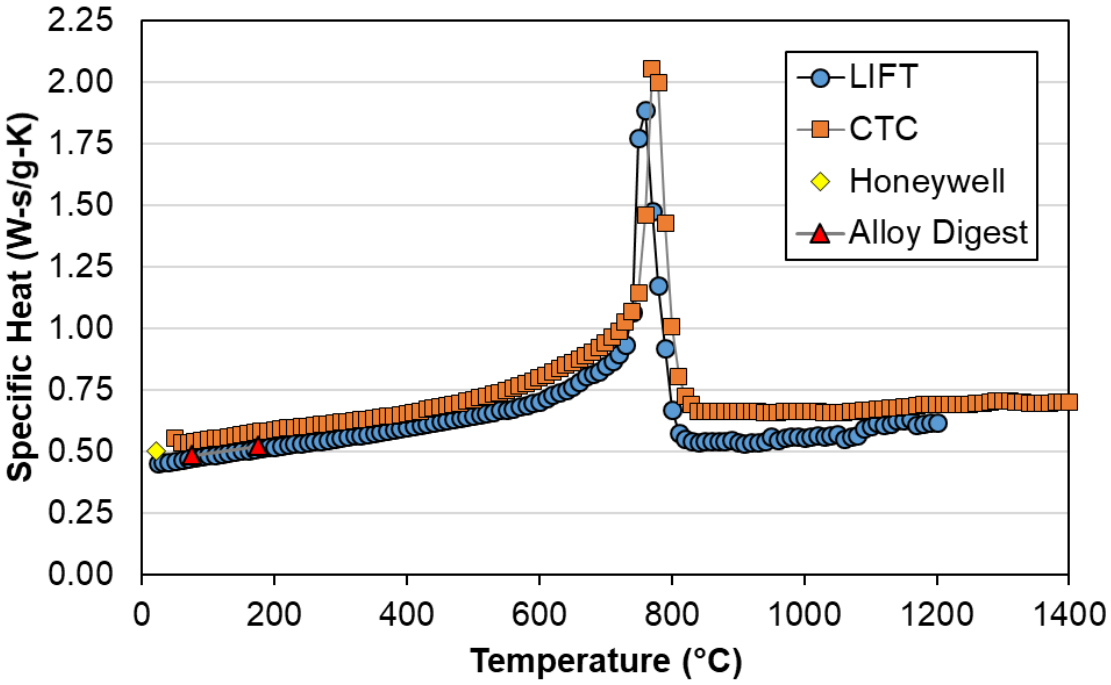

Figure 24. Measured specific heat for HY-100 steel at various temperatures. Comparative data adapted from a CTC report [19], Honeywell report [20], and Alloy Digest book [31].

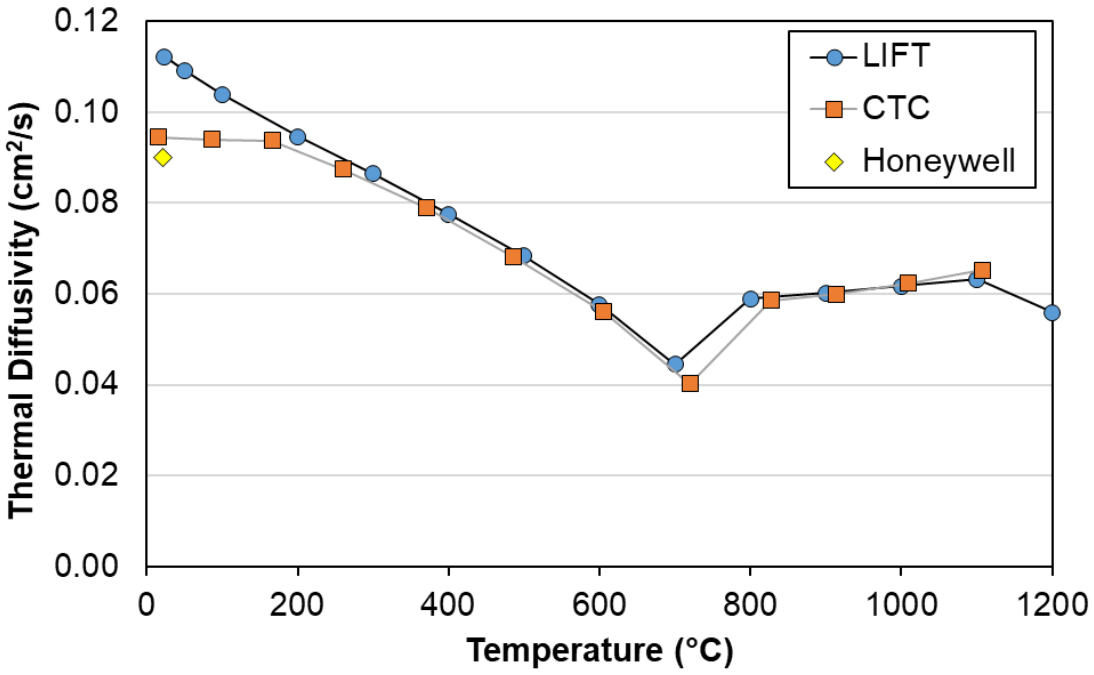

Figure 25. Measured thermal diffusivity for HY-100 steel at various temperatures. Comparative data adapted from a CTC report [19] and Honeywell report [20].

Finally, the data from **Figures 23-25** were used in conjunction with **Equation 4** to calculate the temperature-dependent thermal conductivity as shown in **Figure 26**. As shown, the data from this program compare well with temperature-dependent values from the CTC report [19], two specific heat

values found in Alloy Digest [31], and a room temperature value adapted from a Honeywell report [20]. The raw data points for all of the thermo-physical property graphs can be found in **Appendix E**.

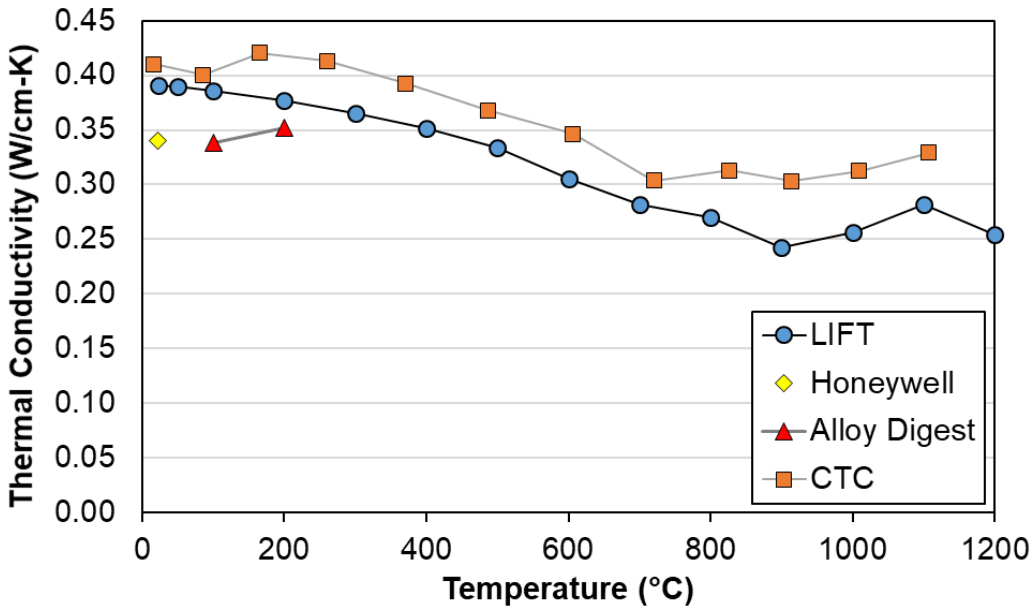

Figure 26. Calculated thermal conductivity for HY-100 steel at various temperatures. Comparative data adapted from a CTC report [19], Honeywell report [20], and Alloy Digest book [31].

Thermo-Mechanical Property Analysis

Figure 27 shows the values for elastic modulus as a function of temperature that were assumed in this work. The elevated temperature mechanical testing described above was performed in accordance with ASTM E21 [16] rather than the more appropriate ASTM E111 [32], which is prescribed when elastic modulus measurements are to be made. As such, it was determined that the experimentally measured elevated temperature elastic moduli were likely inaccurate. In order to provide elevated temperature modulus values for a HY-100 property database, the data in **Figure 27** were adapted from the European standard for fire design of steel structures [33] [34]. Of the potential sources for this information, the European standard contained the most complete data covering temperatures relevant to this study. A room temperature elastic modulus of 210 GPa (30.5 Msi) was assumed [33], as it had been previously for DH36 [5], HSLA-65 [6], HSLA-80 [7], HSLA-100 [8], and HY-80 [9] steel. It was also assumed that rigorously measured elastic moduli for HY-100 steel would be very similar to data presented in **Figure 27** because elastic properties tend to be consistent within a given material system (*e.g.*, steel). For comparison, room temperature values for elastic modulus from a Honeywell report [20] and a range of values reported from the Alloy Digest [31] are plotted as well.

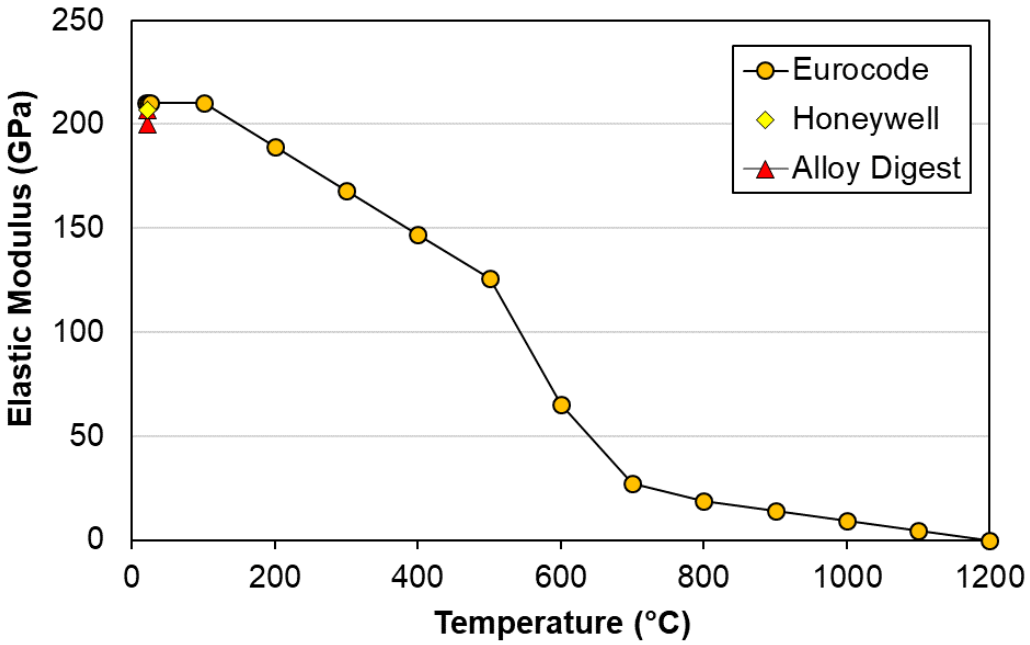

Figure 27. Assumed elevated temperature elastic modulus for HY-100 steel as adapted from references [33] [34]. Room temperature values from Honeywell adapted from reference [20] and the range of values from the Alloy Digest were adapted from reference [31].

Figure 28 shows the experimentally measured temperature-dependent 0.2% offset yield strength for HY-100 base material, and **Figure 29** shows the measured temperature-dependent ultimate tensile strength (UTS). As expected, increased temperatures result in significant strength loss. At temperatures above 800 °C (1472 °F), the base metal microstructure is completely transformed to the weaker austenite phase, resulting in relatively minor differences in strength with increasing temperature.

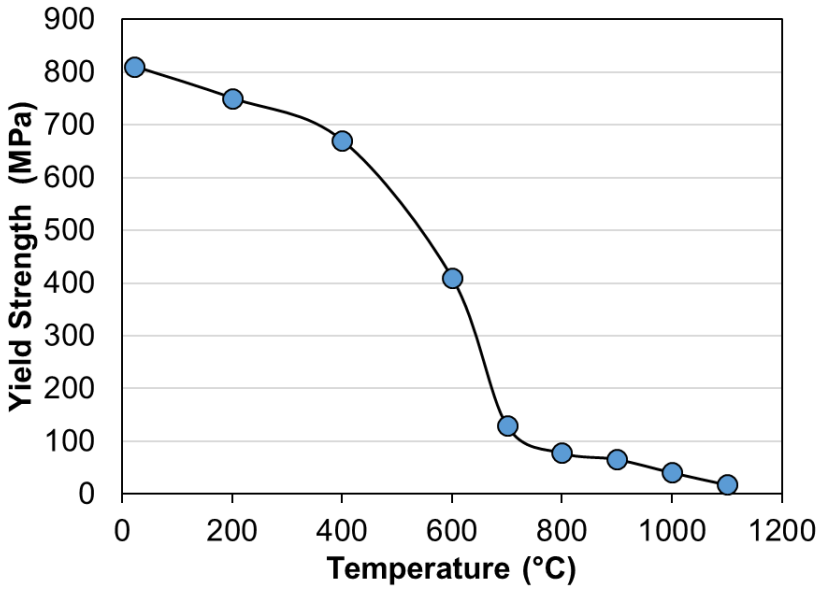

Figure 28. Measured elevated temperature 0.2% offset yield strength for HY-100 steel.

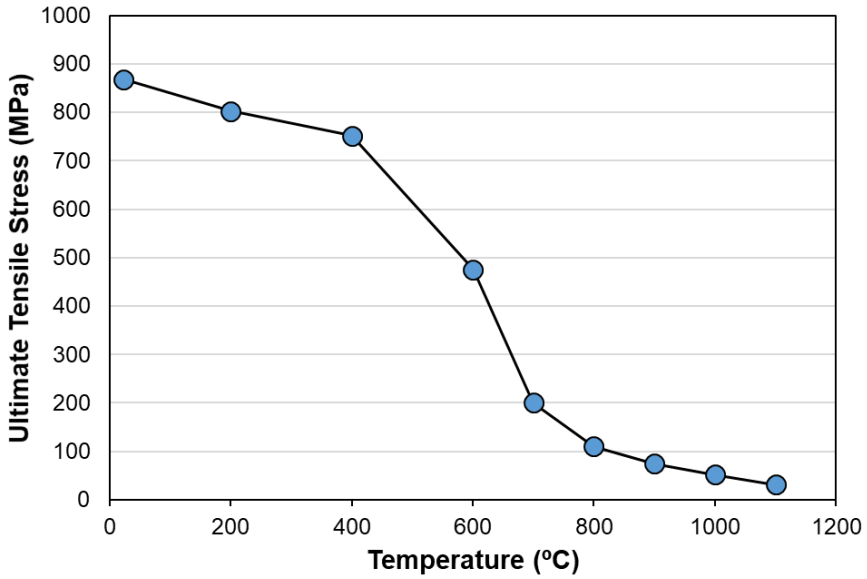

Figure 29. Measured elevated temperature ultimate tensile stress (UTS) for HY-100 steel.

Figure 30 shows the measured 0.2% offset yield strengths and **Figure 31** shows the ultimate tensile strengths of specimens cycled to a peak temperature of 1350 °C (2462 °F), along with those of the base metal on-heating for comparison. The stress-strain curves associated with the data are given in **Figure 66**-**69** of **Appendix F**. All but one sample reached the required minimum yield strength of 690 MPa (100 ksi) at room temperature. The sample cooled at 1 °C/s (1.8 °F/s) failed to meet the minimum with a yield strength of 687.9 MPa (99.8 ksi), just below the requirement. It is also the only specimen to not exceed the strength of the base material's yield strength of 810 MPa (117 ksi). Samples cooled between 10-100 °C/s (18-180 °F/s) each achieved approximately 50% higher yield strength of the sample cooled at 1 °C/s (1.8 °F/s), with an average room temperature yield strength of 1026 MPa (149 ksi). All conditions exceeded the UTS of the base material below 600 °C (1112 °F). These results are consistent with microstructural characteristics of the samples: the three rapidly cooled samples all achieved similar, entirely martensitic microstructures, while the sample cooled at 1 °C/s (1.8 °F/s) consisted of a coarse bainite. The strength also follows microhardness trends, with the low strength, slowly cooled bainitic sample measuring 275 HV_{200} and the rapidly cooled samples measuring 415, 402, and 433 HV_{200}.

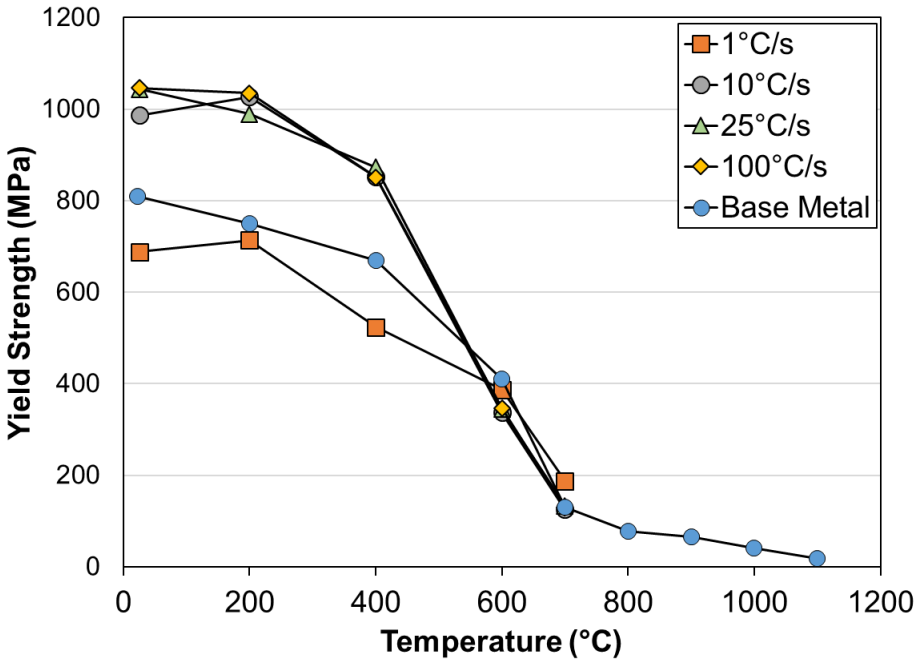

Figure 30. Yield strength of simulated HY-100 CGHAZ after heating to 1350 °C (2462 °F) and cooling at different rates as compared with base material yield strength.

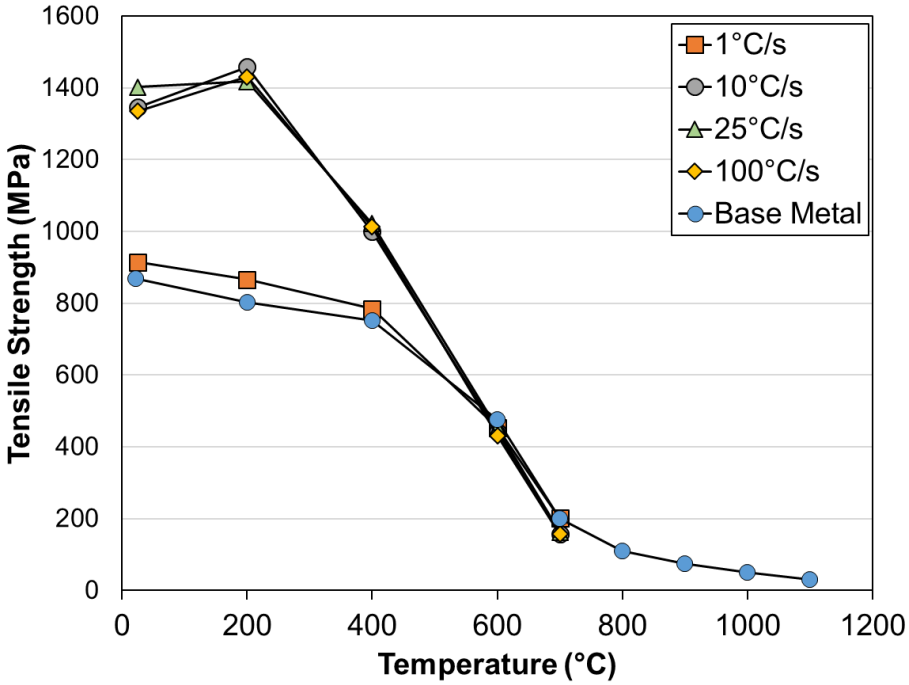

Figure 31. UTS of simulated HY-100 CGHAZ after heating to 1350 °C (2462 °F) and cooling at different rates as compared to base material UTS.

On-heating flow stress measurements for the HY-100 base material are shown in **Figure 32** for all temperatures, and **Figure 33** highlights the flow behavior for tests at temperatures of 800 °C (1472 °F)

and above. The raw data points for these graphs can be found in **Appendix F**. The data are true stresses and strains calculated by applying the traditional conversion equations to engineering stress-strain data provided by the test lab. As expected, increasing the test temperature tends to flatten the flow stress curves, since work hardening is made more difficult by dynamic recovery and/or recrystallization effects.

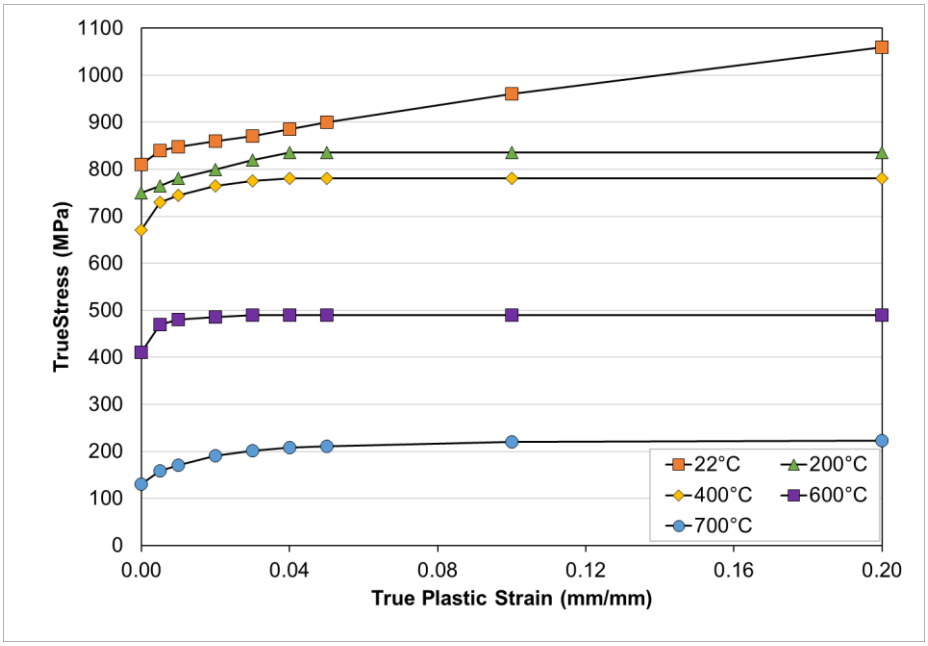

Figure 32. On-heating flow stress behavior for HY-100 steel at various temperatures.

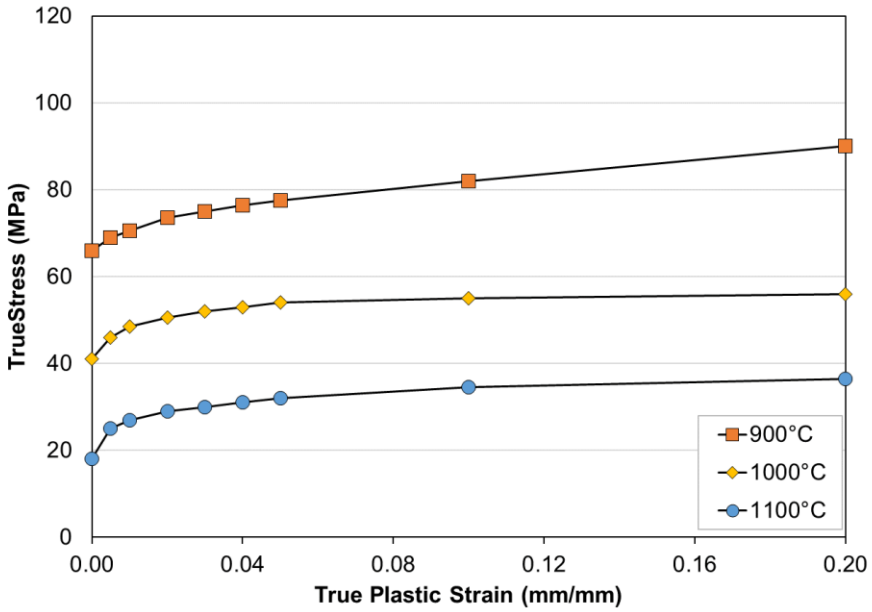

Figure 33. On-heating flow stress behavior for HY-100 steel at testing temperatures above the austenitic phase transformation.

Flow stress curves for the thermally cycled HY-100 are given in **Figures 34-37**. Once again, the data is true stresses and strains calculated by conversion from engineering stress-strain data. Such conversions are invalid past the onset of necking, so the terminal data points in **Figures 34-37** are at the

UTS. All raw data points for these figures, along with the engineering fracture strains for the specimens, are found in **Appendix F**.

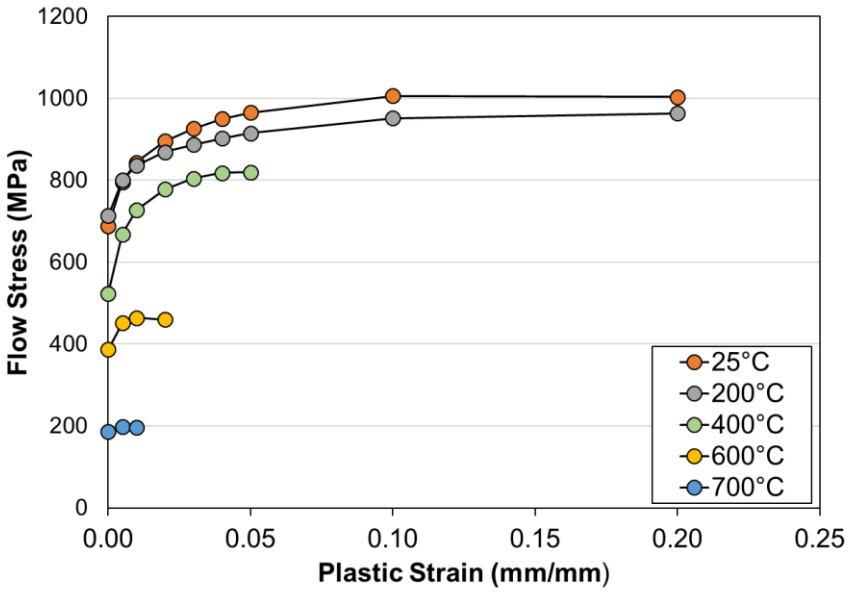

Figure 34. Flow stress behavior at various temperatures for HY-100 steel after cooling at 1 °C/s (1.8 °F/s) from a peak temperature of 1350 °C (2462 °F). Terminal data points are the true stress at fracture.

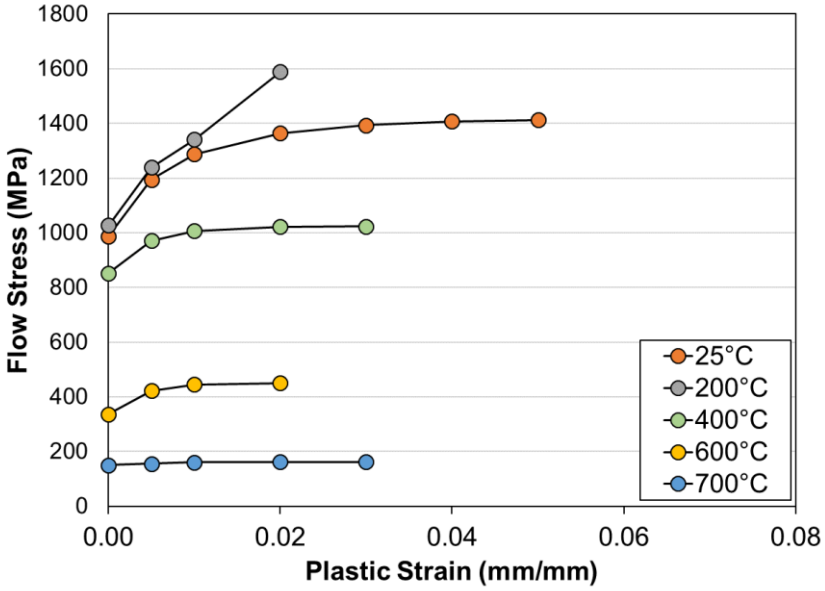

Figure 35. Flow stress behavior at various temperatures for HY-100 steel after cooling at 10 °C/s (18 °F/s) from a peak temperature of 1350 °C (2462 °F). Terminal data points are the true stress at fracture.

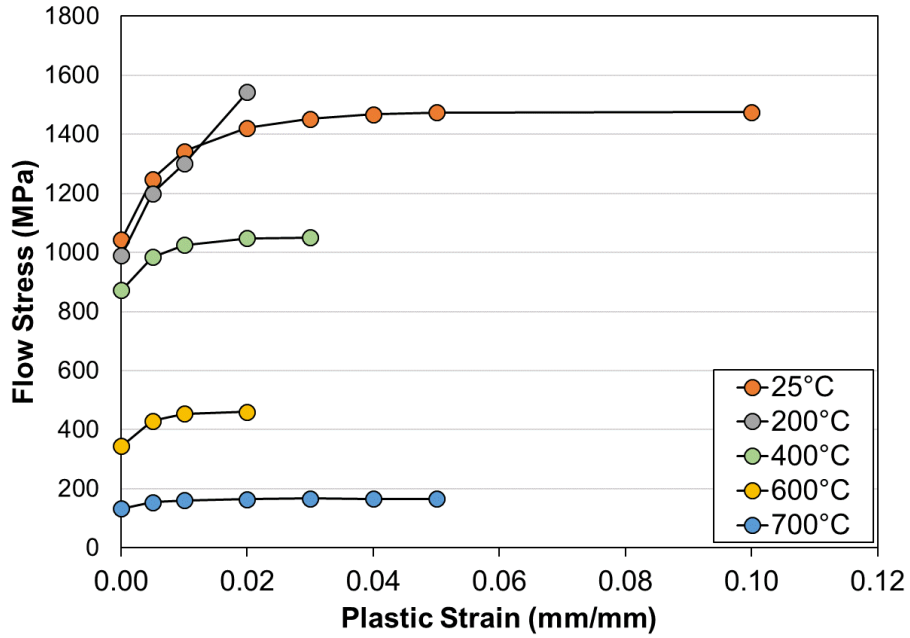

Figure 36. Flow stress behavior at various temperatures for HY-100 steel after cooling at 25 °C/s (45 °F/s) from a peak temperature of 1350 °C (2462 °F). Terminal data points are the true stress at fracture.

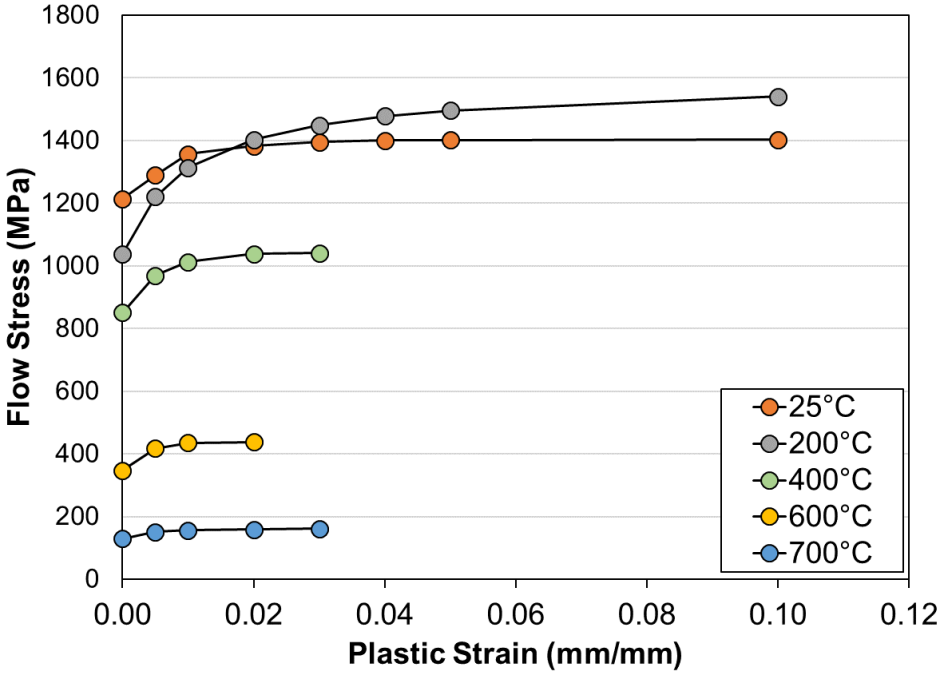

Figure 37. Flow stress behavior at various temperatures for HY-100 steel after cooling at 100 °C/s (180 °F/s) from a peak temperature of 1350 °C (2462 °F). Terminal data points are the true stress at fracture.

CONCLUSIONS

Temperature-dependent material property data of a pedigreed plate of HY-100 steel from room temperature up to nearly the steel's melting point were determined. The thermo-physical properties investigated include specific heat, thermal diffusivity, thermal conductivity, CTE, and density. Thermo-mechanical properties including yield strength, UTS, and flow stress were also measured. The temperatures associated with on-heating and on-cooling phase transformations and their variation with heating rate, cooling rate, and peak temperature were determined and used to develop welding-focused CCT diagrams. Investigation of HAZ microstructures from the CCT specimens and arc welds concluded the analysis. This effort is essential for increasing the fidelity of finite element models used to predict welding-induced distortion and residual stress in marine structures. The data generated in this program have been provided to ESI for immediate incorporation into their *SYSWELD* software. A machine-readable version of the collected data will be uploaded to the University of Michigan's *Materials Commons* data repository <https://materialscommons.org> at a later date.

APPENDIX

Appendix A: Plate Conformance Certificate and Chemical Composition for HY-100

4 C 0 4 5 3

T E S T C E R T I F I C A T

ARCELORMITTAL PLATE LLC

PAGE NO: 01 OF 02
FILE NO: 2822-01-02
MILL ORDER NO: 94761-001
MELT NO: C5106
SLAB NO: 1AK
DATE: 11/15/12

SHIP TO:
RONSON TECHNICAL PRODUCTS
C/O HUDSON METAL PROCESSING
1500 NATIONAL CEMETARY ROAD
FLORENCE SC 29506

ORIGINAL

SOLD TO:
ENERGY & PROCESS CORPORATION
A FERGUSON ENTERPRISE
P.O. BOX 125
TUCKER GA 30085-0125

SEND TO:
ENERGY & PROCESS CORPORATION
A FERGUSON ENTERPRISE
POWER GENERATION SERVICES DIV.
2146-B FLINSTONE DRIVE
TUCKER, GA 30084

01-C

P L A T E D I M E N S I O N S / D E S C R I P T I O N

TOTAL QTY	GAUGE	WIDTH	LENGTH	DESCRIPTION	PIECE WEIGHT
1	3/16"	96"	240"	RECTANGLE	1225#

C U S T O M E R I N F O R M A T I O N

CUSTOMER PO: J257-43

PART NO. HY100316N

S P E C I F I C A T I O N (S)

THIS MATERIAL HAS BEEN MANUFACTURED AND TESTED IN ACCORDANCE WITH PURCHASE ORDER REQUIREMENTS AND SPECIFICATION(S).

NAVSE TECH-PUB-T9074 REV 0 YR 02 HY100-TY.I
MIL S-16216K HY100 TYPE I
NAVSEA TECH. PUBLICATIOIN T9074-BD-GIB-010/0300
REVISION 0 DATED 08/09/02 HY100-TYI
WITH ACN 1 OF 11 DEC. 2002
THE MANAGEMENT SYSTEMS FOR MANUFACTURE OF THIS PRODUCT ARE CERTIFIED TO ISO 9001:2008 (CERTIFICATE NO. 30130) AND ISO 14001 (CERTIFICATE NO. 009496).

C H E M I C A L C O M P O S I T I O N

	C	MN	P	S	CU	SI	NI	CR	MO
MELT:C5106	.16	.30	.007	.002	.15	.21	2.43	1.25	.26
PROD ANALYSIS	.15	.30	.007	.002	.15	.21	2.44	1.24	.25

	V	TI	AL	CB	SB	AS	SN
MELT:C5106	.004	.001	.014	.001	.0010	.0030	.007
PROD ANALYSIS	.004	.001	.013	.001	.0010	.0030	.007

M A N U F A C T U R E

ELECTRIC FURNACE QUALITY - FINELINE - VACUUM DEGASSED - FINE GRAIN PRACTICE

PA2250386

H E A T T R E A T C O N D I T I O N

MATL OR TEST	HEAT TREAT DESCRIPTION	NOM TEMP	HOLD MINS	COOL MTHD
PL/TEST	HARDEN	1660F	14	W.QUENCH
PL/TEST	TEMPER	1180F	26	AIR COOL

WE HEREBY CERTIFY THE ABOVE INFORMATION IS CORRECT:

ARCELORMITTAL PLATE LLC
QUALITY ASSURANCE LABORATORY
139 MODENA ROAD
COATESVILLE, PA 19320

ABS PHILADELPHIA

Q.A. APPROVED
RONSON TECHNICAL PRODUCTS
0801

Elinore Zaplitny

SUPERVISOR - TEST REPORTING
ELINORE ZAPLITNY

4 0 0 4 5 3

T E S T C E R T I F I C A T

PAGE NO: 02 OF 02
FILE NO: 2822-01-02
MILL ORDER NO: 94761-001
MELT NO: C5106
SLAB NO: 1AK
DATE: 11/15/12

T E N S I L E P R O P E R T I E S

SLAB NO.	LOC	DIR	YIELD STRENGTH PSI X 100	TENSILE STRENGTH PSI X 100	ELONGATION GAGE LGTH	%
1AK	BOT.	TRANS.	1088	1195	2.00"	18.0
1AK	TOP	TRANS.	1096	1206	2.00"	16.0

G E N E R A L I N F O R M A T I O N

ALL STEEL HAS BEEN MELTED AND MANUFACTURED IN THE U.S.A.
PRODUCED IN ACCORDANCE WITH INSPECTION SYSTEM
REQUIREMENTS OF MIL-I-45208A AMEND #1.
A.B.S. Q.A. CERTIFICATE 10-MMPQA-586.
MATERIAL HAS BEEN VACUUM DEGASSED AND CALCIUM TREATED
FOR SULFIDE SHAPE CONTROL.
FINELINE MOD FOR SULPHUR
THE TEST RESULTS SHOWN IN THIS REPORT ARE THE
RESULTS OF TESTING PERFORMED BY OUR ORGANIZATION.
LOW MELTING ALLOYS OR LOW MELTING COMPOUNDS ARE NOT
USED IN THE MANUFACTURE OF ARCELORMITTAL PLATE LLC
PRODUCTS OTHER THAN AS DEOXIDIZING AGENTS.
NO WELD REPAIR PERFORMED BY ARCELORMITTAL PLATE LLC.
ACID SOLUBLE ALUMINUM
FOR MORE INFORMATION AND PROCESSING GUIDELINES, REFER TO
WWW.ARCELORMITTAL.COM/PLATEINFORMATION

NDT, VISUAL AND DIMENSIONAL INSPECTION AS REQUIRED BY THE SPECIFICATION WAS SATISFACTORILY PERFORMED.

MATERIAL HAS BEEN SAMPLED, TESTED, AND INSPECTED IN ACCORDANCE WITH THE SPECIFICATION REQUIREMENTS. THE MANUFACTURER HAS MAINTAINED MANUFACTURING PROCEDURES AND PRACTICES WHICH PRODUCE PLATES WHICH MEET THE MINIMUM PROPERTY REQUIREMENTS THROUGHOUT THE PLATE. THE MATERIAL MEETS ALL SPECIFICATION REQUIREMENTS.

RECORDS ARE AVAILABLE COVERING HEAT NUMBER OF THE MATERIAL USED, PROCESSING OF PLATE, DIMENSIONAL CONTROL EMPLOYED AND HEAT TREATMENT.

MERCURY OR MERCURY COMPOUNDS ARE NOT USED IN THE MANUFACTURE OF ARCELORMITTAL PLATE LLC PRODUCTS.

KNOWINGLY AND WILLFULLY FALSIFYING OR CONCEALING A MATERIAL FACT ON THIS FORM, OR MAKING FALSE, FICTITIOUS OR FRAUDULENT ENTRIES OR REPRESENTATIONS HEREIN, COULD CONSTITUTE A FELONY PUNISHABLE UNDER FEDERAL STATUTES.

CERTIFICATE OF CONFORMANCE - ALL ITEMS FURNISHED IN THE SHIPMENT ARE IN FULL CONFORMANCE WITH ALL P.O. AND SPEC. REQ.; AND THAT THE T.R.'S REPRESENT THE ACTUAL ATTRIBUTES OF THE ITEMS FURNISHED ON THE ORDER, AND THAT THE TEST RESULTS ARE IN FULL CONFORMANCE WITH ALL P.O. & SPEC. REQ. RECORDS TO SUBSTANTIATE THE ABOVE ARE ON FILE IN

OUR PLANT AND WILL BE MAINTAINED FOR A PERIOD OF 7 YRS. FROM THE DATE OF THE SHIPMENT UNLESS FURNISHED TO THE PURCHASER IN ADVANCE OF OR AT TIME OF SHIPMENT. WHEN RECORDS ARE RETAINED BY US, WE AGREE TO FURNISH SAME TO THE PURCHASER AT ANY TIME DURING THE ABOVE PERIOD UPON REQUEST.

HEAT TREAT PROC. NO. MIL-STD-1684D

B/L #08007 JONES MOTOR CO.

WE HEREBY CERTIFY THE ABOVE INFORMATION IS CORRECT:

ARCELORMITTAL PLATE LLC
QUALITY ASSURANCE LABORATORY
139 MODENA ROAD
COATESVILLE, PA 19320

Elinore Zaplitny

SUPERVISOR - TEST REPORTING
ELINORE ZAPLITNY

Table 8. Chemical Composition of HY-100 Base Plate as Measured by NSWCCD

Element	Wt	Test 1	Test 2	Test 3	Test 4	Average
C	%	0.166	0.164	0.165	0.166	0.1652
Si	%	0.235	0.233	0.233	0.233	0.2335
Mn	%	0.325	0.314	0.322	0.322	0.321
P	%	0.00702	0.0066	0.00674	0.00684	0.0068
S	%	0.00415	0.00410	0.00414	0.00410	0.00412
Cr	%	1.7	1.44	1.56	1.58	1.57
Mo	%	0.247	0.248	0.25	0.25	0.321
Ni	%	2.59	2.59	2.6	2.62	2.6
Al	%	0.0193	0.0192	0.0194	0.0194	0.0193
Co	%	0.0082	0.0073	0.0062	0.0061	0.0070
Cu	%	0.158	0.154	0.155	0.156	0.156
Nb	%	<0.003	<0.003	<0.003	<0.003	<0.003
Ti	%	<0.001	<0.001	<0.001	<0.001	<0.001
V	%	<0.003	<0.003	<0.003	<0.003	<0.003
Sn	%	<0.005	<0.005	<0.005	<0.005	<0.005
Zr	%	<0.01	<0.01	<0.01	<0.01	<0.01
Ca	%	0.0012	0.0014	0.0015	0.0013	0.0013
Ta	%	0.117	0.115	0.108	0.103	0.111
B	%	<0.0004	<0.0004	<0.0004	<0.0004	<0.0004

Table 9. Chemical Composition of HY-100 Base Plate as Measured by OSU

Element	Wt	Test 1	Test 2	Test 3	Average
C	%	0.076	0.068	0.071	0.072
Si	%	0.22	0.22	0.22	0.22
Mn	%	0.29	0.29	0.29	0.29
P	%	0.005	0.005	0.004	0.005
S	%	0.0006	0.0007	0.0009	0.0007
Cr	%	1.25	1.25	1.25	1.25
Mo	%	0.26	0.27	0.26	0.26
Ni	%	2.91	2.94	2.90	2.92
Al	%	0.019	0.017	0.018	0.018
Co	%	0.003	0.003	0.003	0.003
Cu	%	0.15	0.15	0.15	0.15
Nb	%	0.002	0.001	0.002	0.002
Ti	%	0.002	0.002	0.002	0.002
V	%	0.005	0.005	0.005	0.005
W	%	<0.005	<0.005	<0.005	<0.005
Pb	%	<0.0010	0.001	<0.0010	<0.0010
Sn	%	0.009	0.009	0.009	0.009
As	%	0.008	0.008	0.007	0.008
Zr	%	<0.0010	<0.0010	<0.0010	<0.0010
Ca	%	0.002	0.001	0.002	0.002
Ce	%	<0.0010	<0.0010	<0.0010	<0.0010
Sb	%	0.007	0.005	0.006	0.006
Se	%	0.003	<0.002	0.003	0.002
Te	%	0.014	0.013	0.014	0.014
Ta	%	<0.007	<0.007	<0.007	<0.007
B	%	0.001	0.001	0.001	0.001
Zn	%	0.002	0.003	0.002	0.003
La	%	0.0003	0.0006	0.0005	0.0005

Appendix B: Continuous Cooling Transformation Curves

Table 10. Austenite Transformation Temperatures as Illustrated in **Figure 8**.

Heating Rate (°C/s)	A_{c1} (°C)	A_{c3} (°C)
10	745.6	810.1
100	770.9	851.7
200	729.5	780.8
500	758.2	788.0
1000	772.5	808.3
2000	760.7	789.7

Table 11. Experimentally Measured On-Cooling Transformation Temperatures for HY-100 Dilatometry Specimens Cooled from 785 °C (1445 °F). Note: Colors correspond to the transformation products discussed in **Figures 9-15**.

Cooling Rate (°C/s) [°F/s]	1 [1.8]	5 [9]	10 [18]	25 [45]	100 [180]	200 [360]
Transformation Temperature (°C) [°F]	712 [1313]	693 [1279]	722 [1332]	511 [952]	404 [759]	408 [766]
	630 [1166]	630 [1166]	656 [1213]	402 [756]	254 [489]	241 [466]
	516 [961]	550 [1022]	553 [1027]	267 [513]		
	347 [657]	390 [734]	399 [750]			
	256 [493]	254 [489]	243 [469]			

Table 12. Experimentally Measured On-Cooling Transformation Temperatures for HY-100 Dilatometry Specimens Cooled from 1000 °C (1832 °F). Note: Colors correspond to the transformation products discussed in **Figures 9-15**.

Cooling Rate (°C/s) [°F/s]	1 [1.8]	5 [9]	10 [18]	25 [45]	100 [180]	200 [360]
Transformation Temperature (°C) [°F]	566 [1051]	488 [910]	454 [849]	412 [774]	389 [732]	400 [752]
	413 [775]	389 [732]	417 [783]	257 [495]	251 [484]	262 [504]
	325 [617]	279 [534]	262 [504]			

Table 13. Experimentally Measured On-Cooling Transformation Temperatures for HY-100 Dilatometry Specimens Cooled from 1150 °C (2102 °F). Note: Colors correspond to the transformation products discussed in **Figures 9-15**.

Cooling Rate (°C/s) [°F/s]	1 [1.8]	5 [9]	10 [18]	25 [45]	100 [180]	200 [360]
Transformation Temperature (°C) [°F]	583 [1081]	544 [1011]	416 [781]	432 [810]	431 [808]	418 [784]
	402 [756]	481 [898]	271 [520]	259 [498]	269 [516]	266 [511]
		271 [520]				

Table 14. Experimentally Measured On-Cooling Transformation Temperatures for HY-100 Dilatometry Specimens Cooled from 1350 °C (2462 °F). Note: Colors correspond to the transformation products discussed in **Figures 9-15**.

Cooling Rate (°C/s) [°F/s]	1 [1.8]	5 [9]	10 [18]	25 [45]	100 [180]	200 [360]
Transformation Temperature (°C) [°F]	614 [1137]	503 [937]	502 [936]	445 [833]	431 [808]	431 [808]
	452 [846]	428 [802]	433 [811]	271 [520]	269 [516]	270 [518]
	370- [698]	268 [514]	272 [522]			

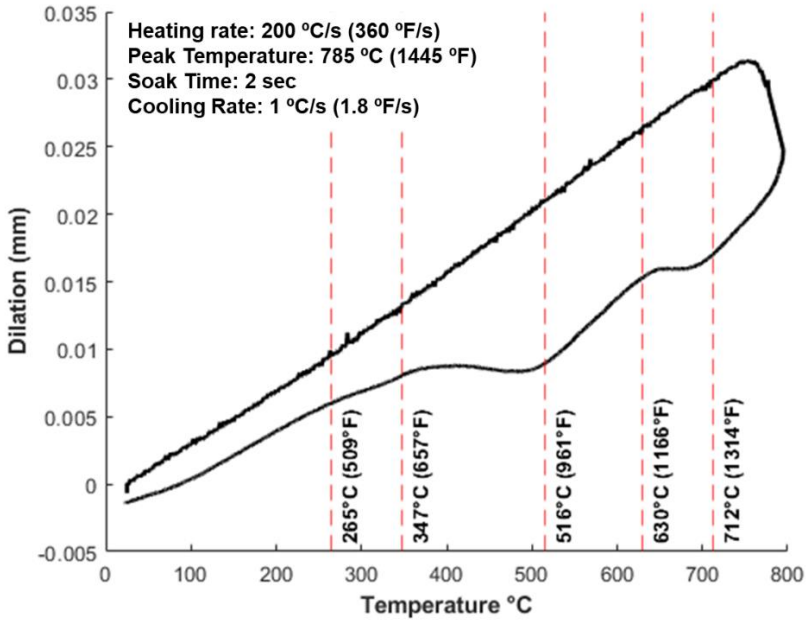

Figure 38. Dilation curve from a HY-100 Gleeble sample heated to a peak temperature of 785 °C and cooled at 1 °C/s.

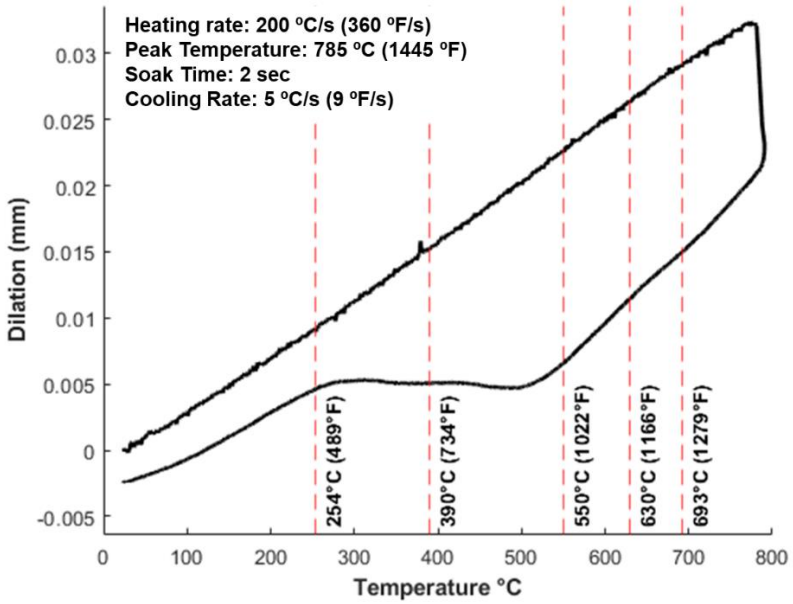

Figure 39. Dilation curve from a HY-100 Gleeble sample heated to a peak temperature of 785 °C and cooled at 5 °C/s.

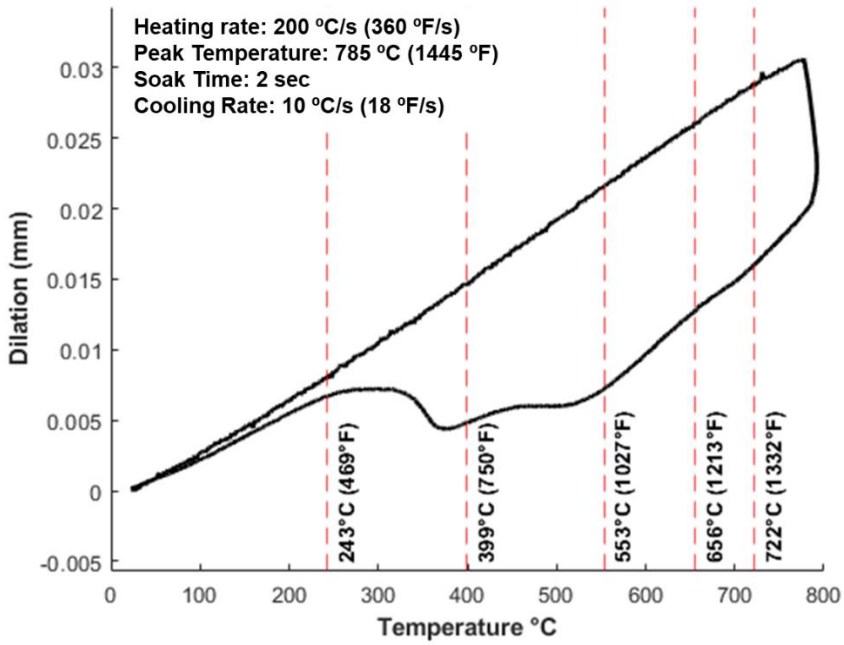

Figure 40. Dilation curve from a HY-100 Gleeble sample heated to a peak temperature of 785 °C and cooled at 10 °C/s.

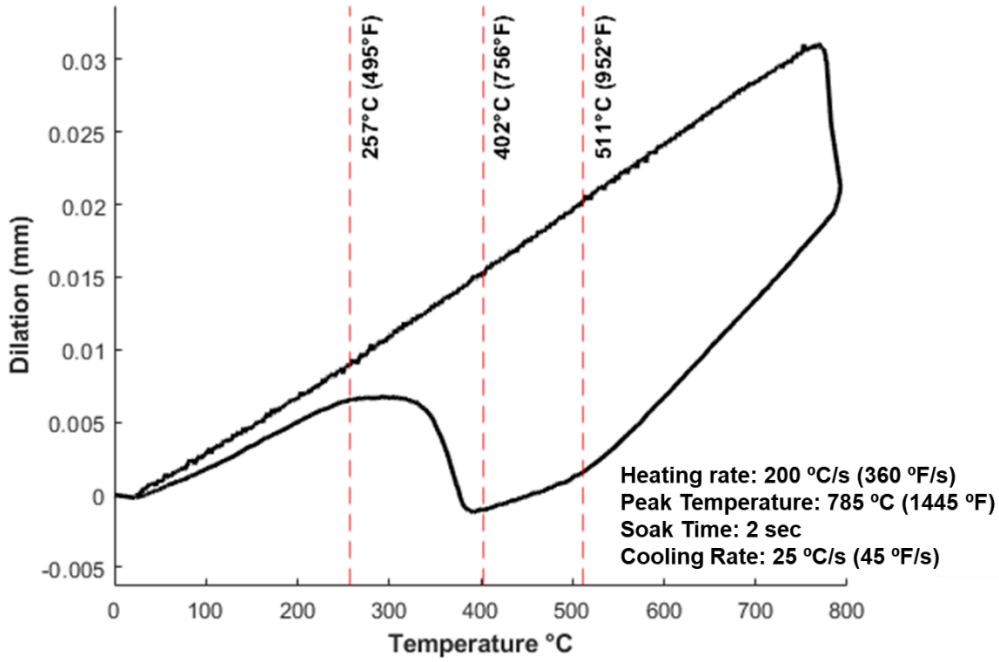

Figure 41. Dilation curve from a HY-100 Gleeble sample heated to a peak temperature of 785 °C and cooled at 25 °C/s.

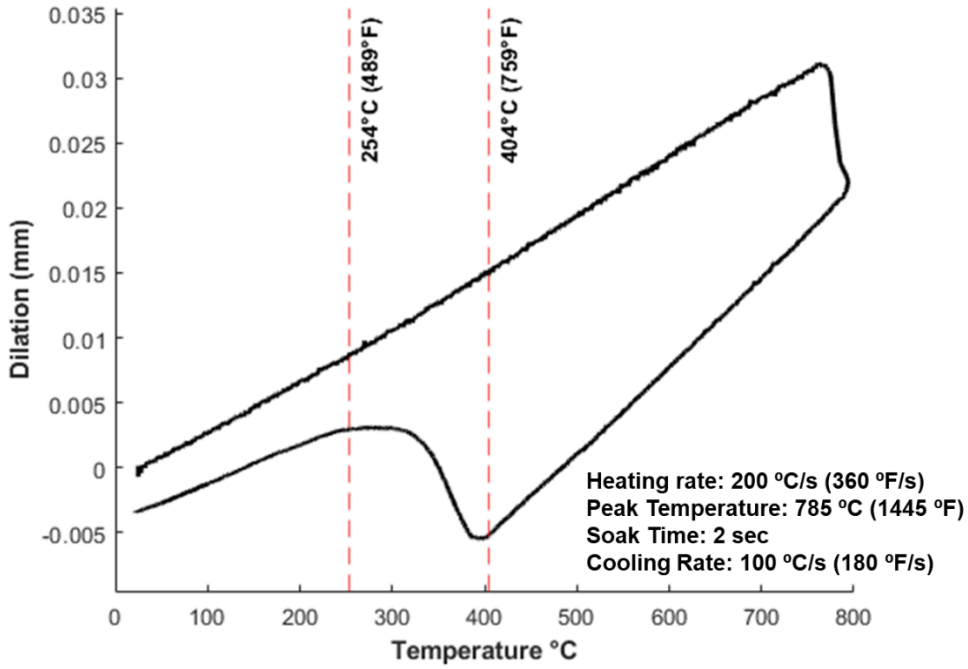

Figure 42. Dilation curve from a HY-100 Gleeble sample heated to a peak temperature of 785 °C and cooled at 100 °C/s.

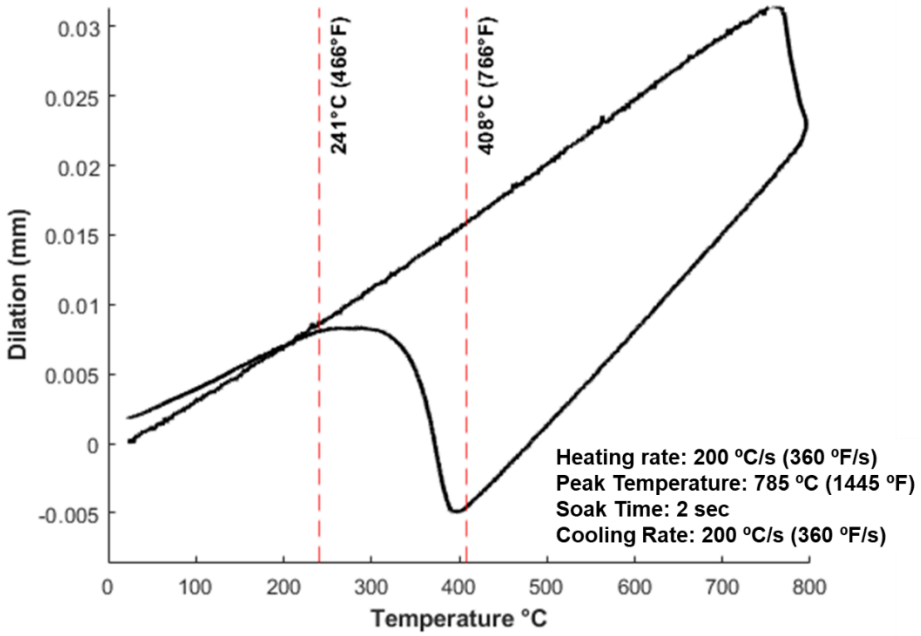

Figure 43. Dilation curve from a HY-100 Gleeble sample heated to a peak temperature of 785 °C and cooled at 200 °C/s.

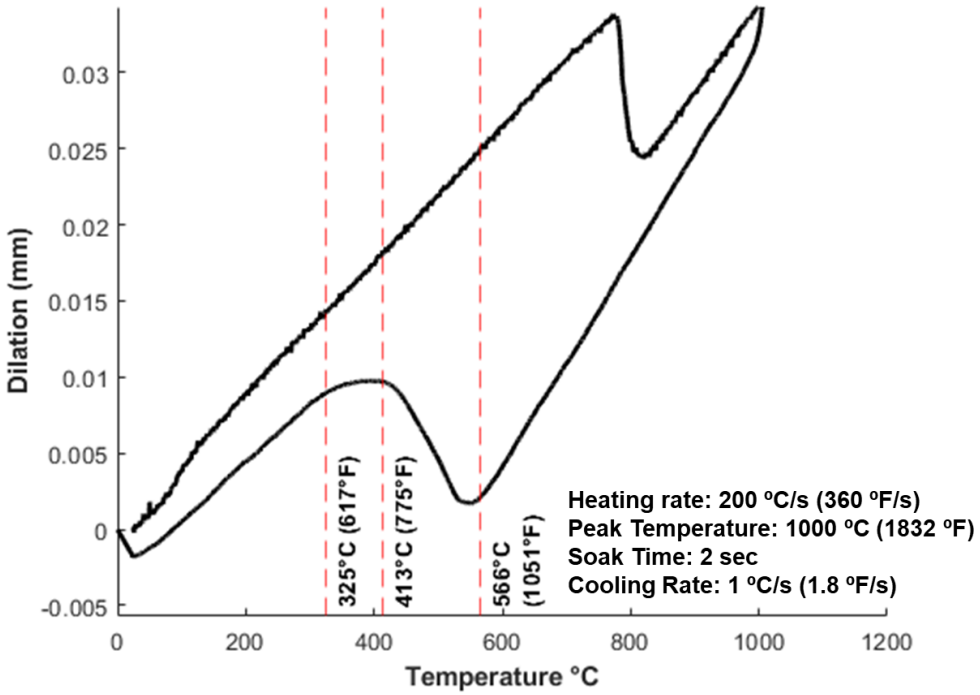

Figure 44. Dilation curve from a HY-100 Gleeble sample heated to a peak temperature of 1000 °C and cooled at 1 °C/s.

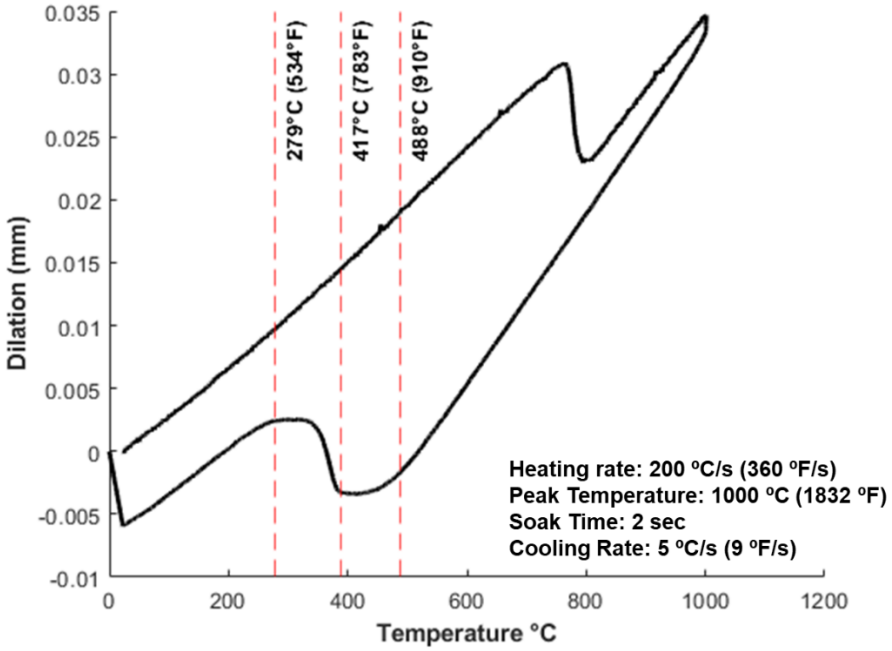

Figure 45. Dilation curve from a HY-100 Gleeble sample heated to a peak temperature of 1000 °C and cooled at 5 °C/s.

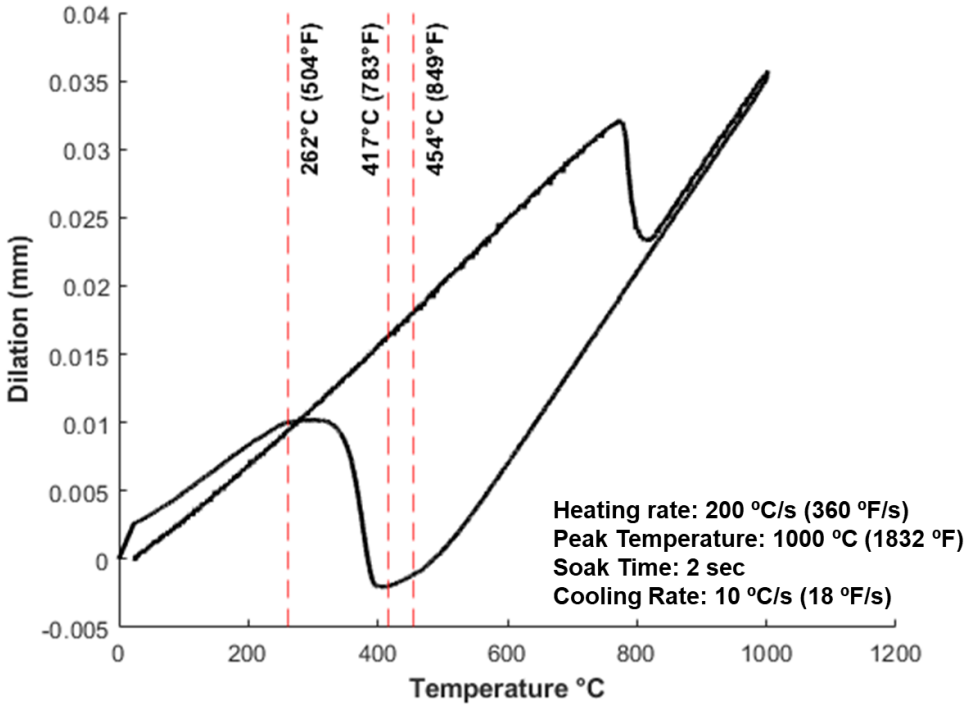

Figure 46. Dilation curve from HY-100 Gleeble sample heated to a peak temperature of 1000 °C and cooled at 10 °C/s.

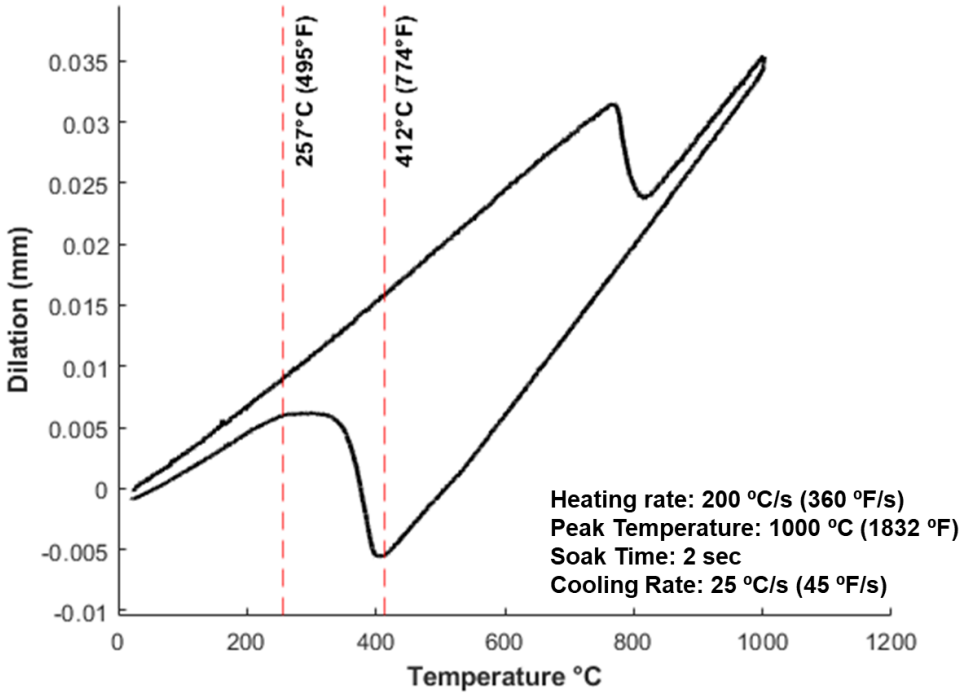

Figure 47. Dilation curve from a HY-100 Gleeble sample heated to a peak temperature of 1000 °C and cooled at 25 °C/s.

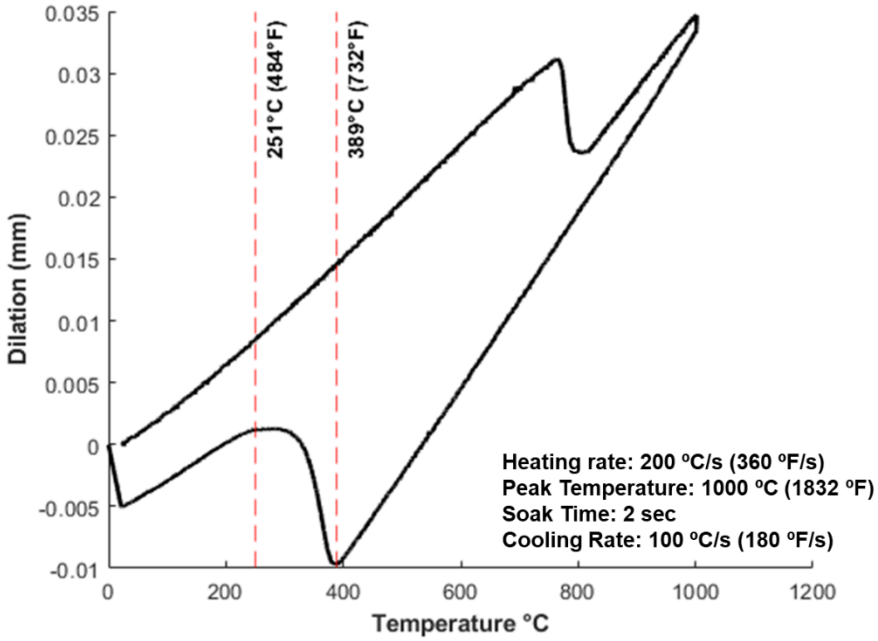

Figure 48. Dilation curve from a HY-100 Gleeble sample heated to a peak temperature of 1000 °C and cooled at 100 °C/s.

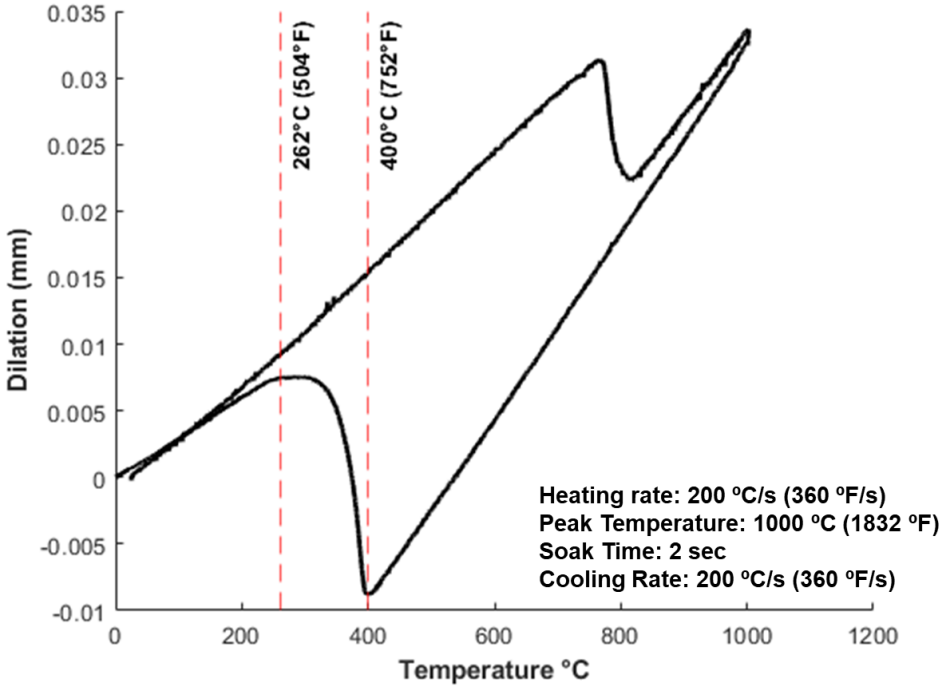

Figure 49. Dilation curve from a HY-100 Gleeble sample heated to a peak temperature of 1000 °C and cooled at 200 °C/s.

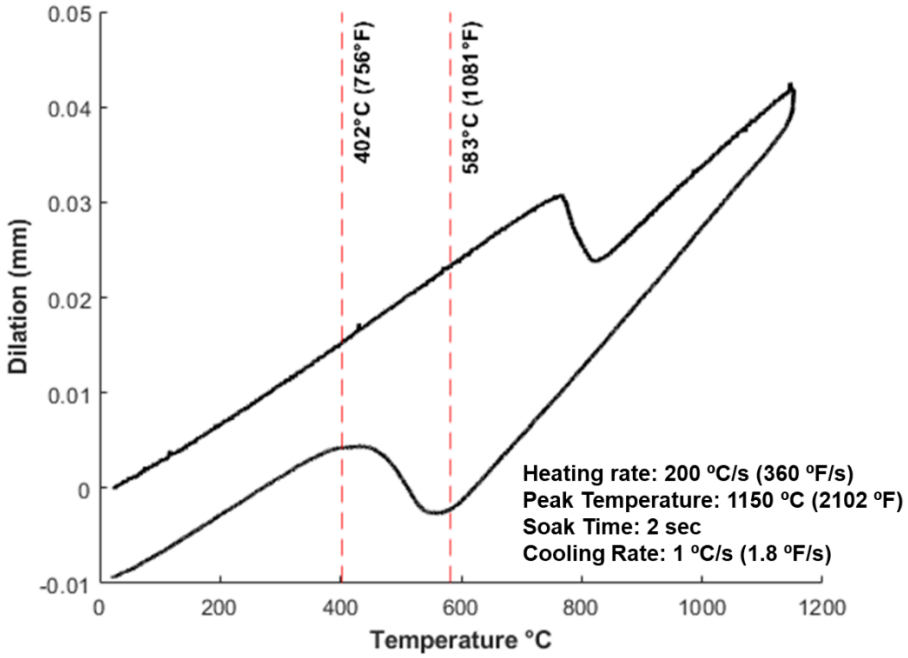

Figure 50. Dilation curve from a HY-100 Gleeble sample heated to a peak temperature of 1150 °C and cooled at 1 °C/s.

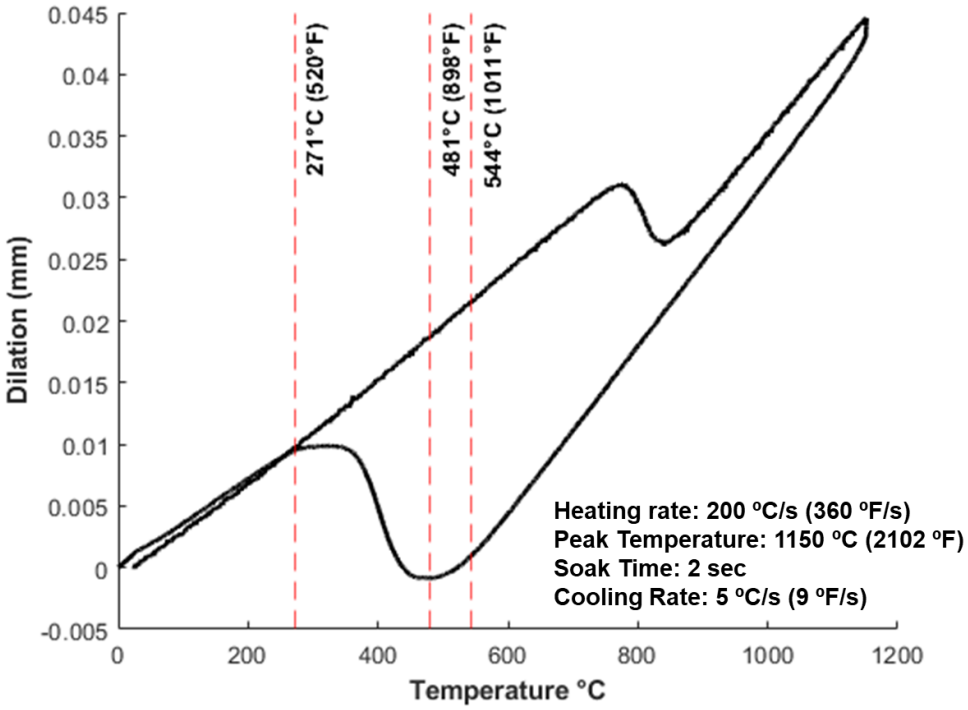

Figure 51. Dilation curve from a HY-100 Gleeble sample heated to a peak temperature of 1150 °C and cooled at 5 °C/s.

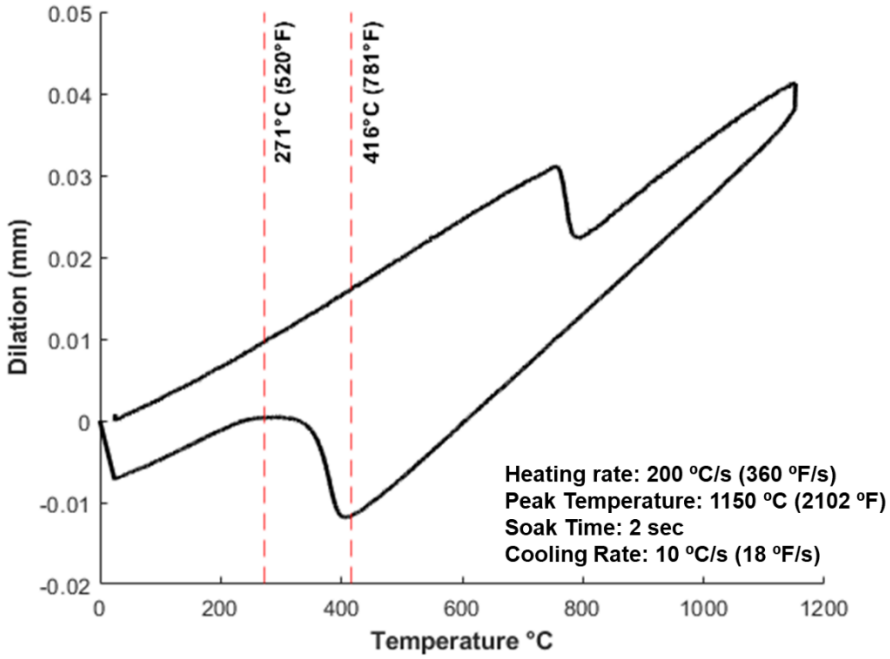

Figure 52. Dilation curve from a HY-100 Gleeble sample heated to a peak temperature of 1150 °C and cooled at 10 °C/s.

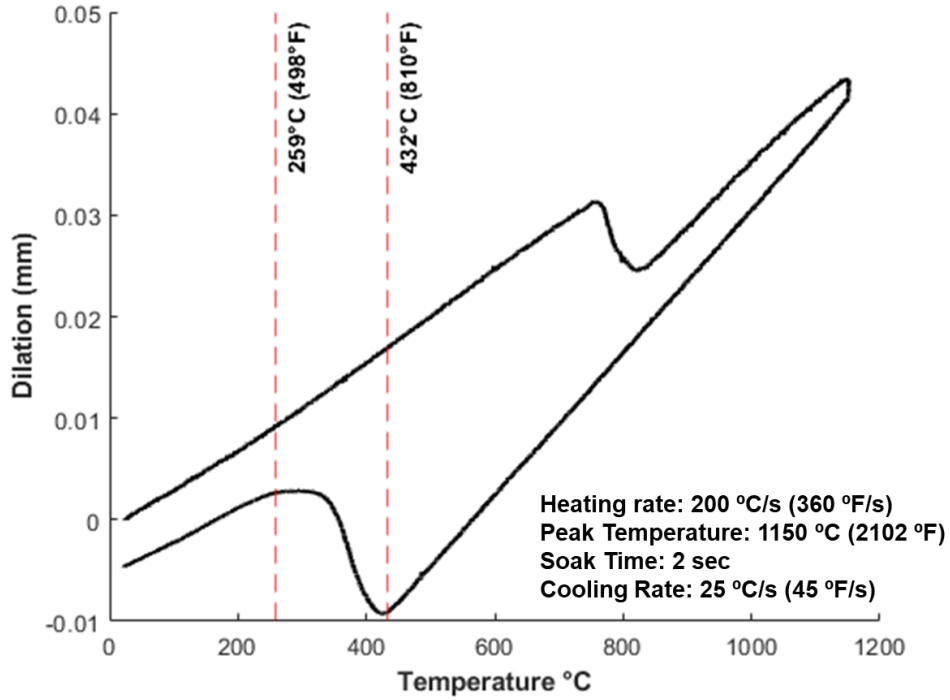

Figure 53. Dilation curve from a HY-100 Gleeble sample heated to a peak temperature of 1150 °C and cooled at 25 °C/s.

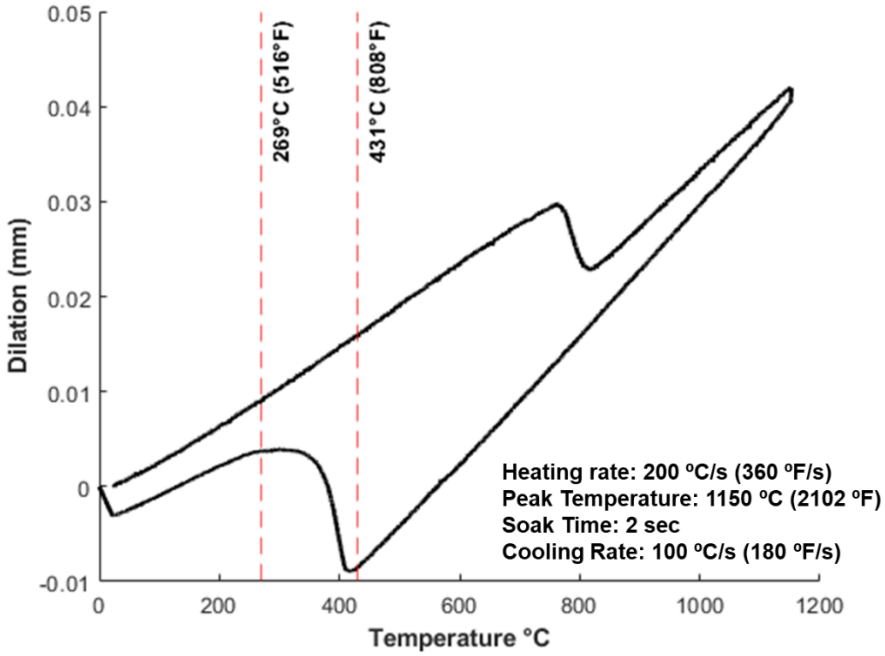

Figure 54. Dilation curve from a HY-100 Gleeble sample heated to a peak temperature of 1150 °C and cooled at 100 °C/s.

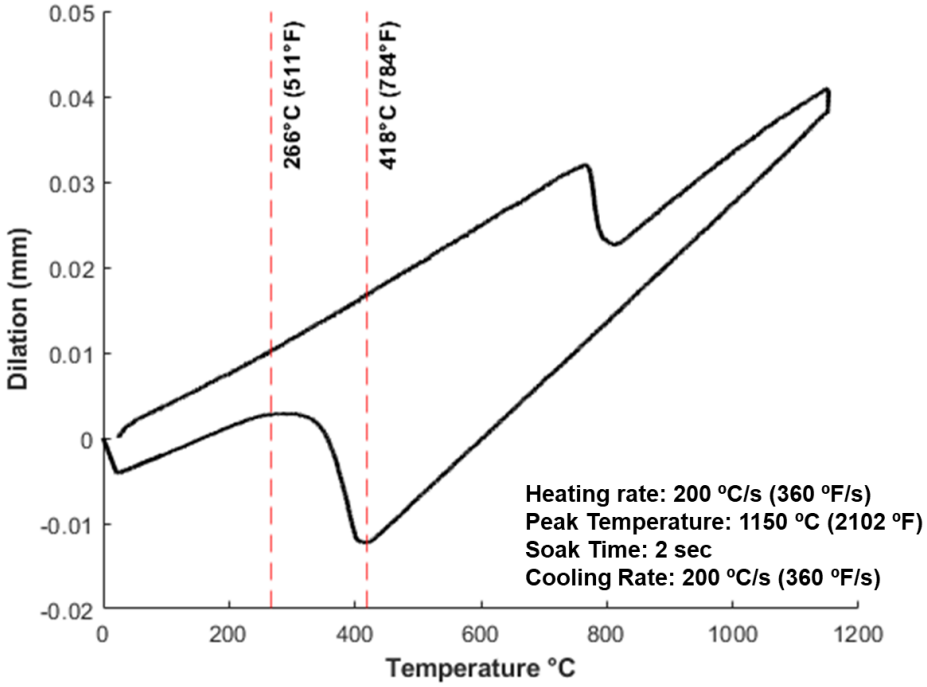

Figure 55. Dilation curve from a HY-100 Gleeble sample heated to a peak temperature of 1150 °C and cooled at 200 °C/s.

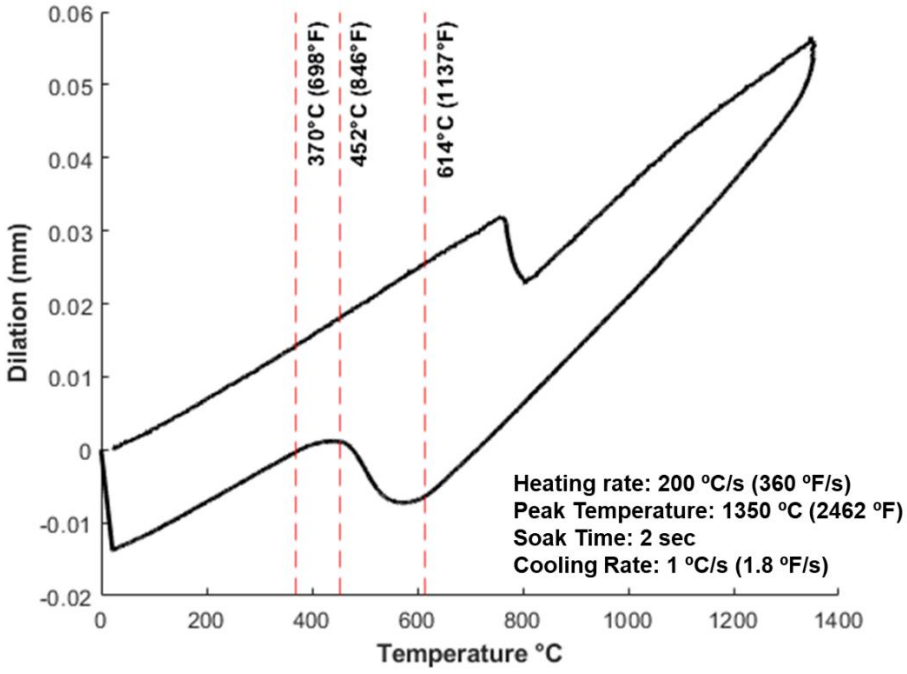

Figure 56. Dilation curve from a HY-100 Gleeble sample heated to a peak temperature of 1350 °C and cooled at 1 °C/s.

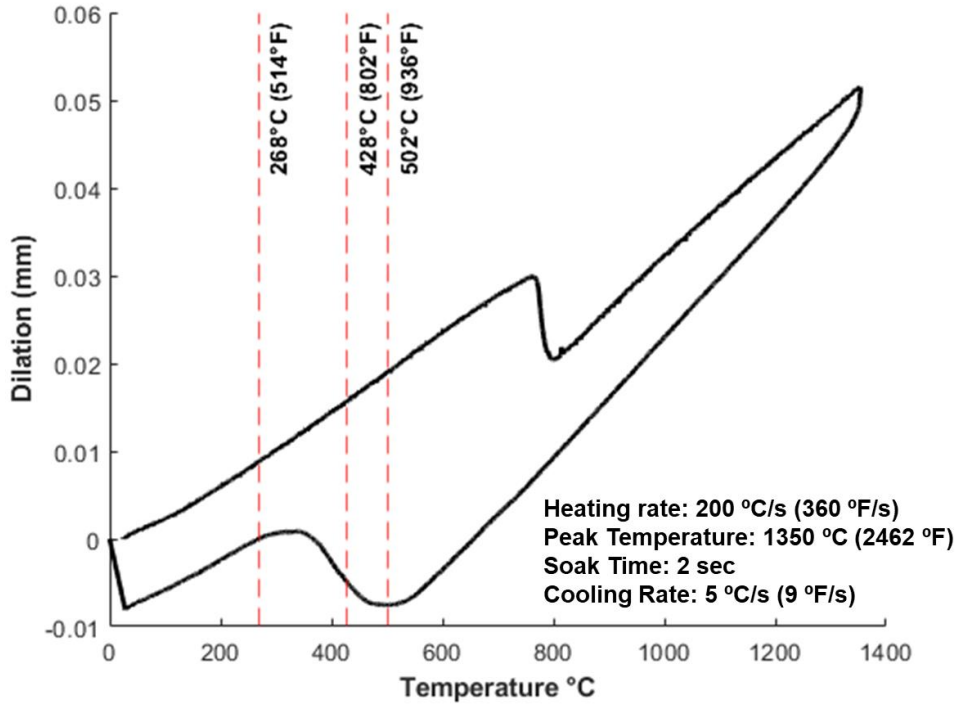

Figure 57. Dilation curve from a HY-100 Gleeble sample heated to a peak temperature of 1350 °C and cooled at 5 °C/s.

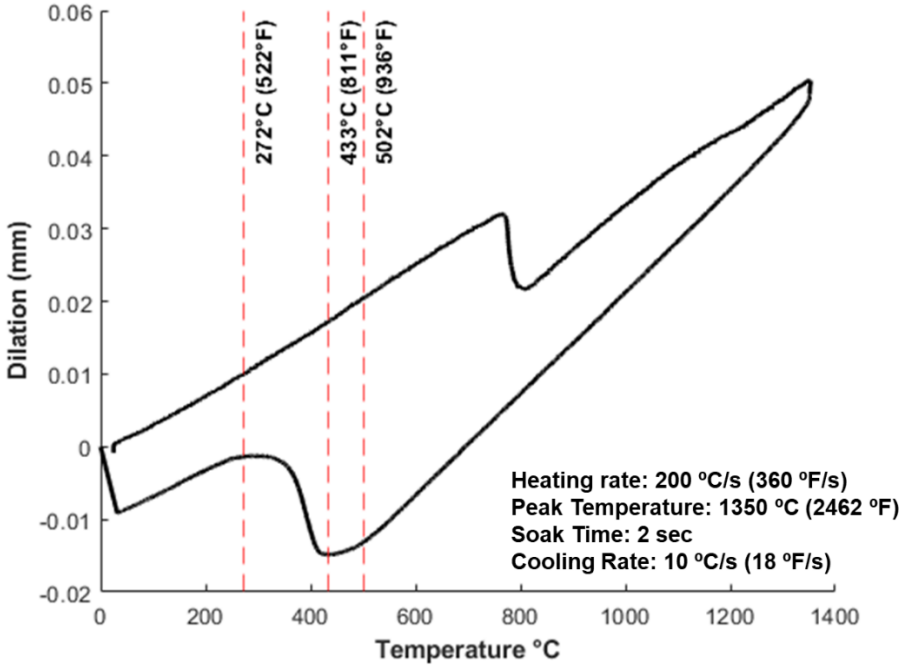

Figure 58. Dilation curve from a HY-100 Gleeble sample heated to a peak temperature of 1350 °C and cooled at 10 °C/s.

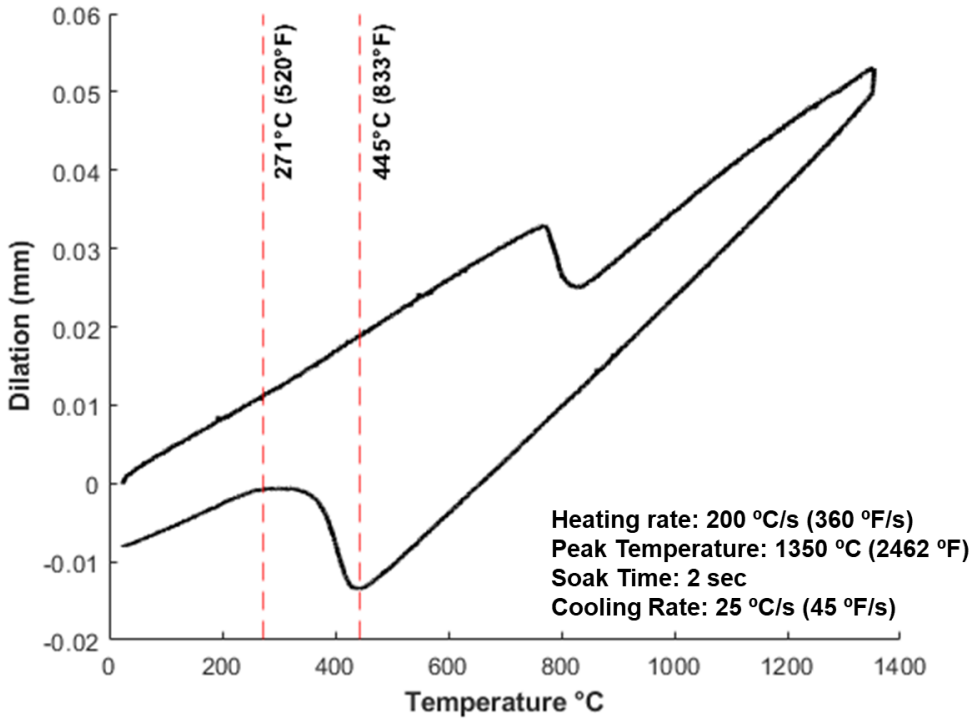

Figure 59. Dilation curve from a HY-100 Gleeble sample heated to a peak temperature of 1350 °C and cooled at 25 °C/s.

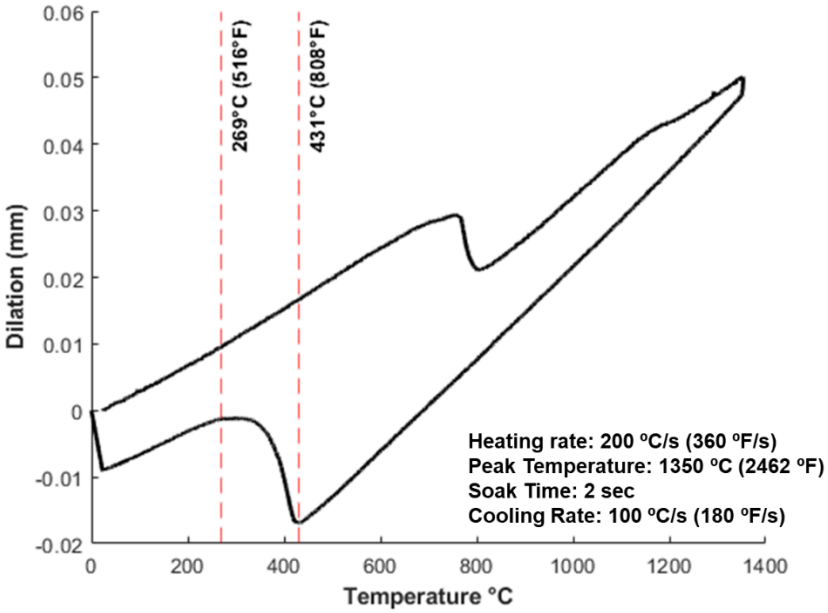

Figure 60. Dilation curve from a HY-100 Gleeble sample heated to a peak temperature of 1350 °C and cooled at 100 °C/s.

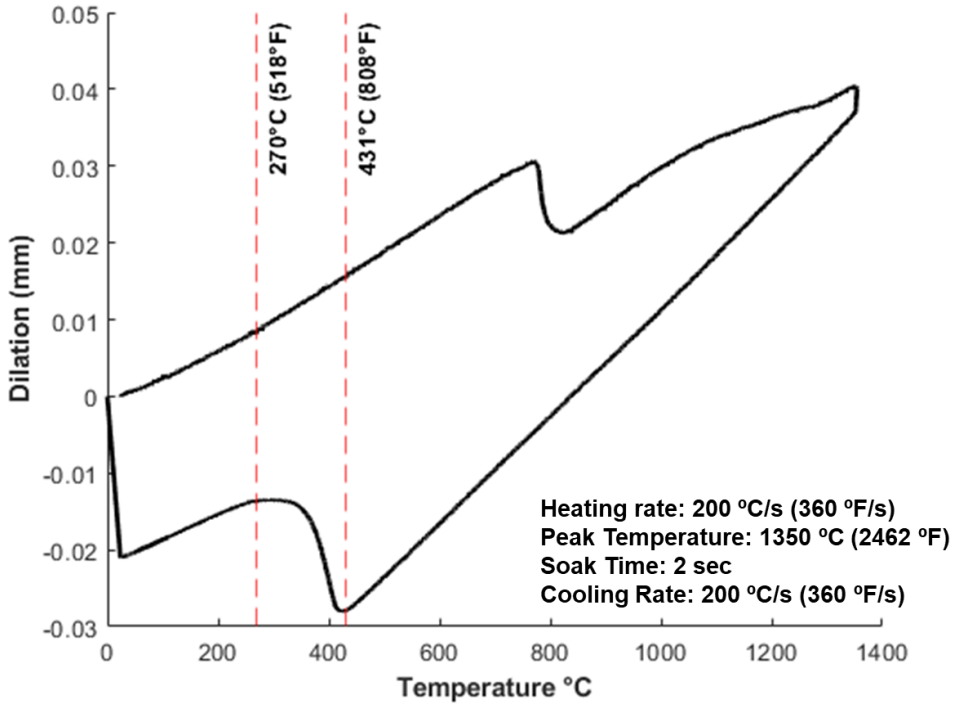

Figure 61. Dilation curve from a HY-100 Gleeble sample heated to a peak temperature of 1350 °C and cooled at 200 °C/s.

Appendix C: Representative Microstructures of HY-100 CCT Specimens

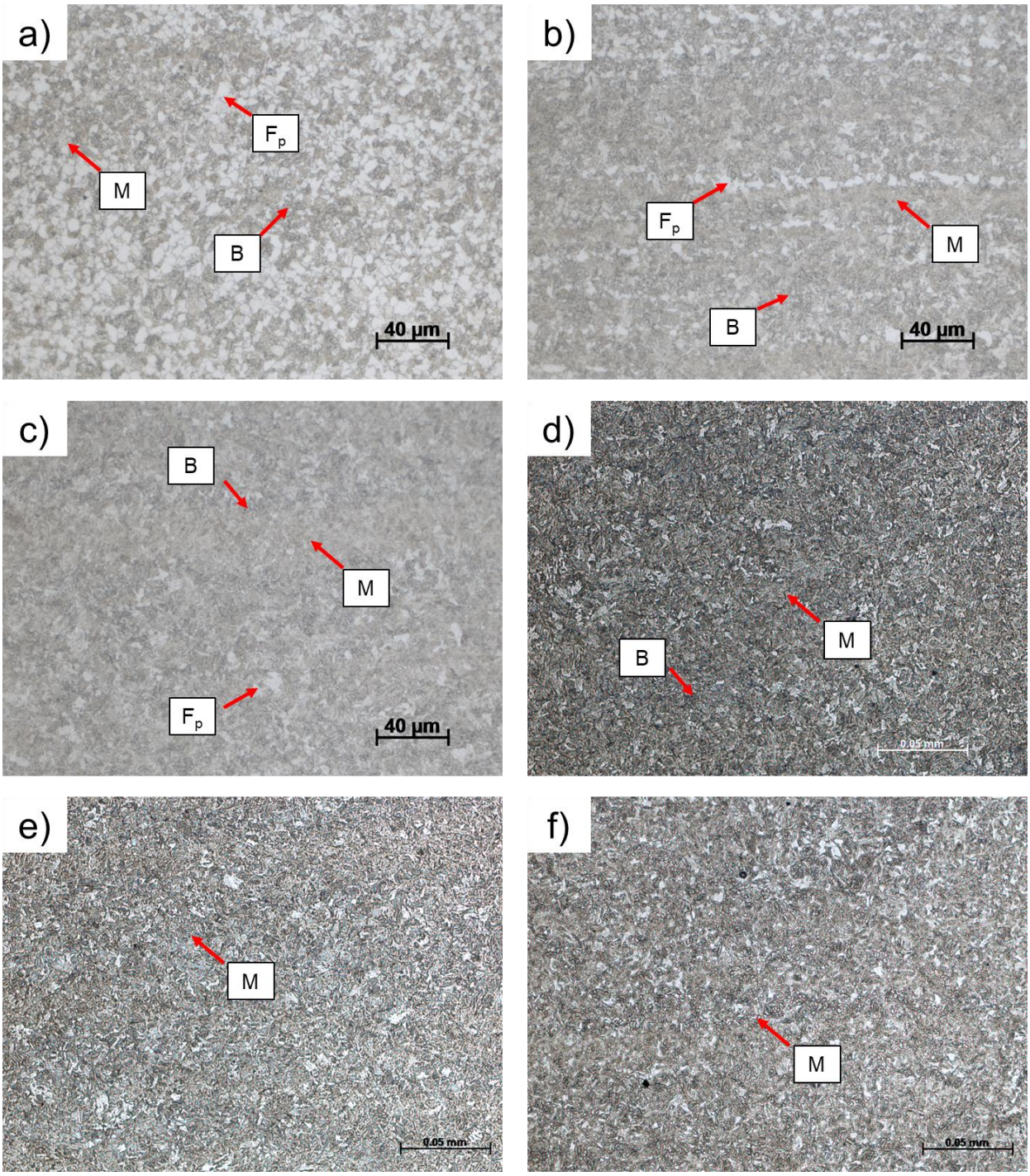

Figure 62. Representative microstructures from HY-100 dilatometry specimens heated to a peak temperature of 785 °C (1445 °F) and continuously cooled at various rates. **(a-f)**: 1, 5, 10, 25, 100, and 200 °C/s (1.8, 9, 18, 45, 180, and 360 °F/s).

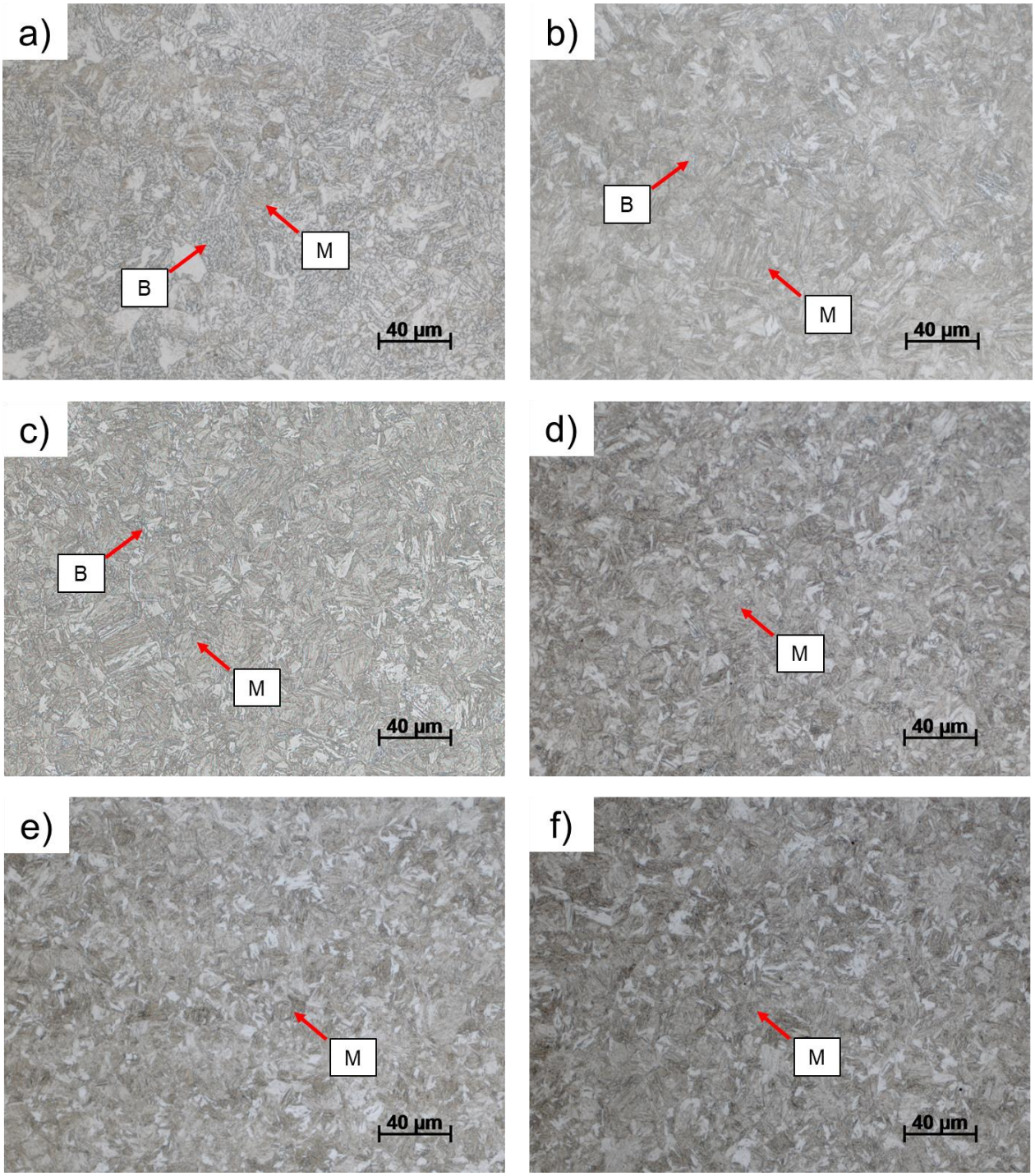

Figure 63. Representative microstructures from HY-100 dilatometry specimen heated to a peak temperature of 1000 °C (1832 °F) and continuously cooled at various rates. **(a-f)**: 1, 5, 10, 25, 100, and 200 °C/s (1.8, 9, 18, 45, 180, and 360 °F/s).

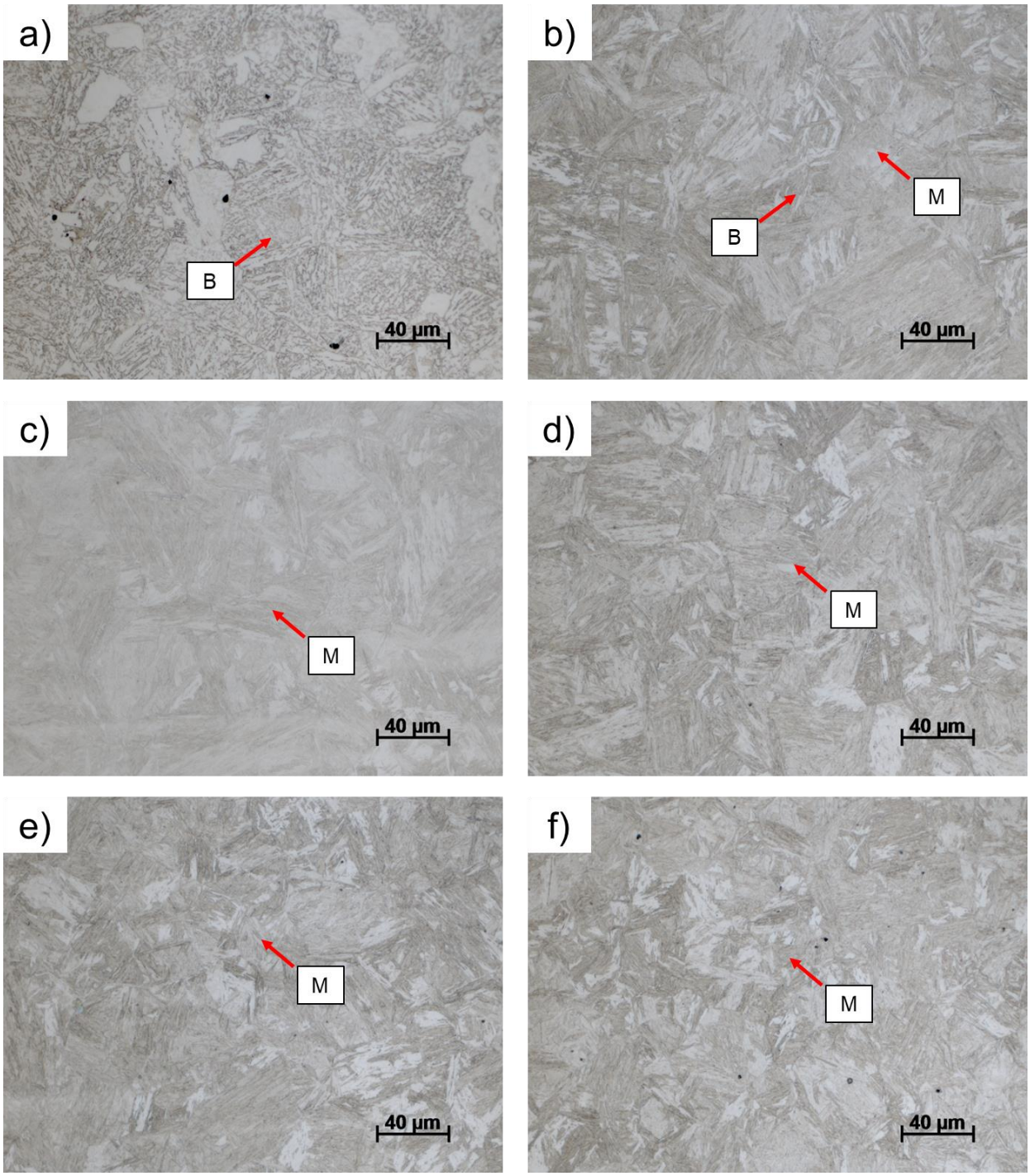

Figure 64. Representative microstructures from HY-100 dilatometry specimens heated to a peak temperature of 1150 °C (2102 °F) and continuously cooled at various rates. **(a-f)**: 1, 5, 10, 25, 100, and 200 °C/s (1.8, 9, 18, 45, 180, and 360 °F/s).

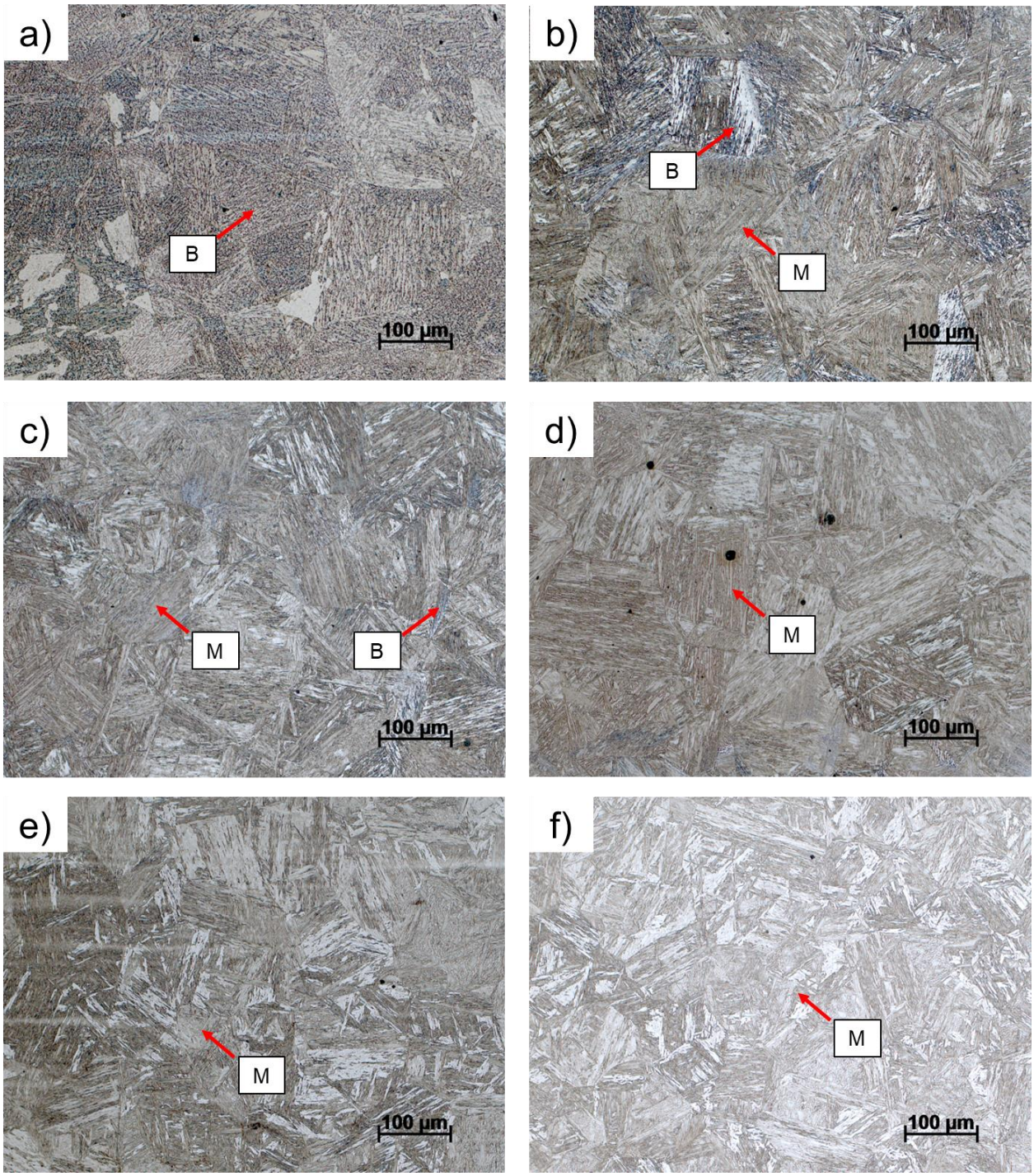

Figure 65. Representative microstructures from HY-100 dilatometry specimens heated to a peak temperature of 1350 °C (2462 °F) and continuously cooled at various rates. **(a-f)**: 1, 5, 10, 25, 100, and 200 °C/s (1.8, 9, 18, 45, 180, and 360 °F/s).

Appendix D: Microhardness Measurements

Table 15. Vickers Microhardness of HY-100 as a Function of Peak Temperature and Cooling Rate. Note: Errors are one standard deviation and values in parenthesis are the number of indents measured.

Cooling Rate		Peak Temperature				
		°C	785	1000	1150	1350
°C/s	°F/s	°F	1445	1832	2102	2462
1	1.8	293 ± 28 (13)		313 ± 20 (20)	284 ± 16 (20)	275 ± 13 (12)
5	9	343 ± 49 (12)		400 ± 37 (18)	444 ± 15 (22)	412 ± 31 (17)
10	18	383 ± 39 (8)		384 ± 31 (20)	436 ± 12 (26)	415 ± 16 (15)
25	45	423 ± 31 (8)		418 ± 23 (18)	426 ± 13 (22)	492 ± 11 (12)
100	180	452 ± 62 (12)		465 ± 15 (22)	443 ± 14 (24)	433 ± 12 (22)
200	360	454 ± 20 (14)		447 ± 7 (22)	449 ± 12 (26)	420 ± 13 (26)

Table 16. Vickers Microhardness Measurements across the Experimental Butt Joint Weldment Illustrated in **Figure 19** (Coordinate Frame Origin at Top Left)

Hardness (HV_{200})	X Coord. (μm)	Y Coord. (μm)	Hardness (HV_{200})	X Coord. (μm)	Y Coord. (μm)	Hardness (HV_{200})	X Coord. (μm)	Y Coord. (μm)
303	17806	147	435	21806	-3353	274	17306	-5353
312	18306	147	264	21306	-3353	284	16806	-5353
359	18806	147	283	20806	-3353	274	16306	-5353
300	20306	-353	288	20306	-3353	267	15806	-5353
302	19806	-353	292	19806	-3353	279	15306	-5353
306	19306	-353	284	19306	-3353	282	14806	-5353
302	18806	-353	284	18806	-3353	290	14306	-5353
311	18306	-353	290	18306	-3353	372	13806	-5353
328	17806	-353	287	17806	-3353	441	13306	-5353
315	17306	-353	271	17306	-3353	414	12806	-5353
315	16806	-353	290	16806	-3353	420	12306	-5353
296	16306	-353	287	16306	-3353	395	11806	-5353
320	15806	-353	432	15806	-3353	387	11306	-5353
313	15306	-353	422	15306	-3353	371	10806	-5353
324	14306	-853	478	14806	-3353	346	10306	-5353
316	14806	-853	450	14306	-3353	369	9806	-5353
315	15306	-853	430	13806	-3353	271	9306	-5353
286	15806	-853	441	13306	-3353	274	8806	-5353
294	16306	-853	439	12806	-3353	276	8306	-5353
296	16806	-853	428	12306	-3353	278	7806	-5353
308	17306	-853	432	11806	-3353	286	7306	-5353
283	17806	-853	399	11306	-3353	281	6806	-5353

293	18306	-853	369	10806	-3353	271	6806	-5853
292	18806	-853	351	10306	-3353	267	7306	-5853
321	19306	-853	347	9806	-3353	286	7806	-5853
318	19806	-853	276	9306	-3353	269	8306	-5853
292	20306	-853	280	8806	-3353	273	8806	-5853
291	20806	-853	275	8306	-3353	264	9306	-5853
302	21306	-853	281	7806	-3353	346	9806	-5853
299	21806	-1353	286	7306	-3353	330	10306	-5853
339	21306	-1353	282	6806	-3353	377	10806	-5853
295	20806	-1353	278	6806	-3853	406	11306	-5853
323	20306	-1353	278	7306	-3853	403	11806	-5853
281	19806	-1353	274	7806	-3853	284	12306	-5853
295	19306	-1353	278	8306	-3853	274	12806	-5853
292	18806	-1353	277	8806	-3853	274	13306	-5853
309	18306	-1353	265	9306	-3853	288	13806	-5853
299	17806	-1353	295	9806	-3853	280	14306	-5853
299	17306	-1353	309	10306	-3853	280	14806	-5853
289	16806	-1353	321	10806	-3853	275	15306	-5853
293	16306	-1353	343	11306	-3853	278	15806	-5853
296	15806	-1353	373	11806	-3853	278	16306	-5853
289	15306	-1353	412	12306	-3853	275	16806	-5853
315	14806	-1353	423	12806	-3853	275	17306	-5853
310	14306	-1353	406	13306	-3853	281	17806	-5853
298	13806	-1353	437	13806	-3853	295	18306	-5853
276	6806	-1853	434	14306	-3853	298	18806	-5853
276	7306	-1853	396	14806	-3853	291	19306	-5853
280	7806	-1853	399	15306	-3853	289	19806	-5853
277	8306	-1853	398	15806	-3853	283	20306	-5853
279	8806	-1853	265	16306	-3853	257	20806	-5853
270	9306	-1853	265	16806	-3853	269	21306	-5853
321	9806	-1853	287	17306	-3853	309	21806	-5853
339	10306	-1853	288	17806	-3853	418	22306	-5853
326	10806	-1853	284	18306	-3853	403	22806	-5853
389	11306	-1853	268	18806	-3853	401	23306	-5853
383	11806	-1853	303	19306	-3853	377	23806	-5853
387	12306	-1853	291	19806	-3853	351	24306	-5853
401	12806	-1853	281	20306	-3853	348	24806	-5853
282	13306	-1853	313	20806	-3853	355	25306	-5853
307	13806	-1853	427	21306	-3853	261	25806	-5853
300	14306	-1853	392	21806	-3853	268	26306	-5853
291	14806	-1853	385	22306	-3853	268	26806	-5853
303	15306	-1853	393	22806	-3853	274	27306	-5853

290	15806	-1853	385	23306	-3853	273	27306	-6353
284	16306	-1853	387	23806	-3853	272	26806	-6353
299	16806	-1853	389	24306	-3853	260	26306	-6353
297	17306	-1853	368	24806	-3853	259	25806	-6353
293	17806	-1853	300	25306	-3853	314	25306	-6353
300	18306	-1853	298	25806	-3853	333	24806	-6353
308	18806	-1853	272	26306	-3853	371	24306	-6353
289	19306	-1853	278	26806	-3853	401	23806	-6353
295	19806	-1853	272	27306	-3853	409	23306	-6353
287	20306	-1853	299	27306	-4353	299	22806	-6353
310	20806	-1853	259	26806	-4353	274	22306	-6353
291	21306	-1853	274	26306	-4353	286	21806	-6353
294	21806	-1853	255	25806	-4353	285	21306	-6353
297	22306	-1853	267	25306	-4353	285	20806	-6353
309	22806	-1853	317	24806	-4353	294	20306	-6353
297	23306	-1853	316	24306	-4353	281	19806	-6353
393	23806	-1853	366	23806	-4353	269	19306	-6353
309	24306	-1853	353	23306	-4353	276	18806	-6353
264	27306	-2353	360	22806	-4353	279	18306	-6353
269	26806	-2353	360	22306	-4353	282	17806	-6353
258	26306	-2353	366	21806	-4353	286	17306	-6353
273	25806	-2353	389	21306	-4353	276	16806	-6353
279	25306	-2353	401	20806	-4353	276	16306	-6353
343	24806	-2353	418	20306	-4353	290	15806	-6353
368	24306	-2353	271	19806	-4353	285	15306	-6353
377	23806	-2353	267	19306	-4353	292	14806	-6353
415	23306	-2353	277	18806	-4353	284	14306	-6353
300	22806	-2353	280	18306	-4353	284	13806	-6353
302	22306	-2353	281	17806	-4353	283	13306	-6353
292	21806	-2353	280	17306	-4353	280	12806	-6353
297	21306	-2353	286	16806	-4353	293	12306	-6353
294	20806	-2353	272	16306	-4353	325	11806	-6353
297	20306	-2353	274	15806	-4353	373	11306	-6353
293	19806	-2353	293	15306	-4353	357	10806	-6353
296	19306	-2353	404	14806	-4353	316	10306	-6353
297	18806	-2353	395	14306	-4353	314	9806	-6353
301	18306	-2353	430	13806	-4353	155	9306	-6353
290	17806	-2353	425	13306	-4353	218	8806	-6353
293	17306	-2353	428	12806	-4353	259	8306	-6353
298	16806	-2353	372	12306	-4353	256	7806	-6353
283	16306	-2353	357	11806	-4353	263	7306	-6353
295	15806	-2353	382	11306	-4353	261	6806	-6353

289	15306	-2353	305	10806	-4353	298	12306	-6853
298	14806	-2353	290	10306	-4353	303	12806	-6853
306	14306	-2353	340	9806	-4353	281	13306	-6853
404	13806	-2353	268	9306	-4353	281	13806	-6853
412	13306	-2353	275	8806	-4353	277	14306	-6853
398	12806	-2353	278	8306	-4353	277	14806	-6853
377	12306	-2353	281	7806	-4353	279	15306	-6853
372	11806	-2353	286	7306	-4353	282	15806	-6853
371	11306	-2353	271	6806	-4353	293	16306	-6853
371	10806	-2353	276	6806	-4853	299	16806	-6853
341	10306	-2353	276	7306	-4853	291	17306	-6853
339	9806	-2353	295	7806	-4853	295	17806	-6853
266	9306	-2353	280	8306	-4853	281	18306	-6853
273	8806	-2353	278	8806	-4853	305	18806	-6853
276	8306	-2353	268	9306	-4853	281	19306	-6853
279	7806	-2353	328	9806	-4853	281	19806	-6853
286	7306	-2353	368	10306	-4853	274	20306	-6853
280	6806	-2353	389	10806	-4853	289	20806	-6853
267	6806	-2853	390	11306	-4853	285	21306	-6853
277	7306	-2853	371	11806	-4853	289	21806	-6853
275	7806	-2853	390	12306	-4853	300	22306	-6853
268	8306	-2853	389	12806	-4853	290	21806	-7353
268	8806	-2853	425	13306	-4853	286	21306	-7353
274	9306	-2853	430	13806	-4853	267	20806	-7353
336	9806	-2853	430	14306	-4853	292	20306	-7353
337	10306	-2853	267	14806	-4853	286	19806	-7353
356	10806	-2853	272	15306	-4853	274	19306	-7353
393	11306	-2853	274	15806	-4853	279	18806	-7353
428	11806	-2853	287	16306	-4853	293	18306	-7353
418	12306	-2853	273	16806	-4853	275	17806	-7353
395	12806	-2853	283	17306	-4853	289	17306	-7353
410	13306	-2853	277	17806	-4853	301	16806	-7353
427	13806	-2853	281	18306	-4853	281	16306	-7353
414	14306	-2853	284	18806	-4853	291	15806	-7353
425	14806	-2853	277	19306	-4853	295	15306	-7353
315	15306	-2853	281	19806	-4853	291	14806	-7353
265	15806	-2853	266	20306	-4853	293	14306	-7353
295	16306	-2853	418	20806	-4853	287	13806	-7353
277	16806	-2853	409	21306	-4853	277	13306	-7353
283	17306	-2853	415	21806	-4853	276	12806	-7353
289	17806	-2853	403	22306	-4853	294	13806	-7853
298	18306	-2853	380	22806	-4853	288	14306	-7853

295	18806	-2853
299	19306	-2853
289	19806	-2853
277	20306	-2853
288	20806	-2853
297	21306	-2853
272	21806	-2853
409	22306	-2853
444	22806	-2853
369	23306	-2853
379	23806	-2853
369	24306	-2853
325	24806	-2853
268	25306	-2853
263	25806	-2853
264	26306	-2853
263	26806	-2853
267	27306	-2853
278	27306	-3353
280	26806	-3353
263	26306	-3353
274	25806	-3353
291	25306	-3353
352	24806	-3353
365	24306	-3353
380	23806	-3353
385	23306	-3353
401	22806	-3353
435	22306	-3353

414	23306	-4853
377	23806	-4853
371	24306	-4853
356	24806	-4853
300	25306	-4853
273	25806	-4853
277	26306	-4853
265	26806	-4853
264	27306	-4853
266	27306	-5353
262	26806	-5353
268	26306	-5353
259	25806	-5353
276	25306	-5353
306	24806	-5353
320	24306	-5353
327	23806	-5353
366	23306	-5353
379	22806	-5353
375	22306	-5353
396	21806	-5353
401	21306	-5353
268	20806	-5353
271	20306	-5353
268	19806	-5353
281	19306	-5353
292	18806	-5353
281	18306	-5353
278	17806	-5353

283	14806	-7853
275	15306	-7853
283	15806	-7853
279	16306	-7853
286	16806	-7853
287	17306	-7853
286	17806	-7853
273	18306	-7853
281	18806	-7853
296	19306	-7853
292	19806	-7853
301	20306	-7853
279	20806	-7853
332	19306	-8353
301	18806	-8353
281	18306	-8353
299	17806	-8353
279	17306	-8353
281	16806	-8353
305	16306	-8353
296	15806	-8353
271	15306	-8353
274	14806	-8353

Table 17. Vickers Microhardness Measurements across the Experimental Tee Joint Weldment Illustrated in **Figure 21** (Coordinate Origin in Top Left Corner)

Hardness (HV_{200})	X Coord. (µm)	Y Coord. (µm)	Hardness (HV_{200})	X Coord. (µm)	Y Coord. (µm)	Hardness (HV_{200})	X Coord. (µm)	Y Coord. (µm)
177	15727	8483	217	10227	-17	342	24227	-3017
173	16227	8483	220	9727	-17	353	23727	-3017
180	16727	8483	225	9227	-17	396	23227	-3017
179	17227	8483	220	8727	-17	382	22727	-3017
176	17727	8483	276	4227	-517	386	22227	-3017
177	18227	8483	283	4727	-517	403	21727	-3017
179	18727	8483	274	5227	-517	404	21227	-3017
172	19227	8483	283	5727	-517	377	20727	-3017
172	19227	7983	285	6227	-517	334	20227	-3017
188	18727	7983	272	6727	-517	359	19727	-3017
169	18227	7983	347	7227	-517	316	19227	-3017
177	17727	7983	403	7727	-517	318	18727	-3017
179	17227	7983	393	8227	-517	305	18227	-3017
178	16727	7983	219	8727	-517	251	17727	-3017
178	16227	7983	302	9227	-517	260	17227	-3017
179	15727	7983	234	9727	-517	270	16727	-3017
181	15727	7483	213	10227	-517	283	16227	-3017
176	16227	7483	219	10727	-517	266	15727	-3017
178	16727	7483	220	11227	-517	264	15227	-3017
170	17227	7483	223	11727	-517	258	14727	-3017
175	17727	7483	216	12227	-517	271	14227	-3017
169	18227	7483	213	12727	-517	352	13727	-3017
178	18727	7483	222	13227	-517	359	13227	-3017
176	19227	7483	317	13727	-517	316	12727	-3017
180	19227	6983	343	14227	-517	320	12227	-3017
183	18727	6983	328	14727	-517	365	11727	-3017
180	18227	6983	303	15227	-517	355	11227	-3017
183	17727	6983	244	15727	-517	339	10727	-3017
182	17227	6983	228	16227	-517	342	10227	-3017
174	16727	6983	203	19227	-517	339	9727	-3017
177	16227	6983	215	19727	-517	312	9227	-3017
186	15727	6983	209	20227	-517	308	8727	-3017
195	15727	6483	206	20727	-517	260	8227	-3017
184	16227	6483	209	21227	-517	271	7727	-3017
181	16727	6483	213	21727	-517	264	7227	-3017
173	17227	6483	217	22227	-517	274	6727	-3017
185	17727	6483	211	22727	-517	269	6227	-3017

188	18227	6483	222	23227	-517	274	5727	-3017
199	18727	6483	219	23727	-517	281	5227	-3017
197	19227	6483	220	24227	-517	269	4727	-3017
216	18727	5983	221	24727	-517	270	4227	-3017
193	18227	5983	274	29227	-1017	280	4227	-3517
185	17727	5983	276	28727	-1017	285	4727	-3517
180	17227	5983	277	28227	-1017	271	5227	-3517
181	16727	5983	274	27727	-1017	275	5727	-3517
195	16227	5983	279	27227	-1017	274	6227	-3517
203	15727	5983	305	26727	-1017	274	6727	-3517
197	15727	5483	341	26227	-1017	272	7227	-3517
189	16227	5483	395	25727	-1017	274	7727	-3517
187	16727	5483	399	25227	-1017	268	8227	-3517
186	17227	5483	219	24727	-1017	286	8727	-3517
193	17727	5483	213	24227	-1017	346	9227	-3517
205	18227	5483	219	23727	-1017	387	9727	-3517
224	18727	5483	223	23227	-1017	335	10227	-3517
222	18727	4983	228	22727	-1017	334	10727	-3517
214	18227	4983	279	22227	-1017	346	11227	-3517
200	17727	4983	229	21727	-1017	361	11727	-3517
193	17227	4983	313	21227	-1017	332	12227	-3517
191	16727	4983	325	20727	-1017	313	12727	-3517
195	16227	4983	347	20227	-1017	313	13227	-3517
198	15727	4983	414	19727	-1017	282	13727	-3517
196	15227	4983	406	19227	-1017	269	14227	-3517
213	14727	4483	383	18727	-1017	269	14727	-3517
197	15227	4483	355	18227	-1017	273	15227	-3517
184	15727	4483	332	17727	-1017	276	15727	-3517
186	16227	4483	348	17227	-1017	275	16227	-3517
193	16727	4483	271	16727	-1017	274	16727	-3517
193	17227	4483	273	16227	-1017	276	17227	-3517
202	17727	4483	267	15727	-1017	271	17727	-3517
211	18227	4483	317	15227	-1017	282	18227	-3517
226	18727	4483	317	14727	-1017	372	18727	-3517
220	19227	4483	347	14227	-1017	298	19227	-3517
224	19727	3983	362	13727	-1017	315	19727	-3517
222	19227	3983	357	13227	-1017	350	20227	-3517
217	18727	3983	356	12727	-1017	334	20727	-3517
227	18227	3983	362	12227	-1017	321	21227	-3517
212	17727	3983	364	11727	-1017	319	21727	-3517
197	17227	3983	380	11227	-1017	357	22227	-3517
187	16727	3983	377	10727	-1017	346	22727	-3517

178	16227	3983	371	10227	-1017	351	23227	-3517
188	15727	3983	382	9727	-1017	362	23727	-3517
192	15227	3983	380	9227	-1017	312	24227	-3517
207	14727	3983	398	8727	-1017	340	24727	-3517
217	14227	3983	392	8227	-1017	351	25227	-3517
226	13727	3483	366	7727	-1017	257	25727	-3517
231	14227	3483	316	7227	-1017	268	26227	-3517
217	14727	3483	272	6727	-1017	270	26727	-3517
197	15227	3483	277	6227	-1017	279	27227	-3517
189	15727	3483	276	5727	-1017	273	27727	-3517
193	16227	3483	283	5227	-1017	273	28227	-3517
186	16727	3483	276	4727	-1017	268	28727	-3517
196	17227	3483	279	4227	-1017	264	29227	-3517
206	17727	3483	283	4227	-1517	271	29227	-4017
206	18227	3483	281	4727	-1517	274	28727	-4017
225	18727	3483	278	5227	-1517	284	28227	-4017
215	19227	3483	286	5727	-1517	280	27727	-4017
216	19727	3483	280	6227	-1517	274	27227	-4017
217	20227	3483	272	6727	-1517	281	26727	-4017
213	20727	2983	286	7227	-1517	280	26227	-4017
232	20227	2983	352	7727	-1517	268	25727	-4017
217	19727	2983	386	8227	-1517	324	25227	-4017
219	19227	2983	392	8727	-1517	357	24727	-4017
226	18727	2983	385	9227	-1517	366	24227	-4017
196	18227	2983	385	9727	-1517	364	23727	-4017
196	17727	2983	380	10227	-1517	382	23227	-4017
206	17227	2983	368	10727	-1517	359	22727	-4017
193	16727	2983	371	11227	-1517	395	22227	-4017
189	16227	2983	382	11727	-1517	360	21727	-4017
192	15727	2983	362	12227	-1517	347	21227	-4017
206	15227	2983	361	12727	-1517	427	20727	-4017
190	14727	2983	359	13227	-1517	364	20227	-4017
225	14227	2983	366	13727	-1517	361	19727	-4017
220	13727	2983	341	14227	-1517	335	19227	-4017
229	13227	2983	348	14727	-1517	359	18727	-4017
220	12727	2483	281	15227	-1517	271	18227	-4017
223	13227	2483	275	15727	-1517	270	17727	-4017
238	13727	2483	273	16227	-1517	265	17227	-4017
229	14227	2483	270	16727	-1517	277	16727	-4017
218	14727	2483	263	17227	-1517	268	16227	-4017
207	15227	2483	320	17727	-1517	274	15727	-4017
196	15727	2483	312	18227	-1517	278	15227	-4017

184	16227	2483	333	18727	-1517	266	14727	-4017
188	16727	2483	365	19227	-1517	268	14227	-4017
196	17227	2483	393	19727	-1517	265	13727	-4017
191	17727	2483	403	20227	-1517	298	13227	-4017
191	18227	2483	410	20727	-1517	335	12727	-4017
213	18727	2483	395	21227	-1517	324	12227	-4017
217	19227	2483	412	21727	-1517	336	11727	-4017
226	19727	2483	404	22227	-1517	348	11227	-4017
229	20227	2483	422	22727	-1517	366	10727	-4017
220	20727	2483	414	23227	-1517	365	10227	-4017
204	21227	2483	417	23727	-1517	364	9727	-4017
225	21727	1983	407	24227	-1517	313	9227	-4017
213	21227	1983	407	24727	-1517	265	8727	-4017
222	20727	1983	410	25227	-1517	263	8227	-4017
227	20227	1983	415	25727	-1517	263	7727	-4017
226	19727	1983	359	26227	-1517	275	7227	-4017
226	19227	1983	333	26727	-1517	284	6727	-4017
206	18727	1983	276	27227	-1517	290	6227	-4017
202	18227	1983	285	27727	-1517	276	5727	-4017
192	17727	1983	276	28227	-1517	277	5227	-4017
188	17227	1983	278	28727	-1517	274	4727	-4017
188	16727	1983	276	29227	-1517	277	4227	-4017
192	16227	1983	289	29227	-2017	263	4227	-4517
191	15727	1983	283	28727	-2017	278	4727	-4517
214	15227	1983	282	28227	-2017	269	5227	-4517
221	14727	1983	286	27727	-2017	282	5727	-4517
227	14227	1983	282	27227	-2017	281	6227	-4517
232	13727	1983	280	26727	-2017	278	6727	-4517
217	13227	1983	362	26227	-2017	276	7227	-4517
222	12727	1983	398	25727	-2017	272	7727	-4517
226	12227	1983	414	25227	-2017	270	8227	-4517
222	11727	1983	409	24727	-2017	263	8727	-4517
232	11227	1483	412	24227	-2017	257	9227	-4517
222	11727	1483	417	23727	-2017	340	9727	-4517
220	12227	1483	425	23227	-2017	348	10227	-4517
218	12727	1483	437	22727	-2017	337	10727	-4517
216	13227	1483	409	22227	-2017	345	11227	-4517
220	13727	1483	428	21727	-2017	334	11727	-4517
217	14227	1483	412	21227	-2017	356	12227	-4517
220	14727	1483	414	20727	-2017	297	12727	-4517
220	15227	1483	404	20227	-2017	264	13227	-4517
190	15727	1483	377	19727	-2017	271	13727	-4517

176	16227	1483	356	19227	-2017	267	14227	-4517
183	16727	1483	351	18727	-2017	266	14727	-4517
185	17227	1483	341	18227	-2017	272	15227	-4517
197	17727	1483	345	17727	-2017	274	15727	-4517
204	18227	1483	267	17227	-2017	269	16227	-4517
208	18727	1483	272	16727	-2017	274	16727	-4517
203	19227	1483	275	16227	-2017	277	17227	-4517
229	19727	1483	277	15727	-2017	263	17727	-4517
222	20227	1483	279	15227	-2017	264	18227	-4517
217	20727	1483	315	14727	-2017	316	18727	-4517
222	21227	1483	347	14227	-2017	325	19227	-4517
222	21727	1483	339	13727	-2017	366	19727	-4517
222	22227	1483	353	13227	-2017	365	20227	-4517
220	22727	983	389	12727	-2017	372	20727	-4517
221	22227	983	376	12227	-2017	350	21227	-4517
222	21727	983	375	11727	-2017	382	21727	-4517
217	21227	983	379	11227	-2017	351	22227	-4517
233	20727	983	382	10727	-2017	365	22727	-4517
236	20227	983	389	10227	-2017	390	23227	-4517
213	19727	983	386	9727	-2017	373	23727	-4517
217	19227	983	390	9227	-2017	361	24227	-4517
213	18727	983	372	8727	-2017	356	24727	-4517
194	18227	983	366	8227	-2017	265	25227	-4517
189	17727	983	362	7727	-2017	274	25727	-4517
177	17227	983	274	7227	-2017	279	26227	-4517
184	16727	983	289	6727	-2017	273	26727	-4517
179	16227	983	282	6227	-2017	276	27227	-4517
183	15727	983	277	5727	-2017	279	27727	-4517
213	15227	983	278	5227	-2017	282	28227	-4517
225	14727	983	279	4727	-2017	283	28727	-4517
224	14227	983	272	4227	-2017	286	29227	-4517
222	13727	983	267	4227	-2517	281	29227	-5017
206	13227	983	280	4727	-2517	273	28727	-5017
209	12727	983	275	5227	-2517	281	28227	-5017
220	12227	983	275	5727	-2517	278	27727	-5017
221	11727	983	264	6227	-2517	278	27227	-5017
218	11227	983	268	6727	-2517	281	26727	-5017
219	10727	983	271	7227	-2517	278	26227	-5017
222	10227	983	271	7727	-2517	276	25727	-5017
233	9727	483	324	8227	-2517	263	25227	-5017
228	10227	483	328	8727	-2517	337	24727	-5017
227	10727	483	294	9227	-2517	355	24227	-5017

224	11227	483	334	9727	-2517	342	23727	-5017
215	11727	483	340	10227	-2517	362	23227	-5017
214	12227	483	361	10727	-2517	347	22727	-5017
222	12727	483	348	11227	-2517	355	22227	-5017
215	13227	483	346	11727	-2517	366	21727	-5017
223	13727	483	333	12227	-2517	372	21227	-5017
220	14227	483	321	12727	-2517	353	20727	-5017
221	14727	483	319	13227	-2517	350	20227	-5017
210	15227	483	341	13727	-2517	357	19727	-5017
190	15727	483	313	14227	-2517	350	19227	-5017
176	16227	483	272	14727	-2517	295	18727	-5017
180	16727	483	276	15227	-2517	262	18227	-5017
183	17227	483	284	15727	-2517	267	17727	-5017
180	17727	483	291	16227	-2517	270	17227	-5017
189	18227	483	281	16727	-2517	268	16727	-5017
192	18727	483	272	17227	-2517	268	16227	-5017
210	19227	483	305	17727	-2517	261	15727	-5017
217	19727	483	383	18227	-2517	271	15227	-5017
218	20227	483	399	18727	-2517	268	14727	-5017
223	20727	483	375	19227	-2517	263	14227	-5017
230	21227	483	387	19727	-2517	260	13727	-5017
219	21727	483	396	20227	-2517	256	13227	-5017
211	22227	483	430	20727	-2517	264	12727	-5017
216	22727	483	417	21227	-2517	285	12227	-5017
226	23227	483	417	21727	-2517	324	11727	-5017
217	23727	-17	412	22227	-2517	339	11227	-5017
217	23227	-17	422	22727	-2517	342	10727	-5017
210	22727	-17	422	23227	-2517	319	10227	-5017
224	22227	-17	432	23727	-2517	270	9727	-5017
224	21727	-17	396	24227	-2517	245	9227	-5017
222	21227	-17	435	24727	-2517	311	19727	-5517
211	20727	-17	340	25227	-2517	313	20227	-5517
213	20227	-17	345	25727	-2517	336	20727	-5517
216	19727	-17	326	26227	-2517	329	21227	-5517
213	19227	-17	277	26727	-2517	337	21727	-5517
208	18727	-17	280	27227	-2517	324	22227	-5517
183	18227	-17	292	27727	-2517	325	22727	-5517
177	17727	-17	282	28227	-2517	327	23227	-5517
189	17227	-17	281	28727	-2517	334	23727	-5517
190	16727	-17	281	29227	-2517	335	24227	-5517
188	16227	-17	265	29227	-3017	264	24727	-5517
194	15727	-17	267	28727	-3017	259	25227	-5517

207	14227	-17	274	28227	-3017	263	25727	-5517
217	13727	-17	280	27727	-3017	264	26227	-5517
215	13227	-17	289	27227	-3017	275	26727	-5517
213	12727	-17	289	26727	-3017	266	27227	-5517
221	12227	-17	274	26227	-3017	282	27727	-5517
216	11727	-17	389	25727	-3017	272	28227	-5517
222	11227	-17	364	25227	-3017	272	28727	-5517
215	10727	-17	328	24727	-3017	263	29227	-5517

Appendix E: Thermo-Physical Property Datasets for HY-100

Table 18. Experimentally Measured Specific Heat of HY-100

Temperature (°C)	c_p (J/g-°C)	(°C)	c_p (J/g-°C)	(°C)	c_p (J/g-°C)	(°C)	c_p (J/g-°C)
23.0	0.4534	320.0	0.5647	620.0	0.7313	920.0	0.5395
30.0	0.4564	330.0	0.5688	630.0	0.7424	930.0	0.5373
40.0	0.4606	340.0	0.5729	640.0	0.7518	940.0	0.5429
50.0	0.4647	350.0	0.5773	650.0	0.7664	950.0	0.56
60.0	0.4688	360.0	0.5815	660.0	0.7847	960.0	0.5497
70.0	0.4728	370.0	0.5858	670.0	0.8063	970.0	0.5586
80.0	0.4768	380.0	0.5904	680.0	0.8157	980.0	0.5606
90.0	0.4808	390.0	0.5951	690.0	0.8283	990.0	0.5604
100.0	0.4847	400.0	0.5996	700.0	0.8499	1000.0	0.5592
110.0	0.4887	410.0	0.6045	710.0	0.867	1010.0	0.5611
120.0	0.4925	420.0	0.6095	720.0	0.8958	1020.0	0.5687
130.0	0.4963	430.0	0.6147	730.0	0.9343	1030.0	0.5611
140.0	0.4999	440.0	0.6199	740.0	1.0651	1040.0	0.566
150.0	0.5034	450.0	0.6243	750.0	1.775	1050.0	0.5705
160.0	0.5071	460.0	0.6295	760.0	1.8871	1060.0	0.5546
170.0	0.5107	470.0	0.6335	770.0	1.475	1070.0	0.5599
180.0	0.5142	480.0	0.6381	780.0	1.1763	1080.0	0.5679
190.0	0.5177	490.0	0.6435	790.0	0.9186	1090.0	0.5956
200.0	0.5214	500.0	0.648	800.0	0.6706	1100.0	0.6037
210.0	0.525	510.0	0.653	810.0	0.5741	1110.0	0.617
220.0	0.5285	520.0	0.6585	820.0	0.5522	1120.0	0.6069
230.0	0.532	530.0	0.6619	830.0	0.5409	1130.0	0.6148
240.0	0.5355	540.0	0.6689	840.0	0.5386	1140.0	0.6263
250.0	0.5388	550.0	0.6725	850.0	0.5447	1150.0	0.629
260.0	0.5421	560.0	0.6765	860.0	0.5449	1160.0	0.635
270.0	0.5453	570.0	0.6828	870.0	0.5421	1170.0	0.6114
280.0	0.5488	580.0	0.6876	880.0	0.545	1180.0	0.6126
290.0	0.5524	590.0	0.6976	890.0	0.5463	1190.0	0.6167
300.0	0.5565	600.0	0.7055	900.0	0.5398	1200.0	0.6171
310.0	0.5605	610.0	0.7165	910.0	0.5351		

Table 19. Experimentally Measured Thermal Properties of HY-100

Temperature (°C)	Thermal Diffusivity (cm^2/sec)	Density (g/cm^3)	Thermal Conductivity (W/cm-°C)
23	0.11228	7.6804	0.39099
50	0.10927	7.6722	0.38958
100	0.10395	7.6581	0.38585
200	0.09467	7.6278	0.37652
300	0.08642	7.5967	0.36534
400	0.07751	7.5628	0.35148
500	0.06842	7.5287	0.33379
600	0.05771	7.4943	0.30512
700	0.04444	7.4623	0.28185
800	0.05892	7.5023	0.27044
900	0.06016	7.4718	0.24264
1000	0.06167	7.4315	0.25628
1100	0.06322	7.3900	0.28205
1200	0.05594	7.3566	0.25395
1300	---	7.3268	---

Appendix F: Thermo-Mechanical Properties

Table 20. Assumed Elevated Temperature Elastic Modulus for HY-100 Base Material. Note: Data are based on an assumed room temperature modulus of 210 GPa (30.5 Msi) as shown in **Figure 27**.

Temperature (°C [°F])	Fraction of Room Temperature Modulus	Elastic Modulus (GPa [Msi])
23 (73)	1.0000	210 (30.5)
100 (212)	1.0000	210 (30.5)
200 (392)	0.9000	189 (27.4)
300 (572)	0.8000	168 (24.4)
400 (752)	0.7000	147 (21.3)
500 (932)	0.6000	126 (18.3)
600 (1112)	0.3100	65 (9.4)
700 (1292)	0.1300	27 (4.0)
800 (1472)	0.0900	19 (2.7)
900 (1652)	0.0675	14 (2.1)
1000 (1832)	0.0450	9 (1.4)
1100 (2012)	0.0225	5 (0.7)
1200 (2192)	0.0000	0 (0)

Table 21. Elevated Temperature Mechanical Properties of HY-100 Base Material. Data as shown in **Figures 28-29**.

Test Temperature (°C [°F])	Yield Strength (MPa [ksi])	Tensile Strength (MPa [ksi])
22 (72)	810 [117]	867 [126]
200 (392)	750 [109]	802 [116]
400 (752)	670 [97]	752 [109]
600 (1112)	410 [59]	476 [69]
700 (1292)	130 [19]	201 [29]
800 (1472)	78 [11]	111 [16]
900 (1652)	66 [10]	74 [11]
1000 (1832)	41 [6]	51 [7]
1100 (2012)	18 [3]	31 [4]

Table 22. Yield Strength of Simulated HY-100 CGHAZs after Heating to 1350 °C (2462 °F) and Cooling at Different Rates. Note: Data as illustrated in **Figure 30**.

Temperature (°C) [°F]	Yield Strength (MPa)			
	1 °C/s Cooling	10 °C/s Cooling	25 °C/s Cooling	100 °C/s Cooling
25 [77]	688	987	1044	1046
200 [392]	714	1027	989	1035
400 [752]	524	852	873	851
600 [1112]	387	337	344	347
700 [1292]	187	126	133	129

Table 23. On-Heating Flow Behavior of HY-100 Base Material. Note: Data as shown in **Figures 32-33**.

22 °C (72 °F)		200 °C (392 °F)		400 °C (752 °F)		600 °C (1112 °F)		700 °C (1292 °F)	
$\varepsilon_{p,\,true}$	σ (MPa)	$\varepsilon_{p,\,true}$	σ (MPa)	$\varepsilon_{p,\,true}$	σ (MPa)	$\varepsilon_{p,\,true}$	σ (MPa)	$\varepsilon_{p,\,true}$	σ (MPa)
0.0000	810	**0.0000**	750	**0.0000**	670	**0.0000**	410	**0.0000**	130
0.0050	840	**0.0050**	764	**0.0050**	730	**0.0050**	470	**0.0050**	158
0.0100	848	**0.0100**	780	**0.0100**	745	**0.0100**	480	**0.0100**	170
0.0200	860	**0.0200**	800	**0.0200**	765	**0.0200**	485	**0.0200**	190
0.0300	870	**0.0300**	820	**0.0300**	775	**0.0300**	490	**0.0300**	202
0.0400	885	**0.0400**	835	**0.0400**	780	**0.0400**	490	**0.0400**	208
0.0500	900	**0.0500**	835	**0.0500**	780	**0.0500**	490	**0.0500**	211
0.1000	960	**0.1000**	835	**0.1000**	780	**0.1000**	490	**0.1000**	220
0.2000	1060	**0.2000**	835	**0.2000**	780	**0.2000**	490	**0.2000**	223

800 °C (1472 °F)		900 °C (1652 °F)		1000 °C (1832 °F)		1100 °C (2012 °F)	
$\varepsilon_{p,\,true}$	σ (MPa)	$\varepsilon_{p,\,true}$	σ (MPa)	$\varepsilon_{p,\,true}$	σ (MPa)	$\varepsilon_{p,\,true}$	σ (MPa)
0.0000	78	**0.000**	66	**0.000**	41	**0.000**	18
0.0050	90	**0.005**	69	**0.005**	46	**0.005**	25
0.0100	96	**0.010**	70.5	**0.010**	48.5	**0.010**	27
0.0200	103	**0.020**	73.5	**0.020**	50.5	**0.020**	29
0.0300	107	**0.030**	75	**0.030**	52	**0.030**	30
0.0400	110	**0.040**	76.5	**0.040**	53	**0.040**	31
0.0500	112	**0.050**	77.5	**0.050**	54	**0.050**	32
0.1000	122	**0.100**	82	**0.100**	55	**0.100**	34.5
0.2000	135	**0.200**	90	**0.200**	56	**0.200**	36.5
		0.300	98	**0.300**	56	**0.300**	39
		0.400	102	**0.400**	56	**0.400**	42

Table 24. Flow Stress of Simulated HY-100 CGHAZs after Heating to 1350 °C (2462 °F) and Cooling at 1 °C/s (1.8 °F/s). Note: Data as illustrated in **Figure 34** and terminal values are the true stress and strain at rupture.

25 °C (77 °F)		200 °C (392 °F)		400 °C (752 °F)		600 °C (1112 °F)		700 °C (1292 °F)	
$\varepsilon_{p,\,true}$	σ (MPa)	$\varepsilon_{p,\,true}$	σ (MPa)	$\varepsilon_{p,\,true}$	σ (MPa)	$\varepsilon_{p,\,true}$	σ (MPa)	$\varepsilon_{p,\,true}$	σ (MPa)
0.000	687.90	**0.000**	713.90	**0.000**	523.80	**0.000**	386.80	**0.000**	187.10
0.005	796.50	**0.005**	800.36	**0.005**	668.16	**0.005**	451.71	**0.003**	198.81
0.010	844.10	**0.010**	836.02	**0.010**	727.13	**0.010**	464.56		
0.020	895.50	**0.020**	868.98	**0.020**	778.17	**0.017**	459.82		
0.030	926.50	**0.030**	886.79	**0.030**	804.88				
0.040	950.20	**0.040**	902.47	**0.040**	817.84				
0.050	965.50	**0.050**	915.37	**0.044**	820.21				
0.100	1006.20	**0.100**	952.18						
0.139	1004.08	**0.144**	963.90						

Table 25. Flow Stress of Simulated HY-100 CGHAZs after Heating to 1350 °C (2462 °F) and Cooling at 10 °C/s (18 °F/s). Note: Data as illustrated in **Figure 35** and terminal values are the true stress and strain at rupture.

25 °C (77 °F)		200 °C (392 °F)		400 °C (752 °F)		600 °C (1112 °F)		700 °C (1292 °F)	
$\varepsilon_{p,\,true}$	σ (MPa)	$\varepsilon_{p,\,true}$	σ (MPa)	$\varepsilon_{p,\,true}$	σ (MPa)	$\varepsilon_{p,\,true}$	σ (MPa)	$\varepsilon_{p,\,true}$	σ (MPa)
0.000	986.90	**0.000**	1027.00	**0.000**	852.10	**0.000**	337.10	**0.000**	150.01
0.005	1194.72	**0.005**	1238.56	**0.005**	970.33	**0.005**	421.60	**0.005**	155.85
0.010	1287.32	**0.010**	1340.66	**0.010**	1006.18	**0.010**	445.25	**0.010**	160.20
0.020	1363.66	**0.020**	1588.67	**0.020**	1021.70	**0.017**	449.64	**0.020**	162.10
0.030	1393.48	**0.030**	1588.67	**0.023**	1022.72			**0.030**	162.21
0.040	1407.69	**0.040**	1588.67						
0.050	1412.89	**0.050**	1588.67						
0.060	1413.76	**0.100**	1588.67						
		0.106	1588.67						

Table 26. Flow Stress of Simulated HY-100 CGHAZs after Heating to 1350 °C (2462 °F) and Cooling at 25 °C/s (45 °F/s). Data as illustrated in **Figure 36** and terminal values are the true stress and strain at rupture.

25 °C (77 °F)		200 °C (392 °F)		400 °C (752 °F)		600 °C (1112 °F)		700 °C (1292 °F)	
$\varepsilon_{p,\,true}$	σ (MPa)	$\varepsilon_{p,\,true}$	σ (MPa)	$\varepsilon_{p,\,true}$	σ (MPa)	$\varepsilon_{p,\,true}$	σ (MPa)	$\varepsilon_{p,\,true}$	σ (MPa)
0.000	1043.66	**0.000**	988.91	**0.000**	872.67	**0.000**	344.38	**0.000**	133.10
0.005	1248.73	**0.005**	1199.55	**0.005**	984.55	**0.005**	429.29	**0.005**	155.12
0.010	1342.12	**0.010**	1300.13	**0.010**	1025.29	**0.010**	453.97	**0.010**	160.97
0.020	1422.13	**0.020**	1543.17	**0.020**	1048.04	**0.017**	460.37	**0.020**	165.01
0.030	1452.54	**0.030**	1543.17	**0.025**	1050.04			**0.030**	166.77
0.040	1467.42	**0.040**	1543.17					**0.040**	165.74
0.050	1473.64	**0.050**	1543.17					**0.047**	165.88
0.061	1475.19	**0.100**	1543.17						
		0.105	*1543.17*						

Table 27. Flow Stress of Simulated HY-100 CGHAZs after Heating to 1350 °C (2462 °F) and Cooling at 100 °C/s (180 °F/s). Data as illustrated in **Figure 37** and terminal values are the true stress and strain at rupture.

25 °C (77 °F)		200 °C (392 °F)		400 °C (752 °F)		600 °C (1112 °F)		700 °C (1292 °F)	
$\varepsilon_{p,\,true}$	σ (MPa)	$\varepsilon_{p,\,true}$	σ (MPa)	$\varepsilon_{p,\,true}$	σ (MPa)	$\varepsilon_{p,\,true}$	σ (MPa)	$\varepsilon_{p,\,true}$	σ (MPa)
0.000	1214.01	**0.000**	1038.54	**0.000**	850.83	**0.000**	346.99	**0.000**	129.09
0.005	1289.29	**0.005**	1221.07	**0.005**	969.46	**0.005**	417.18	**0.005**	151.28
0.010	1356.70	**0.010**	1313.73	**0.010**	1012.81	**0.010**	435.75	**0.010**	156.36
0.020	1382.28	**0.020**	1402.78	**0.020**	1038.02	**0.013**	346.99	**0.020**	159.17
0.030	1395.27	**0.030**	1448.93	**0.029**	1040.76			**0.026**	160.73
0.040	1400.47	**0.040**	1478.10						
0.050	1401.14	**0.050**	1495.22						
0.059	1402.62	**0.100**	1540.67						

Table 28. Engineering Fracture Strain for the Specimens Shown in **Figures 34-36**.

Temperature (°C) [°F]	Fracture Strain, $\varepsilon_{f,\,eng}$ (mm/mm)			
	1 °C/s Cooling	10 °C/s Cooling	25 °C/s Cooling	100 °C/s Cooling
25 [77]	0.217	0.147	0.180	0.190
200 [392]	0.190	0.127	0.134	0.066
400 [752]	0.056	0.139	0.167	0.156
600 [1112]	0.130	0.099	0.025	0.026
700 [1292]	0.049	0.177	0.159	0.136

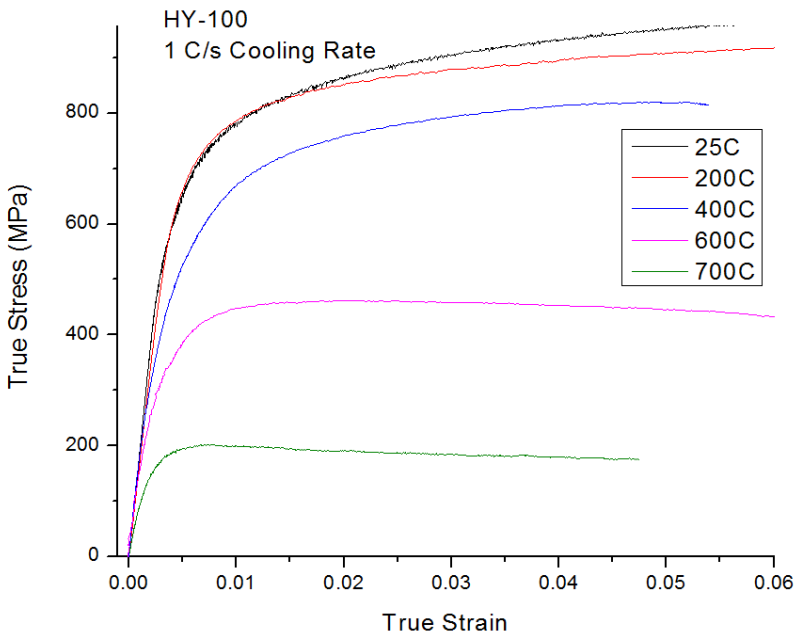

Figure 66. Uniaxial tension stress-strain curves from Gleeble tensile samples thermally cycled to a peak temperature of 1350 °C (2462 °F), cooled at 1 °C/s (1.8 °F/s), then reheated to the test temperature.

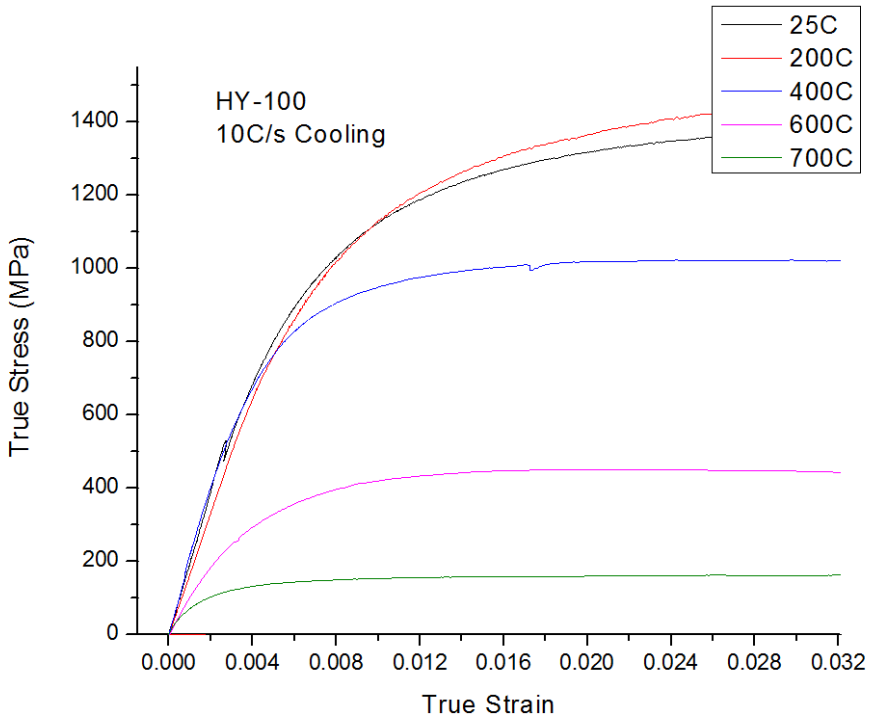

Figure 67. Uniaxial tension stress-strain curves from Gleeble tensile samples thermally cycled to a peak temperature of 1350 °C (2462 °F), cooled at 10 °C/s (18 °F/s), then reheated to the test temperature.

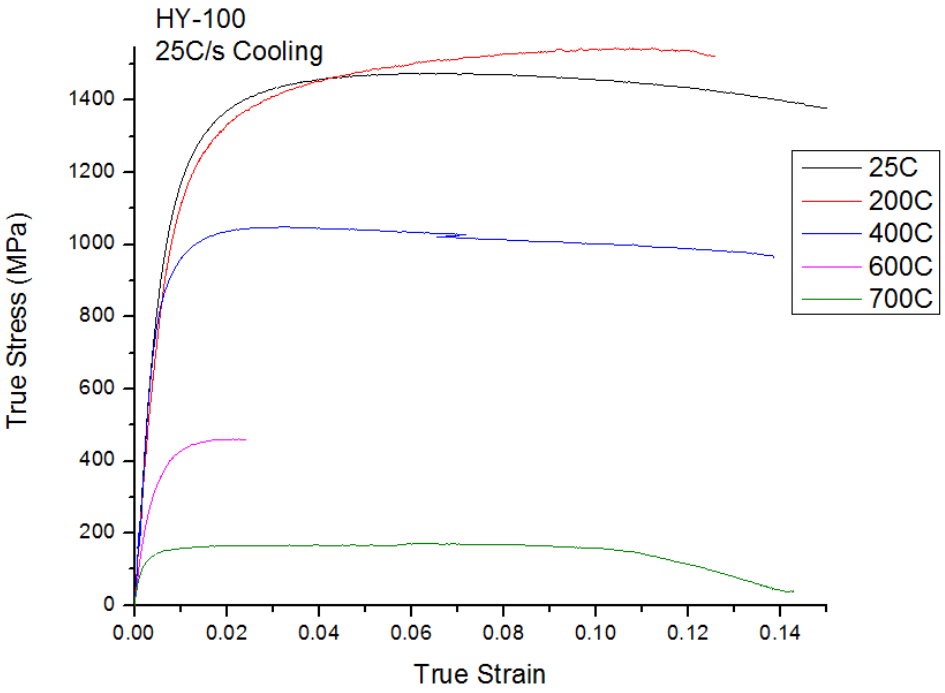

Figure 68. Uniaxial tension stress-strain curves from Gleeble tensile samples thermally cycled to a peak temperature of 1350 °C (2462 °F), cooled at 25 °C/s (45 °F/s), then reheated to the test temperature.

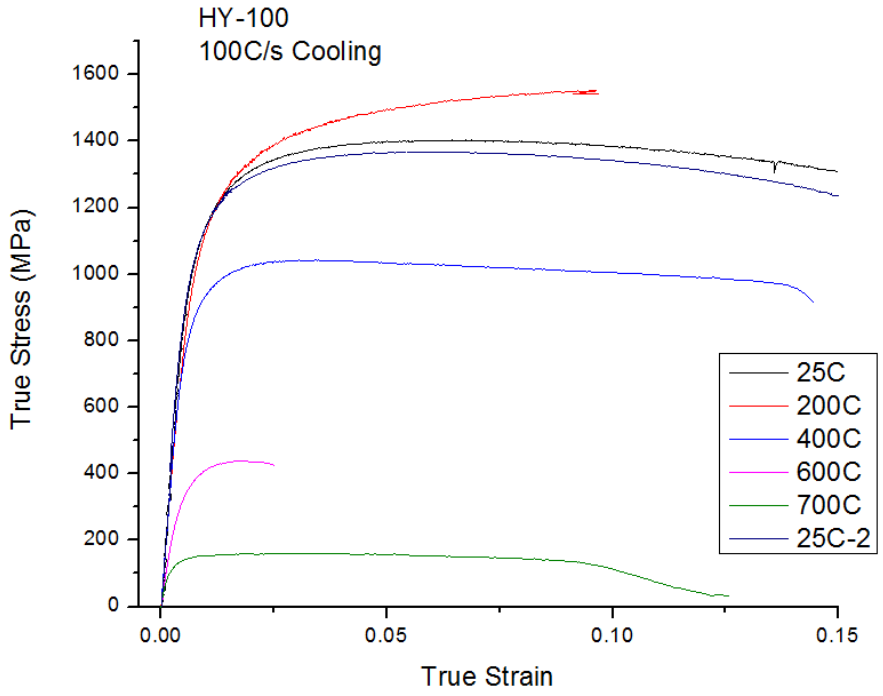

Figure 69. Uniaxial tension stress-strain curves from Gleeble tensile samples thermally cycled to a peak temperature of 1350 °C (2462 °F), cooled at 100 °C/s (180 °F/s), then reheated to the test temperature.

REFERENCES

[1] L. F. Andersen, "Residual Stresses and Deformations in Steel Structures," Doctoral Thesis, Department of Naval Architecture and Offshore Engineering, University of Denmark, 2000.

[2] MIL-S-22698C, "Military Specification: Steel Plate, Shapes, and Bars, Weldable Ordinary Strength and Higher Strength: Structural," 29 June 1988.

[3] ASTM A945/M-16, "Standard Specification for High-Strength Low-Alloy Structural Steel Plate with Low Carbon and Restricted Sulfur for Improved Weldability, Formability, and Toughness," ASTM International, West Conshohocken, PA, 2016.

[4] NAVSEA Technical Publication T9074-BD-GIB-010/0300 Rev. 2, "Base Materials for Critical Applications: Requirements for Low Alloy Steel Plate, Forgings, Castings, Shapes, Bars, and Heats of HY-80/100/130 and HSLA-80/100," 18 December 2012.

[5] D. H. Bechetti, J. K. Semple, C. R. Fisher and W. Zhang, "Temperature-Dependent Material Property Databases for Marine Steels - Part 1: DH36," NSWCCD-61-TR-2019/03, 2019.

[6] J. K. Semple, D. H. Bechetti, W. Zhang and C. R. Fisher, "Temperature-Dependent Material Property Databases for Marine Steels - Part 2: HSLA-65," NSWCCD-61-TR-2020/03, 2020.

[7] J. K. Semple, D. H. Bechetti, W. Zhang and C. R. Fisher, "Temperature-Dependent Material Property Databases for Marine Steels - Part 3: HSLA-80," NSWCCD-61-TR-2020/24, 2020.

[8] J. K. Semple, D. H. Bechetti, W. Zhang and C. R. Fisher, "Temperature-Dependent Material Property Databases for Marine Steels – Part 4: HSLA-100," NSWCCD-61-TR-2021/10, 2021.

[9] J. K. Semple, D. H. Bechetti, W. Zhang, J. E. Norkett and C. R. Fisher, "Temperature-Dependent Material Property Databases for Marine Steels – Part 5: HY-80," NSWCCD-61-TR-2023/19, 2023.

[10] ASTM E417-17, "Standard Test Method for Analysis of Carbon and Low-Alloy Steel by Spark Atomic Emission Spectrometry," ASTM International, West Conshohocken, PA, 2017.

[11] ASTM E1019-18, "Standard Test Methods for Determination of Carbon, Sulfur, Nitrogen, and Oxygen in Steel, Iron, Nickel, and Cobalt Alloys by Various Combustion and Inert Gas Fusion Techniques," ASTM International, West Conshohocken, PA, 2018.

[12] G. R. Eisler and P. W. Fuerschbach, "SOAR: An Extensible Suite of Codes for Weld Analysis and Optimal Weld Schedules," in *Seveth International Conference on Computer Technology in Welding*, San Francisco, CA, 1997.

[13] ASTM E1461-13, "Standard Test Method for Thermal Diffusivity by the Flash Method," ASTM International, West Conshohocken, PA, 2013.

[14] ASTM E1269-11 (2018), "Standard Test Method for Determining Specific Heat Capacity by Differential Scanning Calorimetry," ASTM International, West Conshohocken, PA, 2018.

[15] ASTM A370-18, "Standard Test Methods and Definitions for Mechanical Testing of Steel Products," ASTM International, West Conshohocken, PA, 2018.

[16] ASTM E21-17, "Standard Test Methods for Elevated Temperature Tension Tests of Metallic Materials," ASTM International, West Conshohocken, PA, 2017.

[17] T. D. Huang, M. Harbison, S. Scholler, H. Rucker, J. Hu, P. Dong, M. Collette, H. Chung, M. Groden, W. Zhang, J. Semple, R. Kirchain, R. Roth, M. Bustamante, Y. Yang, R. Dull, Y. Gooroochurn, M. Doroudian, C. F. Fisher, M. Sinfield, D. Kihl and A. Gonzalez, "Robust Distortion Control Methods and Implementation for Construction of Lightweight Metallic Structures," *SNAME Transactions*, 2016.

[18] N. Yurioka, S. Oshita and H. Tamehiro, "Determination of Necessary Preheating Temperature in Steel Welding," *Welding Journal*, vol. 52, no. 6, pp. 147-s to 153-s, 1983.

[19] C. A. Papesch and J. J. Valencia, "Thermophysical Properties for HY-100 Steel Plate Base Metal and HY-100/MIL-100 S-1 Weld," Naval Center of Excellence for Manufacturing Technology (NCEMT) Laboratory Report WO 0066, Johnstown, PA, September 1998.

[20] T. J. Holmquist, "Strength and Fracture Characteristics of HY-80, HY-100, and HY-130 Steels Subjected to Various Strains, Strain Rates, Temperatures, and Pressures," NSWC TR 88-252, 1987.

[21] X. Yue, J. C. Lippold, B. T. Alexandrox and S. S. Babu, "Continuous Cooling Transformatoin Behavior in the CGHAZ of Naval Steels," *Welding Journal*, vol. 91, no. 3, pp. 67-s to 75-s, 2012.

[22] M. Peet, "Prediction of Martensite Start Temperature," *Materials Science and Technology*, vol. 31, no. 11, pp. 1370-1375, 2014.

[23] S. Kang, S. Yoon and S.-J. Lee, "Prediction of Bainite Start Temperature in Alloy Steels with Difference Grain Sizes," *ISIJ International*, vol. 54, no. 4, pp. 997-999, 2014.

[24] C. Capdevilla, F. G. Caballero and C. Garcia de Andres, "Determination of Ms Temperature in Steels: A Bayesian Neural Network Model," *ISIJ International*, vol. 42, pp. 894-902, 2002.

[25] J. S. Kirkaldy and D. Venugopalan, "Phase Transformations in Ferrous Alloys," in *Phase Transformations in Ferrous Alloys: Proceedings of an International Conference*, Philadelphia, PA, 1984.

[26] Bainite Committee of The Iron & Steel Institute of Japan, "Atlas for Bainitic Microstructures, Vol. 1: Continuous-Cooled Microstructures of Low Carbon HSLA Steels," The Iron & Steel Institute of Japan, 1992.

[27] H. K. D. H. Bhadeshia and R. W. K. Honeycombe, Steels: Microstructure and Properties, 3 ed., Oxford, UK: Butterwoth-Heinemann, 2006.

[28] A. K. Sinha, Ferrous Physical Metallurgy, Stoneham, MA: Butterworth Publishers, 1989.

[29] G. Thewlis, "Classification and Quantification of Microstructures in Steels," *Materials Science and Technology*, vol. 20, pp. 143-160, 2004.

[30] International Institute of Welding, Compendium of Weld Metal Microstructures and Properties: Submerged-arc Welds in Ferritic Steel, Cambridge, UK: Woodhead Publishing, 1985.

[31] "HY-100 (High Strength, Tough Plate Steel)," in *Alloy Digest*, Upper Montclair, NJ, Engineering Alloy Digest, August 1970, pp. Filing Code: SA-255.

[32] ASTM E111-17, "Standard Test Method for Young's Modulus, Tangent Modulus, and Chord Modulus," ASTM International, West Conshohocken, PA, 2017.

[33] E. 1993-1-1, "Eurocode 3: Design of steel structures - Part 1-1: General rules and rules for buildings," 2005.

[34] E. 1993-1-2, "Eurocode 3: Design of steel structures - Part 1-2: General rules - Structural fire design," 2005.

This page intentionally left blank

DISTRIBUTION

EXTERNAL

	Copies
DEFENSE TECHNICAL INFORMATION CENTER 727 JOHN J KINGMAN ROAD SUITE 0944 FORT BELVOIR, VA 22060-6218	1
RESEARCH COMMONS NAVAL UNDERSEA WARFARE CENTER BUILDING 101 NEWPORT, RI 02841	1
COMMANDER ATTN: SEA 05P2 NAVAL SEA SYSTEMS COMMAND 1333 ISAAC HULL AVENUE S.E. WASHINGTON NAVY YARD WASHINGTON, DC 20376 ATTN: Archer, Bjornson, McGrorey, Melvin	4
ATTN: SEA 05P4 NAVAL SEA SYSTEMS COMMAND 1333 ISAAC HULL AVENUE S.E. WASHINGTON NAVY YARD WASHINGTON, DC 20376 ATTN: Rodgers	1
OFFICE OF NAVAL RESEARCH 875 N RANDOLPH ST ARLINGTON, VA 22217 ATTN: Farren, Mullins	2
LIGHTWEIGHT INNOVATIONS FOR TOMORROW (LIFT) 1400 ROSA PARKS BOULEVARD DETROIT, MI 48216 ATTN: Hawke	1
HUNTINGTON-INGALLS INDUSTRIES – INGALLS SHIPBUILDING 100 JERRY ST PE HIGHWAY PASCAGOULA, MS 39581 ATTN: Scholler, Yang	2
OHIO STATE UNIVERSITY WELDING ENGINEERING PROGRAM 1248 ARTHUR E ADAMS DR COLUMBUS, OH 43221 ATTN: Zhang	1

NSWCCD INTERNAL DISTRIBUTION

Code	Name	Copies
60		1
60	Mercier	1
60	Rivera	1
60	Hovanec	1
604	Waters	1
61	DeLoach	1
611	Davis	1
611	Sinfield	1
611	Fisher	2
611	Bechetti	1
611	Le	1
611	Norkett	1
611	Semple	1
612	Roe	1
612	Draper	1
651	Henes	1
651	Nelson	1
651	Rodriguez	1
664	Miraglia	1
664	Nahshon	1


NAVSEA
WARFARE CENTERS
Carderock